Biomimetic Bottom-up Assembly of Nanomaterials and Their Applications as Nanoreactors

by

Nuerxiati Nueraji

A dissertation submitted to the Graduate Faculty in Chemistry in partial fulfillment of the requirements for the degree of Doctor of Philosophy The City University of New York.

2008

UMI Number: 3296952

Copyright 2008 by
Nueraji, Nuerxiati

All rights reserved.

UMI Microform 3296952
Copyright 2008 by ProQuest Information and Learning Company.
All rights reserved. This microform edition is protected against
unauthorized copying under Title 17, United States Code.

ProQuest Information and Learning Company
300 North Zeeb Road
P.O. Box 1346
Ann Arbor, MI 48106-1346

©2008

Nuerxiati Nueraji

All Rights Reserved

This manuscript have been read and accepted for the Graduate Faculty in Chemistry in satisfaction of the dissertation requirement for the degree of Doctor of Philosophy.

Hiroshi Matsui

_____	_____
Date	Chair of Examining Committee

Gerald Koeppl

_____	_____
Date	Executive Officer

Michael Drain

Lynn Francesconi

Michael Mirkin

Stephen O'Brien

Supervisory Committee

THE CITY UNIVERSITY OF NEW YORK

Abstract

Biomimetic Bottom-up Assembly of Nano-materials and Their Applications as Nano-reactors

by

Nuerxiati Nueraji

Mentor: Professor Hiroshi Matsui

The design and fabrication of nanometer-sized functional materials have become a widely studied field in nanotechnology due to their potential use as building blocks in nanodevices. Various bottom-up methods have been developed to fabricate nano- and micro-scale devices in microelectronics, optic, actuators and sensors. Introduction of biological self-assembly of nanometer-sized building blocks is expected to accomplish the bottom-up fabrications in a more reproducible, efficient, and economic manner. The development of the next generation of electronic industry demands more advanced electronic circuits. The advanced electronic circuits can be achieved by increasing the packing density of nanometer-sized electronic elements. The application of bottom-up approaches has important potentials for the fabrication of advanced electronic circuits.

In this dissertation, we mainly focused on the two main parts: (A) Synthesis of nano-sized building blocks. Furthermore, the synthesis of unique crystalline structures and shapes of the inorganic and organic nano-materials at room

temperatures and study of their properties. For example, the results of Electric field Microscopy (EFM) showed the ferrolectric properties of Barium titanate nanocrystals formed at room temperature. Also, the semiconducting properties of needle shaped single crystalline structures of organic semiconductors, Polythiophenes, Polyaniline, and Polypyrolle was proved by scanning tunneling spectroscopy (STS). (B) Bottom up approach for fabrication of nanodevice; we propose here a bionanotechnological approach for efficient fabrications of nanometer-scale electronic circuit geometries by anchoring functionalized bionanotubes on to a surface via a complementary bioconjugation mechanism. Nanoparticles with various functions can be coated onto the bionanotubes by "mineralizing peptides" and the electronic properties of the circuit can be tuned by controlling size and packing density of particles on the sidewall of the nanotubes.

For the bottom-up approach, it is mandatory that the synthesis of photonic nanomaterials and their alignments be accomplished efficiently and precisely, due to the effects of the size, alignment, shape, and crystalline structure of the photonic nanocrystals. The tunabilities of these features and the potential of new materials fabrications by using peptides will provide a significant advantage for photonic material syntheses. We have employed peptide-precursor nanoring assemblies for the production of functional nanostructures including gold, ferroelectric barium titanate, and used interfacial polymerization method to produce shape controlled inorganic and organic nanoparticles. In this research, we further fabricated nano-arrays on substrates by the bottom-up approach (AFM-based nanolithography). The tunable spacing between the nanocrystals was adjusted by controlling the dimension of the peptide

nano-rings and functioned as photonic spacers. The novel fabrication methodology provided improved a feasible approach to control the photonic properties of resulting nano-particle arrays.

Furthermore, in order for the *in situ* synthesis of tunable nano-particle arrays on the functionalized substrates as nanodevices, the bio-mineralization process was also applied in the SPM based nanolithography bottom–up approach. The mineralizing peptides were firstly patterned on to surface combining with bioresistive spacers. Corresponding peptides were used to implement the requirement of materials in device. Parameters including pH of solution, spacer, the width of the patterned areas and the nature of peptides were monitored to control the size, inter-particle distance, and shape of nano-particle arrays.

This is

dedicated to

My wife: Winnie

My children: Marat Nuraje

Aygul Nuraje

Acknowledgements

First and foremost, I'd like to give my wholehearted gratitude to my dear mentor, Prof. Hiroshi Matsui, for his inspiring guidance, unconditional devotion, and enlightening instructions in the joyful but challenging journey of my PhD study.

I also own thanks to my research committee members, Prof. Michael Drain, Prof. Michael Mirkin, Prof. Lynn Francisconi and Prof. Stephen O'Brien. This dissertation cannot be so fruitful without their continuous guidance and advice.

As a research collaborator, I own special thanks to Prof. Nan-loh Yang and Dr. Kai Su. Our collaborating has been enjoyable and fruitful.

I own thanks to my previous colleagues in our lab: Dr. Ipsita Banerjee, Dr.Ramin Djalali, Dr.Xueyun Gao, Dr. Anne Runge, Dr.Linglu Yang, Dr. Lingtao Yu, Dr. Robert Maccuspie, and current colleagues: Dr.Anita Swami, Dr.de la Rica, Hanying Bai, Ms. Fen Xu, Mr. Cristophe Pejoux, Mr. Wei Su, Ms Anjia Luona, Ms. Prerna Kaur, Mr.Jacaopo Sampson, Mr. Amit Haboosheh, Mr.Andy Chen, and Ms. Samia Mohammed. Especially Dr.Anita Swami helps me preread the thesis and give me helpful suggestions for the completion of the whole thesis. Most of all, I own thanks to my dear parents; my father:Mr. Nuraje Adumbek and my mother:Mrs. Mareya Baytur; my older brother, Nurem Nuraje; my sister; Nureya Nuraje; my younger brother, Erxat Nuraje.

I especially extend my gratitude to my mother in law, Ms Peifen Fu. She always brings me more interesting information about current hot research topics, and the trends of society and simultaneously encourages me to accomplish significant outcome. During my Ph.D study, she has taken all of responsibility for taking care of

my two children and released me to do more research. I believe that I couldnot get such publications without her encouragement and help.

Finally, I want to express my gratitude to my wife, Winnie for her sustained passionate support to my PhD study and took the most responsibility of taking care of my children.

I also gratefully acknowledge the financial supports from DOE and National Institute of Health..

Thanks,

Nurxat Nuraje (a.k.a Nuerxiati Nueraji)

Table of Contents

List of Figures

List of Tables

List of Schemes

Chapter 1

Fabrication of Ferroelectric Barium Titanate Nanocrystals at Room Temperature Using Peptide Nano-rings as Templates [1]

1.1 Introduction

Ternary oxides, especially $BaTiO_3$ and $SrTiO_3$, have attracted long-standing interest in nanostructure syntheses because of their extraordinary ferroelectric, dielectric, pyroelectric, piezoelectric, and electro-optic properties. As such, they can be widely used in dynamic random access memories, capacitors, electromechanics, and nonlinear optics[2-7]. Miniaturization of ferroelectric $BaTiO_3$ crystals to the nanometer scale is desirable for their application in the next generation of electronics[8-11]; however, the main challenge lies in the growth of barium titanate nanocrystals at room temperature in a tetragonal crystalline structure, which induces the ferroelectric property. In the past, $BaTiO_3$ nanoparticles have been grown in the cubic structure, the most stable form at room temperature, and annealing of the nascent $BaTiO_3$ nanoparticles at high temperature has been necessary to transform their structure from the cubic to the tetragonal form[4, 6, 12-15]. Here, a novel method that uses ring-shaped peptide assemblies as templates for the one-step biomimetic synthesis of ferroelectric $BaTiO_3$ nanoparticles in a tetragonal structure at room temperature is reported. Biological and biomimetic systems produce remarkable structures of crystals controlled by the chemical structure, the morphology, and the shape of the biological templates[16-27]. For example, sea urchin larvae grow single-crystalline calcite in a curved compartment[24], and our approach mimics those systems by growing the unusual structures of the $BaTiO_3$ crystals on curved and confined peptide assemblies. To the best of the authors' knowledge, this is the first report on the growth of ferroelectric $BaTiO_3$ nanoparticles at room temperature.

1.2. Experimental

1.2.1 Synthesis of Bolaamphiphilic Peptides

The scheme of the synthesis of bolaamphiphilic peptides followed previous peptide synthetic approaches[28, 29]. Bolaamphiphiles refer to a series of amphiphilic species with an alkyl chain at the middle of the compound and two hydrophilic end groups (**Scheme 1.1**).

Scheme 1.1 Chemical structure of the bolaamphiphilic peptide.

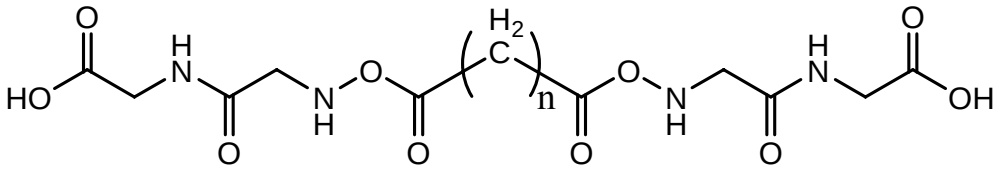

Glycylglycine bolaamphiphiles

By using Bis(*N*-alpha-amido-glycylglycine)heptane-1,7-dicarboxylate as a example, the synthetic route is shown in **Scheme 1.2**. Typically, in N, N-dimethylformamide (DMF) were dissolved the dicarboxylic acid and 1-hydroxybenzotriazole (HOBt). To this solution, a chloroform solution containing N-Ethyl-N′-(3-dimethylaminopropyl)carbodiimide hydrochloride (EDAC) was added at -5^{o}C with stirring and the mixture was stirred for 1 hour at that temperature. To the resulting solution, a methanol solution containing glycylglycine benzyl ester hydrochloride, and then triethylamine were successively added. The mixture was stirred for 24 hours while gradually increasing the temperature to room temperature. The solvent was then removed in vacuo to obtain a white precipitate. The precipitate was washed on a filter paper successively with a 10%wt aqueous citric acid solution, water, a 4%wt aqueous sodium hydrogen carbonate solution and water and then

crystallized from DMF to obtain N, N'-bis(glycylglycine benzyl ester)heptane-1,7-dicarboxyamide. This dicarboxyamide was dissolved in DMF in a water bath at 50°C, to which a 0.1N NaOH solution was added. The precipitate was recrystallized from DMF to obtain Bis(*N*-alpha-amido-glycylglycine)heptane-1,7-dicarboxylate (C7) as a white solid.

Scheme 1.2 Synthesis of Bis(*N*-alpha-amido-glycylglycine)heptane-1,7-dicarboxylate.

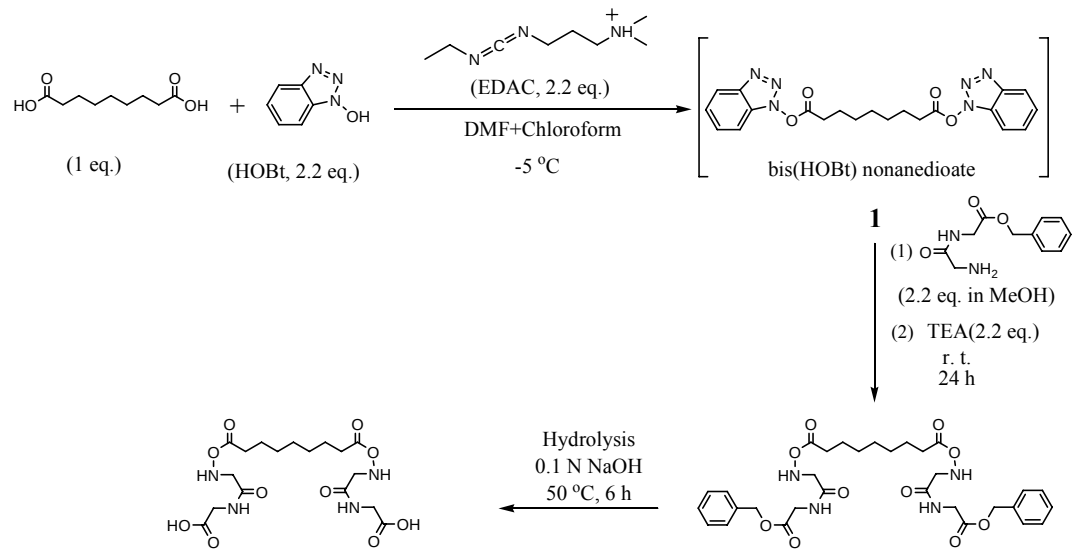

1.2.2 Nano-ring Self-assembly by C7 and A Bimetallic Precursor

Bis(*N*-alpha-amido-glycylglycine)heptane-1,7-dicarboxylate, C7, and bimetallic precursor, barium titanium ethyl hexano-isopropoxide, $BaTi(O_2CC_7H_{15})[OCH(CH_3)_2]_5$, were used as monomers to self-assemble nano-rings. In the peptide monomer solutions (10mL) at different pH values by using citric acid/NaOH (10mM) as the buffer solutions were added 20μL of

$BaTi(O_2CC_7H_{15})[OCH(CH_3)_2]_5$ (13%wt in isopropyl alcohol, Alfa Aesar). Ring-shaped self-assemblies appeared after 1–4 days in the dark. This solution containing the nano-ring-$BaTiO_3$ complexes was washed with deionized water and centrifuged at 14.5k rpm. After this process was repeated twice, the solution was then irradiated by long-wave UV light (355 nm) for 10 hours to remove the peptide templates. The final product was then washed and centrifuged to purify the tetragonal $BaTiO_3$ nanocrystals.

1.2.3 Morphological and Structural Studies of The Nano-ring Self-assembly and The Final Barium Titanate Nanocrystals

The nano-rings and the extracted $BaTiO_3$ nanoparticles were imaged by AFM (Nanoscope III, Vecco, Inc.) on freshly cleaved mica surfaces. These samples were also dried on carbon-coated copper grids at room temperature and studied by TEM and electron diffraction (JOEL 1200 EX) at an acceleration voltage of 100 kV. X-ray diffraction was measured using a Philips PW3040. A confocal Raman microscope (LabRam, Jobin Yvon/Horiba) was used to obtain Raman spectra and two-dimensional Raman images. The 632.8nm line of an air-cooled He/Ne laser was injected into an integrated Olympus BX 40 microscope and focused to a spot size of approximately 0.7μm by an 80× long-working-distance objective.

1.2.4 Ferroelectric Polarization Study by Electrostatic Force Microscope (EFM)

EFM images of the $BaTiO_3$ nanoparticles were recorded by the same atomic force microscope with a NanoScope Extender (Vecco, Inc) on Au substrates.

1.3 Results and Discussion

Peptide templates are used to hydrolyze $BaTi(O_2CC_7H_{15})[OCH(CH_3)_2]_5$ inside the cavities in order to produce the tetragonal $BaTiO_3$ nanoparticles at room temperature. Previously, it has been found that ring-shaped peptide assemblies could template Au-nanoparticle formation inside the peptide rings[30]. While the size of the Au nanoparticles can be controlled by the cavity size, they grow with or without the peptide nanorings. However, the new discovery reported here is that the peptide nanorings have the biomimetic function of crystallizing nanometer-scale crystals that have never been grown under ambient conditions. In other words, tetragonal $BaTiO_3$ nanoparticles can only grow in the peptide nanorings at room temperature. When the peptide monomer solutions are added to a precursor, $BaTi(O_2CC_7H_{15})[OCH(CH_3)_2]_5$,[2] ring-shaped self-assemblies appear after 1–4 days in the dark. During this process, the peptide nanoring templates are selfassembled simultaneously as the precursors are hydrolyzed in the cavities (Figure 1.1). The peptide nanoring structure has previously been investigated[30]. Figure 1.2(a) shows the phase image of $BaTiO_3$ nanoparticles inside the peptide nanorings in a pH4.5 solution determined by atomic force microscopy (AFM). In this AFM phase image, the harder barium titanate nanoparticles appear in a brighter contrast at the centers of the peptide nanorings, which appear as softer assemblies in a darker contrast. The peptide nanorings are monodisperse with a size of 49 ± 11 nm, as determined by AFM and transmission electron microscopy (TEM). This phase contrast is consistent with that of Au nanocrystals grown inside the peptide nanorings imaged previously[30]. The magnified TEM image of the barium titanate nanoparticle in the peptide nanoring, Figure 1.2(b), also clearly shows a darker $BaTiO_3$ particle grown inside the peptide template. The Raman spectra of the ring/ $BaTiO_3$ complexes shown in Figure 1.5 reveal the presence of Ti–carboxylate ligation. For example, peaks at 1582, 1362, and 1060 cm–1, marked in Figure 1.5, correspond to the *m*(C–O) carbonate bands in the oxalate-bridged metal complex, COO– Ti–OOC[31]. The peak at 767 cm–1 represents the Ti–O–Ti stretching mode. This chelate structure is consistent with the one between the barium titanate precursors and the hydroxylated block-copolymer surfaces[32]. When the peptide nanorings with the $BaTiO_3$ nanoparticles are irradiated by UV light (355

nm) for 10 h in solution, the peptide template shells are removed, as shown in Figure 1.3. Previously, Au nanoparticles have also been grown in peptide nanorings self-assembled from peptide monomers and Au ions, and long UV irradiation destroyed the ring templates due to reduction of the Au ions that chelated the carboxylates of the peptide monomers to form the nanoring structure.[30] It is likely that a similar reduction mechanism destroys the nanoring templates of the BaTiO3 nanoparticles because the UV irradiation renders the Ti ions ineffective so they can no longer function as a glue to sustain the ring structure via the Ti-ion/peptide chelation. The AFM image in Figure 1.3 shows monodisperse $BaTiO_3$ nanoparticles with a diameter of 12 ± 1 nm after UV irradiation of the ring/particle complexes for 10 h. The contrast of the nanoparticles in the AFM phase image in Figure 1.3 is consistent with that in the centers of the nanorings in Figure 1.2(a), which suggests that the nanoparticles are released from the nanorings. The electron diffraction pattern of the resulting BaTiO3 nanoparticles in the inset of Figure 1.3 indicates that they are highly crystalline. The outer and inner diameters of the peptide nanorings are observed to change as a function of pH of the growth solution, as shown in Figure 1.4. This plot shows that the size of the nanoring decreases from 49 to 23 nm as the pH is increased from 4.5 to 10. Figure 1.4 also shows that the decrease of the peptide nanoring cavity size directly influences the size of the $BaTiO_3$ nanoparticles grown inside the cavities. Under all growth conditions, their sizes are observed to be very monodisperse, and their sizes can be changed from 12 to 6 nm, as shown in Figure 1.4. The structure of the $BaTiO_3$ nanoparticles has been studied by X-ray diffraction as shown in Figure 1.6. In this figure the (100), (110), (111), (200), (210), and (211) faces of $BaTiO_3$ are observed. The magnified X-ray diffraction spectrum in the inset inset of Figure 1.6 resolves the characteristic (002) and (200) faces of the tetragonal $BaTiO_3$ crystals[33]. To test the nanometerscale ferroelectric property of the tetragonal $BaTiO_3$ nanoparticles, electrostatic force microscopy (EFM) was used to image and manipulate the ferroelectric polarization of these nanoparticles. This procedure is summarized in Figure 1.7a. In the first step, the electric polarization of the $BaTiO_3$ nanoparticles is manipulated by applying a voltage, V_{write}, to the conductive AFM tip that gently contacts the nanoparticles[4].

After the local electric polarization is written onto the nanoparticles, the resulting polarization is probed using EFM with a lower voltage, V_{probe}, by measuring the shift in the resonance frequency of the AFM tip[9]. As shown in Figure 1.7a, during the probing process the AFM tip is raised at a constant height above the nanoparticles in order to avoid interference between the manipulated polarization and V_{probe}[34]. The raised distance of 40 nm enables one to image only the contribution from the surface charges associated with the local electric polarization of the $BaTiO_3$ nanoparticles. After a V_{write} of +12 V was applied to $BaTiO_3$ nanoparticles with an average diameter of 12 nm (Figure1.7b), the EFM image of those nanoparticles to which a V_{probe} of +2 V was applied, shown in Figure 1.7c, appears in a brighter contrast compared with the background due to the repulsive electrostatic interaction between the tip and the nanoparticles[9]. After a V_{write} of –12 V was applied to the same $BaTiO_3$ nanoparticles, the EFM image of those nanoparticles to which a V_{probe} of 2 V was applied, shown in Figure 1.7d, appears in a darker contrast compared with the background due to the attractive electrostatic interaction. It should be noted that control experiments that involved scanning the manipulated nanoparticles with V_{probe} = –2 V resulted in reverse EFM images, which confirms that the probe voltage did not interfere significantly with the written polarization. These EFM images indicate that the $BaTiO_3$ nanoparticles synthesized in the peptide nanorings at room temperature possess a ferroelectric property by reorienting the spontaneous electric polarization with an external electric field. Previously, when mineralization of calcite has occurred in micrometer-scale pores of membranes, the resulting crystals in the pores have been observed to have unusual crystalline forms and structures due to unusual surface tensions and reaction kinetics of the crystal growth in such small confined regions[24]. The shapes of crystallizing templates in organisms are also observed to have a significant impact on the resulting crystalline structures grown on biological templates[26, 35]. The nanometer-scale peptide rings used here as the confining templates for the crystal growth of $BaTiO_3$ took this strategy of the confinement-controlled mineralization one step further to the nanometer scale. As observed by the crystal growth in the membranes, the confinement effect of the peptide nanorings induced the unusual crystallization of tetragonal nanoparticles of $BaTiO_3$. Since the

arrangement and the distribution of selfassembled monolayers (SAMs) of nucleating functional groups have previously been observed to influence the resultingcrystalline structures[35], the chemical structure, such as the location of carboxylic acid groups that chelate Ti ions on the curved surfaces of the peptide nanorings, should also be a critical factor in growing tetragonal $BaTiO_3$ nanoparticles
without annealing. The exact chemical structure of the peptide assemblies is still under investigation.

Figure 1.1 Schematic fabrication of $BaTiO_3$ nanoparticle by (i)bolaamphiphilic peptide C7 and (ii) bimetallic precursor.(a) self-assembly with precursor. (b) UV irradiation

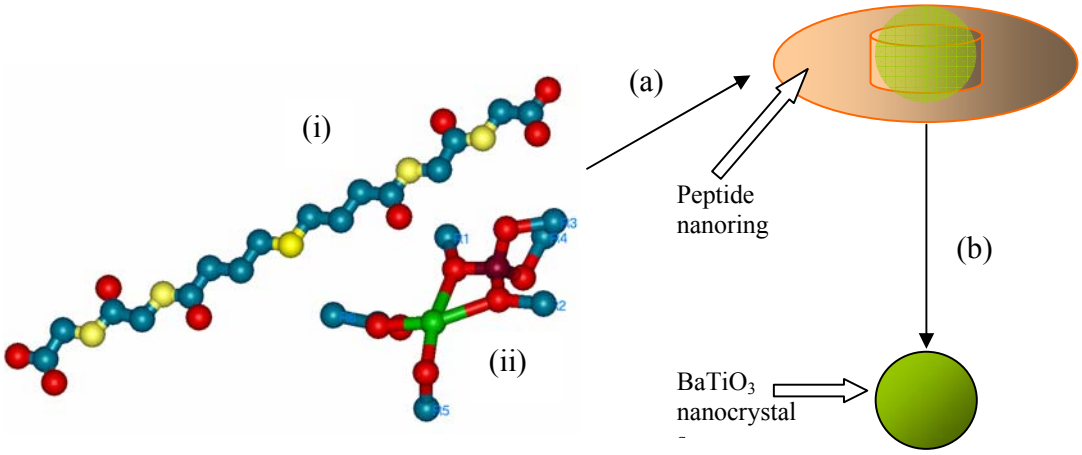

Figure 1.2 (a) Atomic force microscopy (AFM) phase image of barium titanate nanoparticles inside peptide nano-ring templates. Scale bar = 50 nm. (b) TEM image of a barium titanate nanoparticle inside the peptide nano-ring template. Scale bar 70 nm. (by Nurxat)

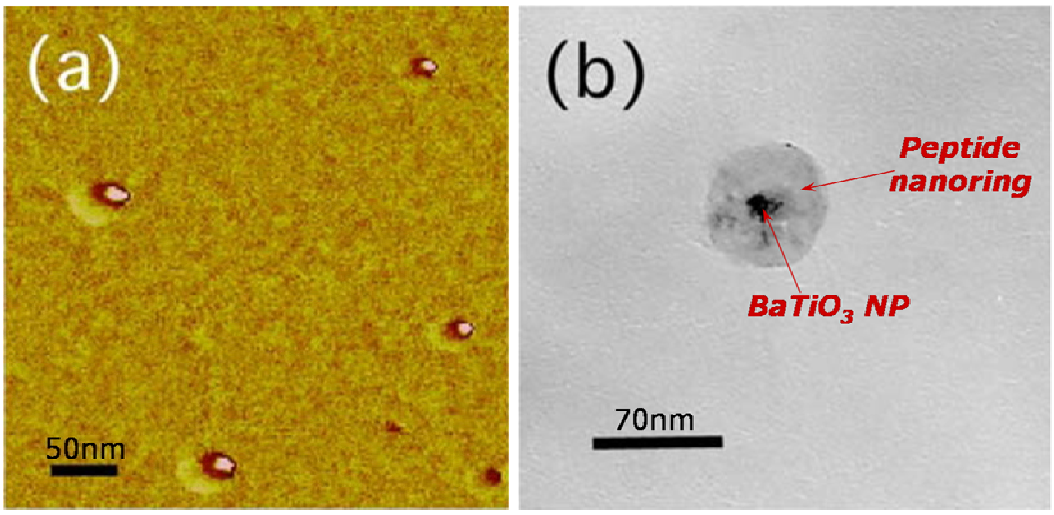

Figure 1.3 AFM phase image of barium titanate nanoparticles after removal of peptide nanoring templates. Scale bar = 60 nm. Inset shows an electron diffraction pattern of the barium titanate nanoparticles with the (110), (111), (210), and (211) faces. (by Nurxat, Jacopo, Amit & Kai)

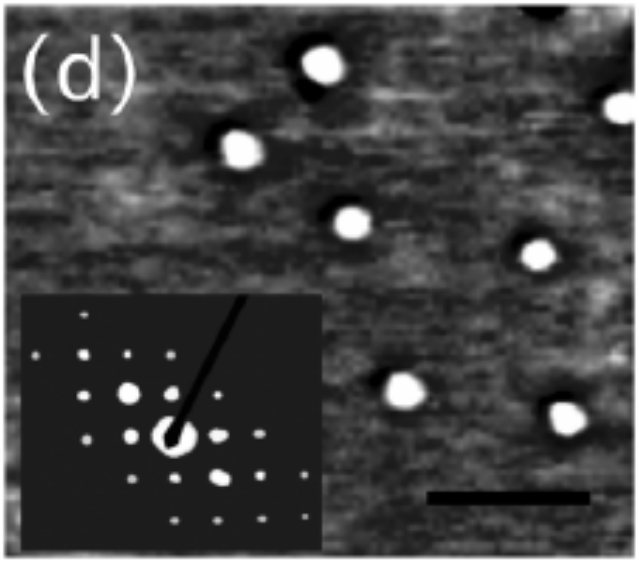

Figure 1.4 Sizes and distributions for the nano-rings assemblies and the final barium titanate nanoparticles at different pH values

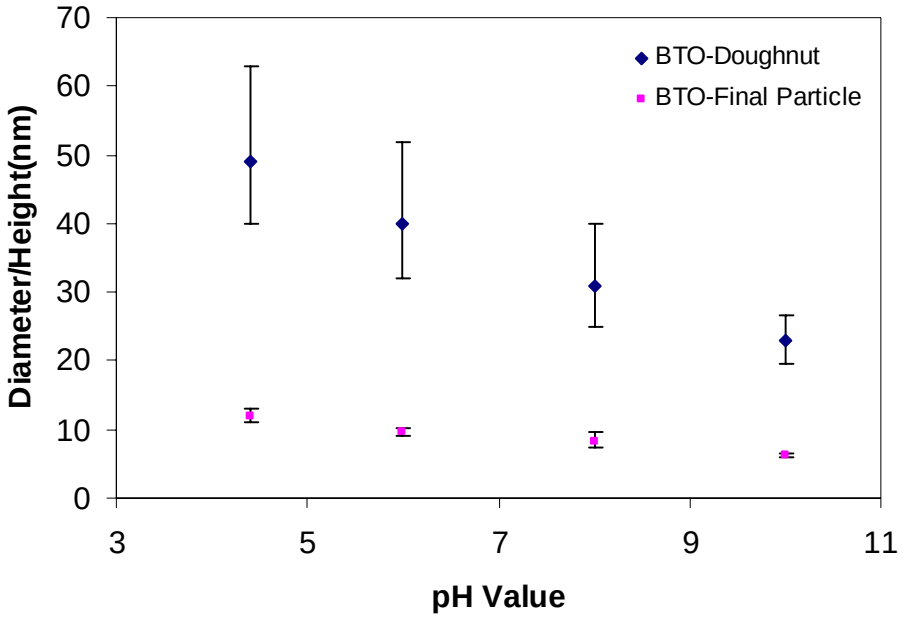

.

Figure 1.5 Raman spectra of (a) nanotubes self-assembled from the peptide monomers without the barium titanate salts (b) nano-doughnuts self-assembled from the peptide monomers in the presence of the barium titanate salts. (by Nurxat & Kai)

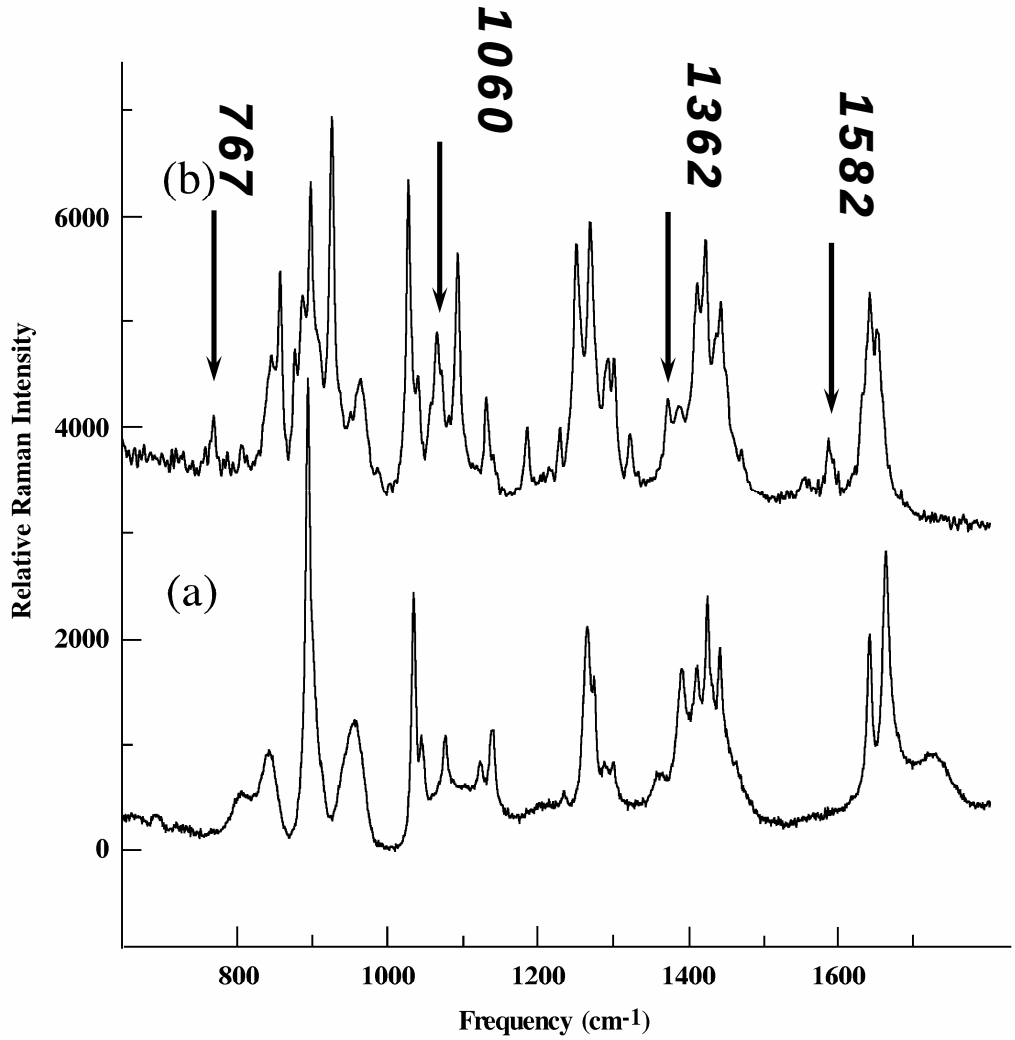

Figure 1.6 (a) X-ray diffraction pattern of barium titanate nanocrystals, from the solution at pH=10, with the enlarged 2-theta area for the assignment of tetragonality. (by Kai)

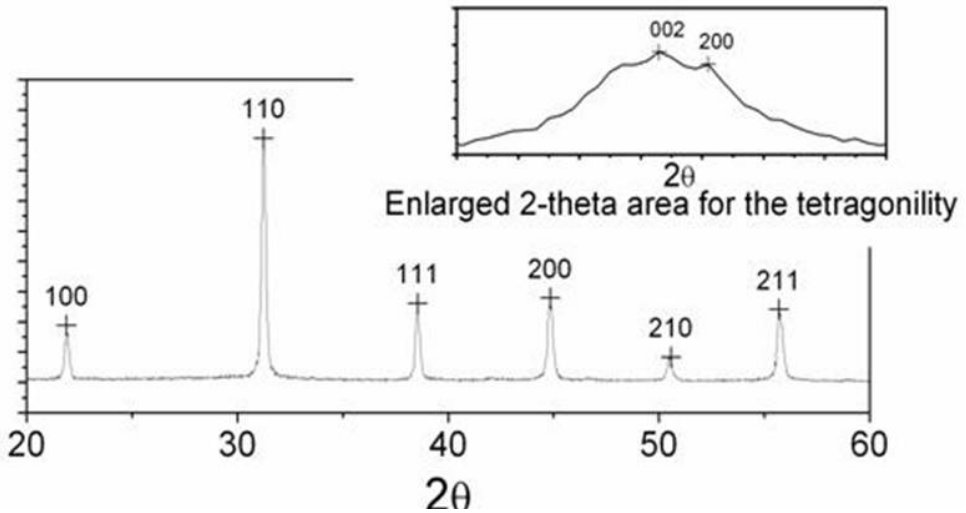

Figure 1.7 (a) The schematic representation of manipulating and probing electric polarization of $BaTiO_3$ nanoparticles with EFM; (b) Topological AFM image of barium titanate nanoparticles. Scale bar = 30 nm; (c) EFM images of barium titanate nanoparticles with V_{probe} = +2 V after V_{write} = +12 V was applied on the nanoparticles across a conductive AFM tip and a gold substrate. Scale = 30 nm; (d) EFM images of barium titanate nanoparticles V_{probe} = +2 V after V_{write} = -12 V, was applied on the nanoparticles across a conductive AFM tip and a gold substrate. Scale = 30 nm. (by Nurxat, Kai & Edward)

.

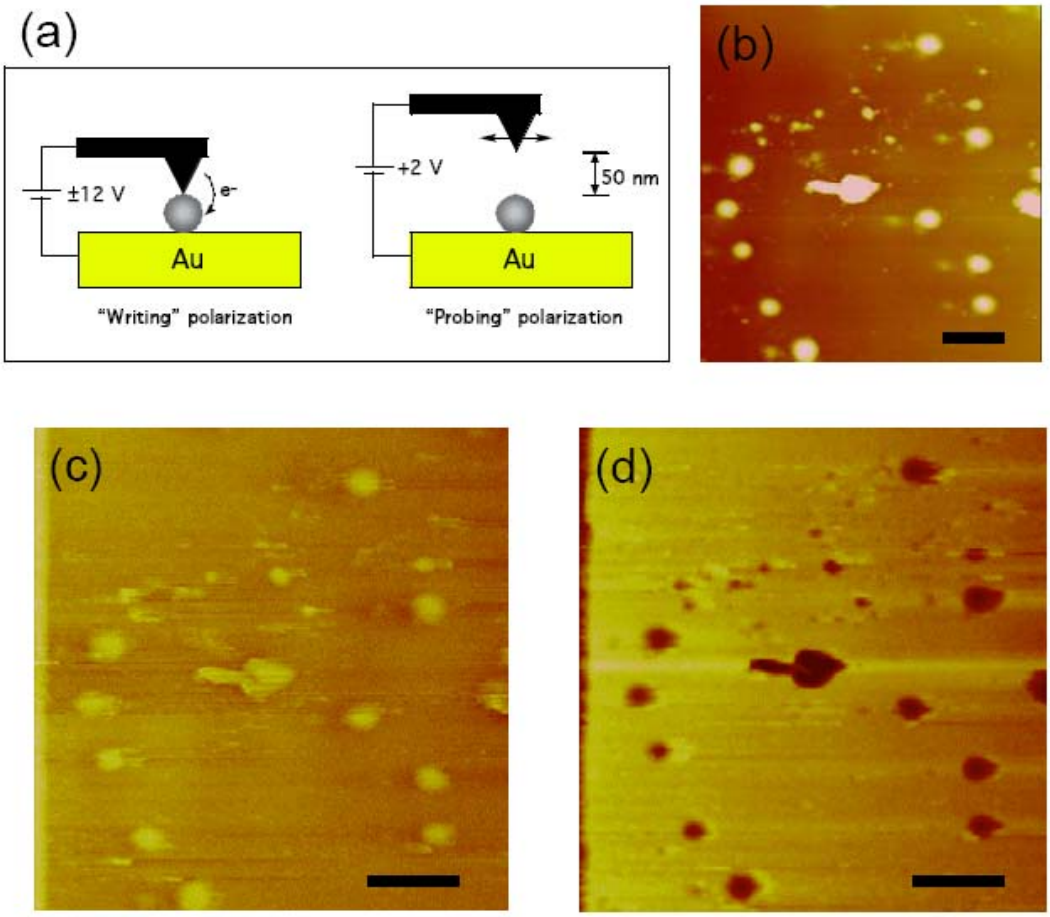

1.4 Conclusion

In conclusion, ferroelectric $BaTiO_3$ nanoparticles were hydrolyzed inside the peptide-ring templates at room temperature and under ambient pressure, and these nanoparticles had the tetragonal crystalline structure. Because the cavity sizes of nano-rings were changed as a function of pH, the diameters of monodisperse $BaTiO_3$ nanoparticles could be controlled between 6 nm and 12 nm. The resulting $BaTiO_3$ nanoparticles were also demonstrated to possess the switching behavior via external electric fields by reorienting their spontaneous electric polarization as the direction of the electric fields was switched. This unusual crystallization of tetragonal $BaTiO_3$ nanoparticles at room temperature was likely induced by the surface chemical structure of peptide templates and the high surface tension in the nano-scale peptide cavities. Generally various important electric materials are synthesized at high temperature, however if these syntheses can be conducted in milder experimental conditions such as room temperature, it can reduce the production cost, the facility size (such as cooling systems), and the manpower, which will have a huge impact for manufacturing. The high temperature processing could also lead to nanoparticle aggregations and defects due to local thermal stresses. If the ring-shaped peptides enable one to synthesize those crystals at low temperature, as seen in the case of the tetragonal $BaTiO_3$ nanoparticles, this approach will provide a new route for novel material syntheses.

Chapter 2

An Open-Bench Method for the Preparation of $BaTiO_3$, $SrTiO_3$ and $Ba_xSr_{1-x}TiO_3$ nanocrystals at 80°C[36]

2.1 Introduction

The remarkable physicochemical properties of $BaTiO_3$ (BTO), $SrTiO_3$ (STO), and $Ba_xSr_{1-x}TiO_3$ (BST) have attracted sustained scientific and technological interest.[37-39] With the current advances in nanoscience, such high-quality perovskite mixed-metal oxide crystals on the nanometer scale without a history of thermal stress are highly desirable as fundamental elements for nanosystems, including nanocapacitors and ferroelectrics such as ferroelectric random access memories (FeRAM).[5, 40] We report here the first synthesis of $Ba_{0.7}Sr_{0.3}TiO_3$ nanocrystals in the size range from 50 to 10 nm with achievable giant dielectric constants ($1.4 * 10^5$) at room temperature using a facile synthesis route involving an open-bench system at 80 °C. This synthesis is based on results from our preparation of nanocrystals of BTO, STO, and BST with various compositions. BTO and STO are among the most studied perovskite ferroelectrics. In the past, most synthesis procedures for the preparation of perovskite crystals included high-temperature (1000 °C) sintering followed by annealing. Recently, extensive effort has been focused on the establishment of moderate reaction conditions, especially lowering the synthesis temperature for high-quality nanocrystals.[1-3, 13, 40-44] Various methods for the synthesisof perovskite nanocrystals have been developed, including co-precipitation,[45, 46] sintering of organometallic

precursors,[47] hydrothermal and solvothermal methods,[13, 41, 48-51] sol-gel process,[2, 52] and procedures mediated by molten composite-hydoxide.[42] Recent interests in nanoscience led to extensive efforts focusing on obtaining BTO and STO nanocrystals based on the understanding gained from bulk crystals.[5, 10] The synthesis of BST nanocrystals with systematic composition variation has not been reported.

There are special issues in preparing ferroelectric nanocrystals due to their very high surface to volume ratio. The impurity ions on the surface of the nanostructures may form a depolarization field preventing the tetragonal phase to grow.[5, 53, 54] The tetragonal polymorph was usually obtained upon cooling the products to room temperature after a ~1000^{o}C sintering. Although approaches with a trend towards low-temperature synthesis of perovskite nanocrystals have been developed,[13, 41, 42] most of the synthetic temperatures were higher than the Curie temperature (~120^{o}C) of BTO. Our recent room temperature synthesis of ferroelectric nanocrystals with diameters from 6 to 12nm using a bolaamphiphilic peptide ring as the template was discussed.[55] The peptide ring in the equatorial direction prevented the approach of impurity ions to the particle surface from the lateral direction providing an asymmetric environment conducive to the growth of the tetragonal polymorph. A fungus-mediated biological route toward the synthesis of tetragonal barium titanate nanoparticles of sub-10nm dimensions under ambient conditions was also reported.[43] Most recently, a *bio-inspired* process has been applied for the room-temperature synthesis of BTO from a bimetallic alkoxide precursor.[44] Nonaqueous approaches have also been developed to synthesize nanocrystalline BTO, STO, and $Ba_{0.5}Sr_{0.5}TiO_3$ mixed-metal oxide using elemental alkaline earth metals as starting materials.[13] The resulting BTO and BST nanocrystals

were found to be of cubic polymorph.[56] Based on a reaction between a metallic salt and a metallic oxide, nanometer-sized BTO and $Ba_{0.5}Sr_{0.5}TiO_3$ have also been synthesized in a solution of composite-hydroxide eutectic at ~200^{o}C.[42] Our reverse micelle route performed on a bench top at 80^{o}C gives high-quality nanocrystalline BSTs with variable compositions leading directly to nanocrystals with giant dielectric constants. This finding is significant in providing, through a readily accessible synthetic route, novel particles with size down to the 10nm level for nanoelectronics.

BTO/STO artificial superlattices in thin films have been fabricated by pulsed laser deposition (PLD) on many substrates.[57] PLD method can fabricate of BTO/STO superlattice with stacking periodicity varying from 1:1 to 125:125. Using X-ray diffraction (XRD), the BTO/STO superlattics showed both BTO and STO characteristic peaks, while BST solid solutions from solvothermal method, and our present system only showed characteristic peaks for the BST nanocrystals, indicating the atomic mixing nature of the Ba^{2+} and Sr^{2+} sites.

Reverse micelles as efficient nanoreactors have been applied to the syntheses of nanocrystals.[58] In our syntheses, titanium tetrachloride, strontium chloride and barium chloride aqueous solutions were used as starting materials without organic components to obtain high-quality, homogeneous, stoichiometric BST nanocrystals. The system consisted of a combination of four components of the reverse micelles: cyclohexane (oil phase), aqueous solution of the metal chlorides, triton X-100 (emulsifier) and n-butanol (co-emulsifier). The system remained stable and transparent up to the point of extensive condensation of hydroxy precursors. The nonionic surfactant allows the optimization of pH for the formation of mixed-metal oxides without altering the micelle

structure significantly. The optimum OH^-/Ti^{4+} molar ratio was estblished to be 2 (see Section 2.2, Experimentals). The use of only inorganic substances in reverse micelles is of importance for the following reasons: (1) the impurity ions can be readily removed from the final products by washing with water; (2) total inorganic starting materials are ideal for the aqueous phase in the reverse micelle so that all the reactions are confined inside the nanoreactors; (3) the reaction temperature of 80°C, is much lower than that of reported synthetic procedures for BST; (4) the same micelle system can be used to make nanocomposites of BST with polyelectrolytes or conducting polymers by emulsion polymerizations in a one-pot method.[59]

2.2 Experimental

As the chemicals were purchased from Aldrich and used as received. In a typical synthesis, a hydrochloric acid (37%) solution (6.39g, 47%) of $TiCl_4$ (99.9%) and 15mL DI water were mixed and used as the aqueous phase, and cyclohexane (99%, 23g) as the oil continuous phase. Triton X-100 (labotary grade, 25g) and n-butanol (99.4%, 28g) were selected as the emulsifier and co-emulsifier. The chemicals were then transferred to a 500ml flask equipped with a stirrer, a thermometer, a dropping funnel and a reflux condenser. With stirring, a 40%NaOH (97%) solution was dropped into the flask until pH=7. Stoichiometric amount of $SrCl_2 \cdot 6H_2O$, 99%, (or $BaCl_2 \cdot 2H_2O$, 99%) was dissolved in de-ioned water (25ml) and then added into the flask dropwise under continuous stirring. Additional 40%NaOH aqueous solution with was then added dropwise into the colloid system until OH^-/Ti^{4+}=2/1. This reaction system was then kept at 78-80℃ for 3 hours prior to a centrifugation at 4000rpm for 15min. The resulting sediment was redispersed in de-ironed water using

an ultrasonic bath. This centrifugation-redispersion cycle was repeated at least three times to remove emulsifiers and other ionic impurities. The final particles were dried in vaccu at 80℃ over night. The dried BSTO powders were characterized by X-ray diffraction (XRD, Philips PW3040) for crystalline phase determination. Transmission electron microscope (TEM, JOEL 1200 EX) and electron diffraction at an acceleration voltage of 100 kV were used to characterize the morphologies and crystalline structures of BSTO nano-co-crystals. The dielectric constant measurements were conducted on a Novocontrol BDS 80 high-resolution broadband dielectric spectrometer with a sample holder cell (diameter: 19.21mm; thickness: 0.27mm).

2.3 Results and Discussion

The nanocrystals synthesized using our open-bench method are of high quality based on data from XRD, Fourier transform infrared (FTIR) spectroscopy, energy dispersive X-ray spectrometry (EDS) and TEM. **Figure 2.1** shows the XRD pattern of BTO nanocrystals, no characteristic peaks from $BaCO_3$ or TiO_2 impurities were observed.

Figure 2.1 XRD patterns of BTO nanocrystals. (by Kai & Nurxat)

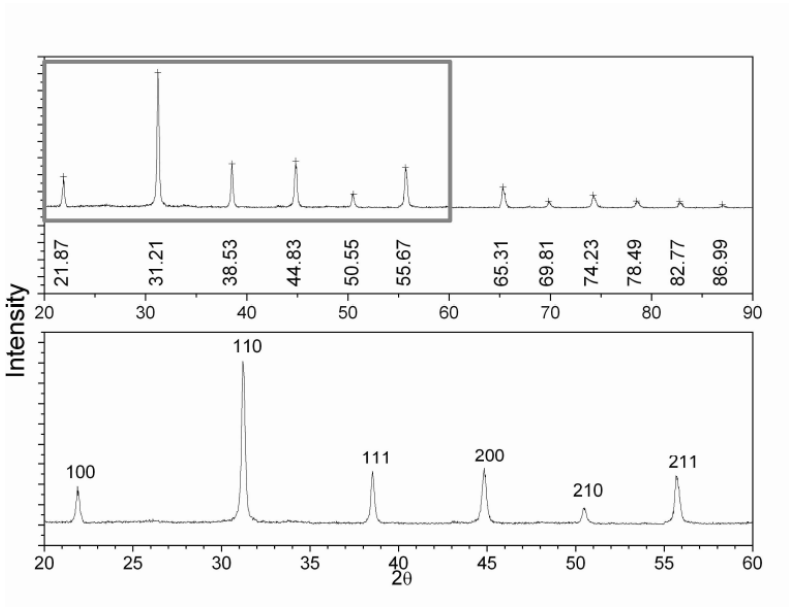

The BTO lattice parameters are in agreement with the reported data (JCPDS No. 31-174). The quality of the products from our synthetic and purification procedure was further established by FTIR and EDS. These analytical data (**Figure 2.2** and **2.3**) from our nanocrystals serve as examples of the high quality achievable by our reverse micelle synthetic procedure. For example, in the spectrum of STO (**Figure 2.2**), there are no observable vibrational peaks from organic impurities. The absorption at 534 cm^{-1} indicates the formation of Ti-O octahedra and the broad peak at 3358 cm^{-1} reflects the absorption from surface hydroxyl groups. In the EDS analysis of BTO (**Figure 2.3**), no detectable Cl or Na peaks were observed, indicating that Cl^- and Na^+ ions were efficiently removed from the final products by thorough washing.

Figure 2.2 FTIR spectrum of STO nanocrystals (by Kai & Nurxat)

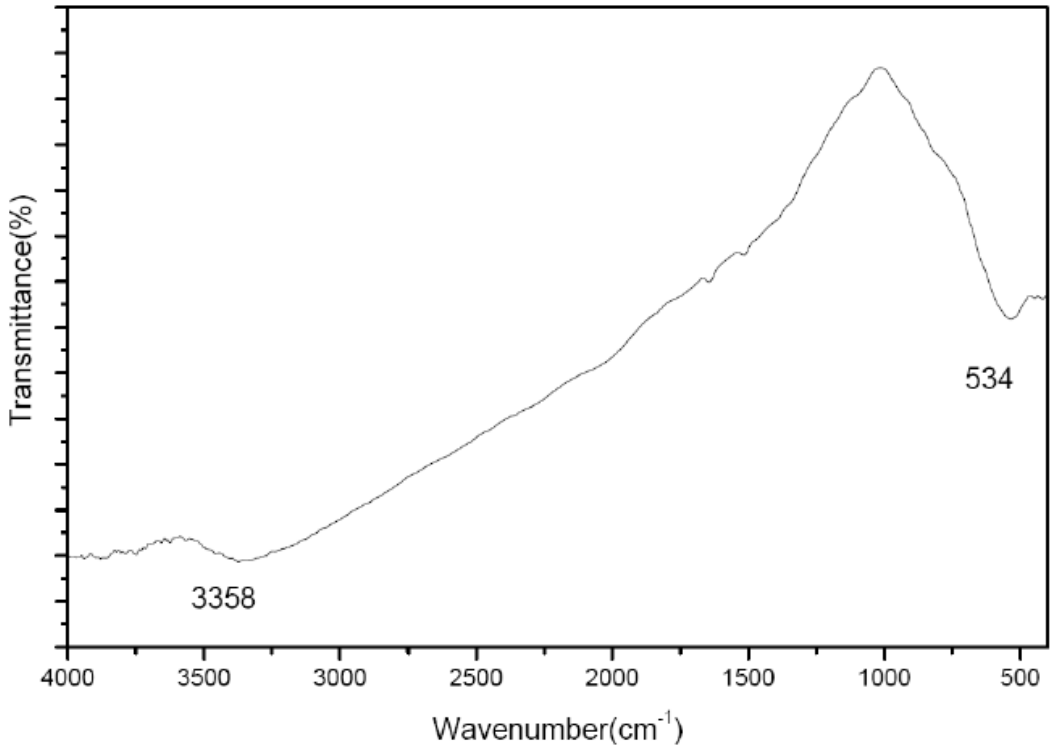

Figure 2.3 EDS spectrum for BTO nanocrystals. Si signal is from the silicon wafer supporting substrate. (by Kai & Nurxat)

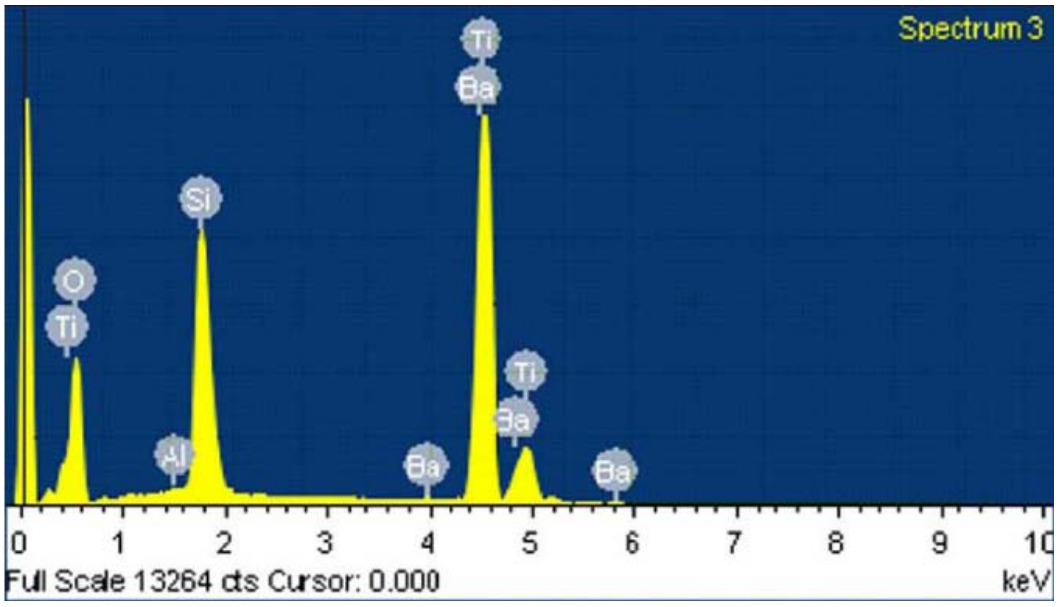

The manipulation of the Ba^{2+}/Sr^{2+} molar ratio in the BST nanocrystals was demonstrated by the synthesis of a series of BST nanoparticles with the molar fractions of Ba^{2+} varied in the steps of 0.1. The XRD of $Ba_xSr_{1-x}TiO_3$, **Figure 2.4 (a)**, with the full range of compositions show a single 200/002 peak for each composition, indicating the formation of true solid solution with atomic mixing of Ba^{2+} and Sr^{2+} rather than superlattice which would show separate BTO and STO peaks.[57] With the change in the composition of BST, the trend of 2θ for the 200/002 peak and the variation in dielectric constant are depicted in **Figure 2.4 (b)**. The 2θ value decreased from 46.74 to 44.83 with increasing Ba^{2+} molar fraction, indicating the lattice unit expanded from 3.904 to 4.039Å. The decrease of 2θ values for the series of BST nanocrystals shows three distinct regions in **Figure 2.4 (b)**. The highest rate of lattice expansion with increase in Ba^{2+} takes place in the range of x=0.3 to 0.7. This is the first systematic investigation of BST with methodical composition variation.

As expected, the change of the features of XRD is most pronounced in the range of near equal Ba^{2+} and Sr^{2+} compositions (x=0.4 to 0.6). In this region, the 111 peaks show much greater variation than the 200 peaks; the former plane is defined by periodicity involving less atomic positions than the latter, thus more sensitve to changes in Ba^{2+}/Sr^{2+} composition ratios. At x=0.5, the XRD data showed a decrease in crystallinity with further deterioration at x=0.6. There is a conspicuous return to the previous level for high-quality crystals at x=0.7. From x=0.7 to pure BTO, a gradual change toward BTO peak positions for both 111 and 200 peaks was observed. As shown in Figure 2.4(b), the room temperature static dielectric constant has a marked jump at x=0.7 to a high level of $1.4x10^5$. This maximum was observed previously for

bulk crystals,[60-62] and in agreement with molecular dynamic calculation.[63] The giant dielectric constant observed indicates the tetragonal polymorph of the nanocrystal. In the low size range of 50 to 10nm, XRD data can not be used to rule out the presence of cubic polymorph.[64]

Figure 2.4 XRD and dielectric results for BTO, STO and BST nanocrystals. (a) The XRD patterns for BST nanocrystals. (b) The shifting of 2θ value at 200/002 peaks and the static dielectric constants for BST with increasing of Ba^{2+} molar fraction. ■-2θ values in XRD; Δ-static dielectric constant values. (by Kai &Nurxat)

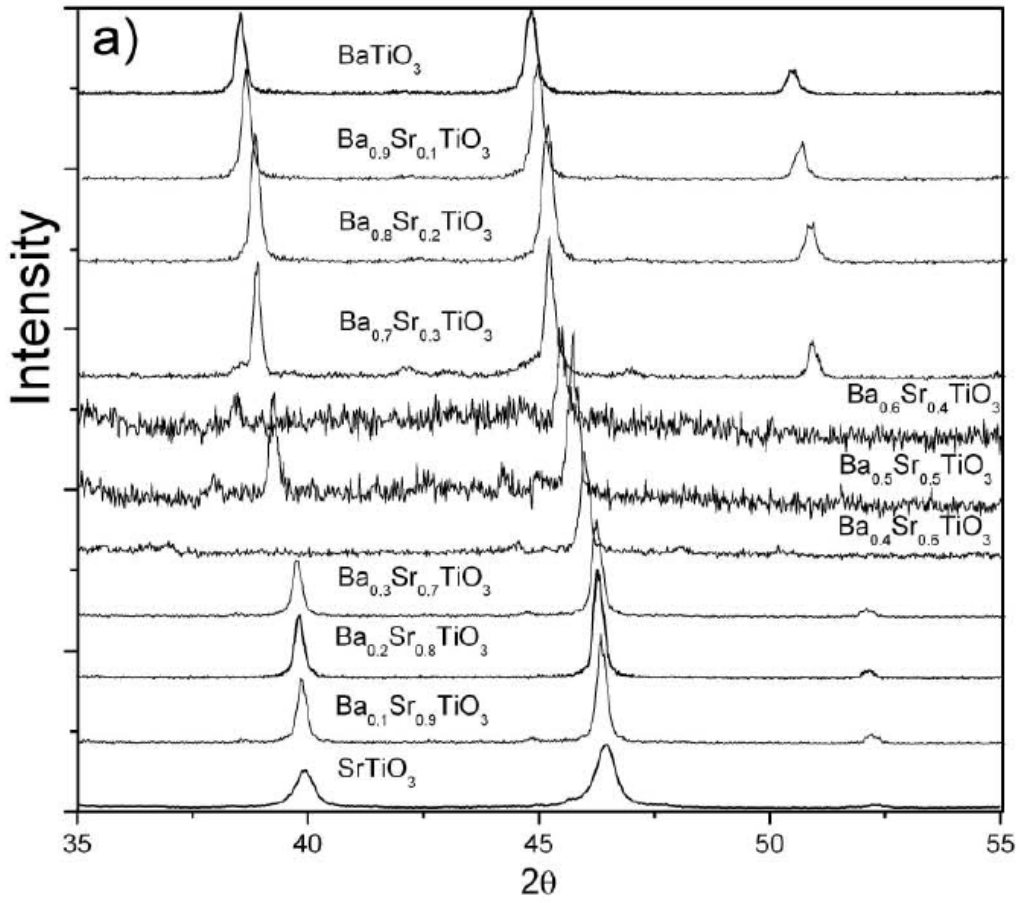

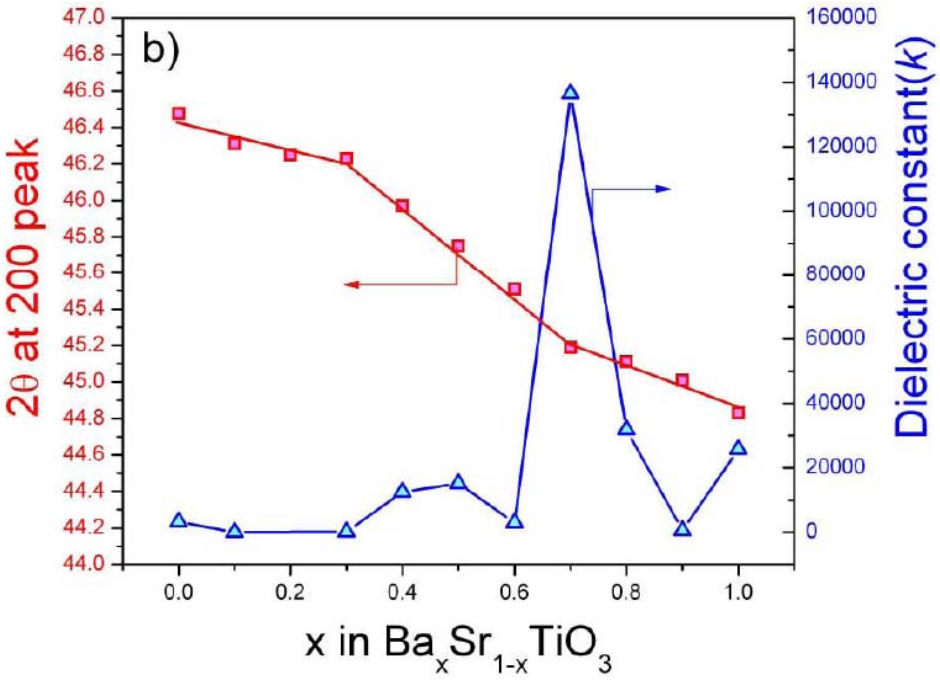

The TEM images and electron diffraction patterns of BTO, STO, and $Ba_{0.7}Sr_{0.3}TiO_3$ nanocrystals are shown in **Figure 2.5**. The BTO nanocrystals have an average size of 80nm in **Figure 2.5 (a)** and **(e)**. Thus, bypassing the final high temperature sintering process avoided the formation of agglomerates. The electron diffraction pattern, **Figure 2.5 (d)** also indicates that the synthesis gave directly high-quality nanocrystals. Both the shape in TEM and the spot matrix in the electron diffraction pattern support the preparation of single-crystalline BTO nanoparticles at a temperature as low as 80^{o}C. **Figure 2.5 (b)** and **(g)** show the TEM of STO nanocrystals as non-agglomerated nanocubes with an average size of 70nm. The electron diffraction pattern with lattice indices in **Figure 2.5 (f)** shows the single crystalline nature of STO nanocrystals. Unlike STO and BTO, the $Ba_{0.7}Sr_{0.3}TiO_3$ nanocrystals show rather uniform nanospheres in the TEM image, **Figure 2.5 (c)** and **(i)**, with an average diameter of

50nm. The electron diffraction patterns, **Figure 2.5 (d)**, **(f)**, and **(h)**, are in agreement with XRD results.

The preparation of $Ba_{0.7}Sr_{0.3}TiO_3$ nanocrystals with giant dielectic constant was extended to still lower size ranges, 20 to 10 nm, based on fine tuning the size of the aqueous micelles through changing the surfactant to water ratio. Particles in this low size range can have potential application to FeRAM. Keeping the oil phase, emulsifier and co-emulsifier amounts constant, and changing the amount of the aqueous contents by ½ and ¼ led to uniform BST nanoparticles of smaller sizes: 15-20nm in diameter from the system the ½, **Figure 2.6 (a)** and **(b**), and 5-10nm in diameter from the ¼, **Figure 2.6 (c)** and **(d**).

Figure 2.5 TEM images and electron diffraction of BTO, STO and $Ba_{0.7}Sr_{0.3}TiO_3$: (a-c) TEM images of BTO, STO, and $Ba_{0.7}Sr_{0.3}TiO_3$, respectively. (d, f and h) the electron diffraction patterns of BTO, STO, and $Ba_{0.7}Sr_{0.3}TiO_3$, respectively. (e, g and i) TEM images of BTO, STO and $Ba_{0.7}Sr_{0.3}TiO_3$ in high magnification, respectively. (by Nurxat & Nurxat)

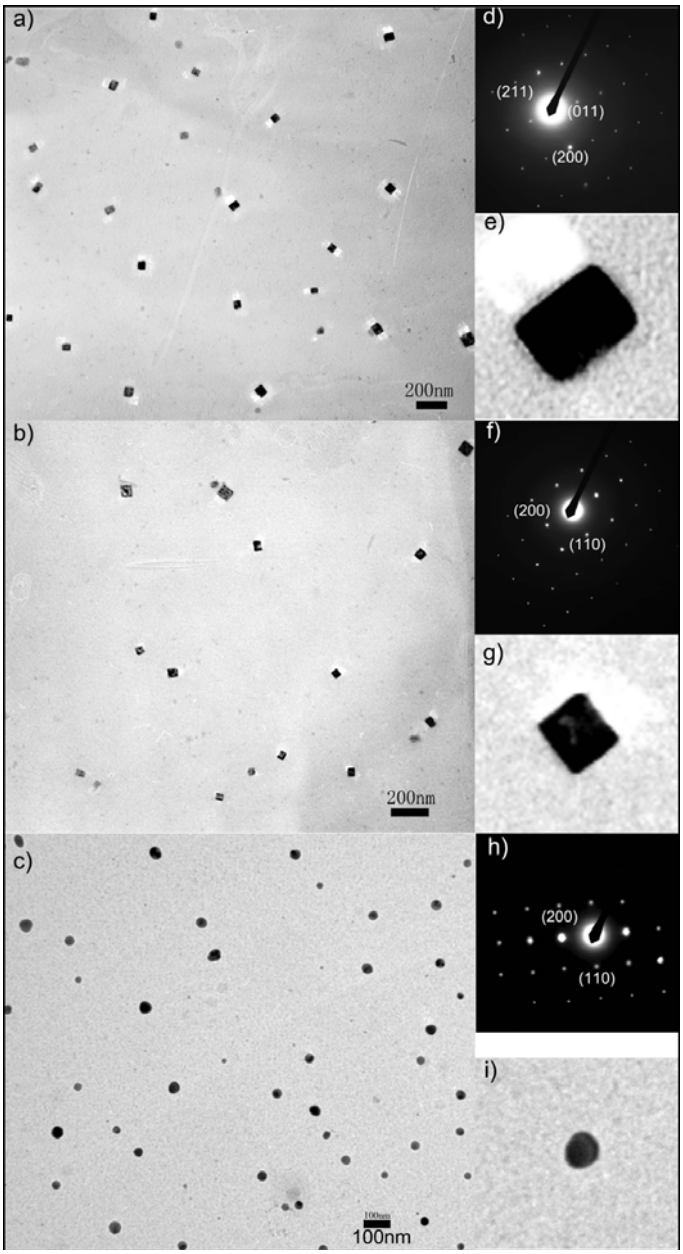

Figure 2.6 TEM images of $Ba_{0.7}Sr_{0.3}TiO_3$ nanoparticles from different synthetic conditions: (a, b) the amount of all aqueous contents equals to 0.5 of the original amount; (c, d) the amount of the aqueous contents equals to 0.25 of the original amount. (by Kai)

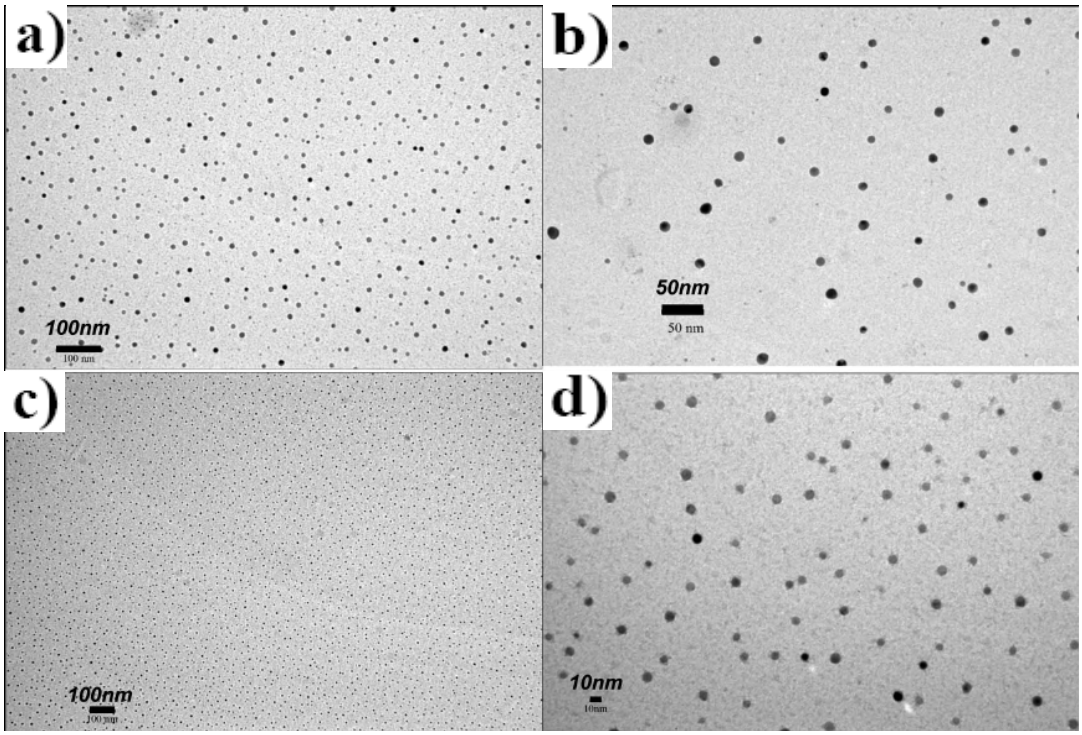

2.4 Conclusion

In summary, an efficient open-bench method has been discovered for the synthesis of high-quality STO and BTO nanocrystals and BST nanosolid solutions with variable compositions and size ranges. The 80 °C temperature of the synthesis process represents nanocrystal formation below the Curie temperature of BTO. This open-bench process allows the direct, facile preparation of BST single nanocrystals with a giant static dielectric constant without a history of thermal stress. The optimized reverse micelle method led to high-quality nanocrystals as supported by XRD, electron diffraction, TEM, FTIR, and EDS data. The shifting of 2θ value at the 200/002 peak reflects the increasing lattice unit dimension with increasing Ba^{2+} molar fraction as expected. Whereas the synthesized $Ba_{0.7}Sr_{0.3}TiO_3$ nanocrystals are spherical in shape, BTO and STOhave tetragonal and cubic shapes, respectively. The size of the BST nanoparticles was shown to be readily tuned from 50 to 10 nm using our reverse micelle approach. These findings can have a significant impact on the development of nanoelectronics. The new procedure does not require demanding conditions such as high temperature, high pressure, and an inert environment and involves only the handling of common components. This simple open-bench method represents an important contribution to the perovskite nanocrystal synthesis methodology.

Chapter 3

Catalytic growth of silica nanoparticles in controlled shapes at planar liquid/liquid interfaces[65]

3.1 Introduction

In recent years, material scientists have extensively investigated novel ways to control the shape of nanoparticles.[66] Controlling shapes of nanoparticles is becoming extremely important in various practical applications since chemical and physical properties of nanoparticles can be tunable by their shapes.[67, 68] For example, different shapes of nanoparticles have different absorption properties so that the shape control can create a new set of colors of nanoparticles in addition to the size, useful for medical imaging. For another application of the shape-controlled nanoparticles in catalysis, when Pt nanoparticles were grown in a tetrahexahedral shape, their catalytic activity was enhanced because these nanoparticles had many high-index facets that served as active sites for breaking chemical bonds.[69] Here we report a novel method to control the shape of nanoparticles by reacting precursors at planar liquid/liquid interfaces. By simply changing the combination of organic and aqueous solvents that formed the interfaces, this interfacial growth technique yielded different shapes of silica nanoparticles in triangle, cube, rod, and rope.

In general, non-spherical nanoparticles can be grown by modulating the relative surface energies between faces of nuclei.[67, 70] While various dry and wet methods have produced nanoparticles in well-defined shapes, wet chemical methods have an advantage to control the shape by influencing growth rates on specific faces of nuclei

at the nucleation stage via capping of these faces with surfactants, ions, and biomolecules.[17, 71-79] In all cases, the shape control becomes more effective when the nucleation and the growth rates slow down so that these surfactants have enough time to absorb particular faces; by this face-selective capping, the growth rate for each face is no longer equal, which could yield non-spherical nanoparticles.

Interfaces between two immiscible liquids such as surfaces of droplets have been shown to be ideal platforms for the assembly of colloidal nanoparticles,[80-83] but there were fewer reports to grow inorganic nanoparticles at planar immiscible interfaces.[84] However, experimental studies of chemical reactions at liquid/liquid interfaces at the microscopic level are still in their infancy and the particle growth at the liquid/liquid interface has not been explored to control the shape.[85, 86] In fact, the planar liquid/liquid interface has a significant potential for the controlled particle growth since this soft interface lacks fixed nucleation sites that give capping ions freedom to target certain faces of nuclei and the interfacial tension retards particle growth rates to control their morphologies.[87] The slowing of nuclear kinetics at the interfaces is caused by the lower stability of small nuclei due to the change in interfacial tension between two different phases.[88] While the slower nucleation kinetics has been observed at planar liquid/liquid interfaces, there are few reports taking this advantage to control the shape of nanoparticles at the interfaces. Here, our strategy for the shape control of nanoparticles is to apply various positive and negative ions at planar liquid/liquid interfaces where the nucleation kinetics are slow enough for these ions to absorb and change the growth rate on particular faces and these face-selective ion absorptions tethered the shape of resulting nanoparticles via hydrolysis and

condensation (Figure 3.1). While silica and other nanoparticles were assembled into various shapes by the surfactant supramolecular assembly method in a bulk single-phase solution,[89, 90] here we report an alternative method for the nanoparticle shape control, the liquid-liquid interfacial nanoparticle growth method. In this report, we selected silica as a model growth system since its growth mechanisms in acid and base catalyses are well characterized. While previously the interfacial synthesis strategy has been applied to grow polymers in controlled morphologies,[85] the application of interfacial growth to inorganic nanoparticle syntheses in controlled shapes has not been explored extensively.

3.2 Experimental

The silica precursor, tetraethyl orthosilicate (TEOS,98%, Sigma-Aldrich) was dissolved in organic solvents, *n*-butanol (Fisher) and $CHCl_3$ (Sigma-Aldrich), in a 1 M concentration. To form the liquid/liquid interface with the *n*-butanol organic layer, first 0.1 M aqueous solution of acid or base, HCl, HNO_3 (Fisher), NH_4OH (Sigma-Aldrich), or NaOH (Acros Organics), was added to a vial, and then 5 ml of the TEOS/*n*-butanol solution was added slowly along the wall of the vial without disturbing the interface. In these interfacial systems, the organic phase of *n*-butanol located at the top layer. To form the liquid/liquid interface with the $CHCl_3$ organic layer, first 5 ml of the TEOS/$CHCl_3$ solution was added to a vial, and then 5 ml of the 0.1M HCl solution was added slowly along the wall of the vial without disturbing the interface. In these interfacial systems, the organic phase of $CHCl_3$ located at the bottom layer. After two days, aqueous layers containing silica nanoparticles were washed and centrifuged. Silica nanoparticles extracted in the aqueous layers were

then dried on carbon coated copper grids at room temperature for TEM and electron diffraction measurements at an acceleration voltage of 100kV (JEOL 1200 EX).

3.3 Results and Discussion

In this planar liquid/liquid interfacial growth of silica, the Si precursor (TEOS) and catalysts were loaded in different layers; TEOS in an organic layer and catalysts in an aqueous layer. As the alkoxide precursor from the organic phase contacted and reacted with catalysts at the liquid/liquid interfaces, silica particles were formed by hydrolysis and condensation. The intermediate species condensed from silanol $[Si(OH)_n]_m$ clusters were hydrophilic and therefore the growth of silica nanoparticles was driven in the direction from the organic layer to the aqueous layer. The interfacial experiments were established under five different conditions with TEOS as the precursors. In the interfacial syntheses with the acid catalysis, HCl or HNO_3 solution was employed as the aqueous phase and *n*-butanol as the organic phase. In the interfacial syntheses with the base catalysis, we applied NaOH or NH_4OH as the aqueous phase and *n*-butanol as the organic phase. Chloroform was also applied as the organic phase to further slow down the growth rate of silica at the liquid/liquid interfaces.

Figure 3.1 Illustration of the scheme to grow silica in various shapes at planar liquid-liquid interface. Aqueous phase contains ions that not only catalyze the condensation but also cap the specific face of nuclei at slow particle growth at the interface.

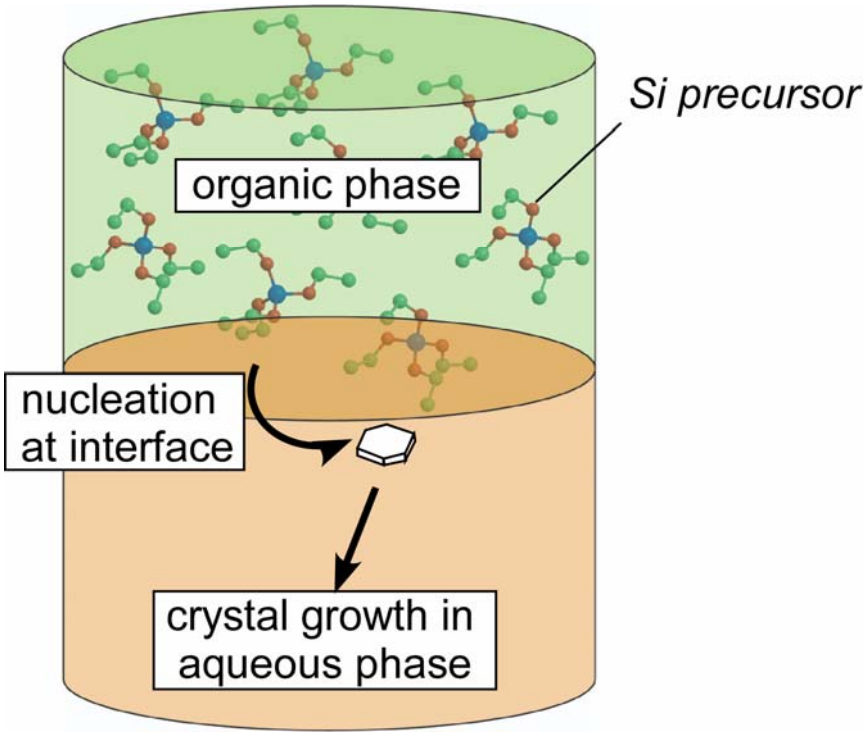

With the acid catalysis, the hydrolysis of the TEOS precursor without the interface by stirring the solution yielded branched silica wires as shown in Figure 3.2(a). This branched wire growth without any particular shape controls was also observed in sol-gel growth methods in homogeneous solutions containing the acid catalysis.[90] However, the shape of silica particles was changed as the precursor was hydrolyzed at the liquid/liquid interface between the organic phase and the aqueous phase. When the TEOS precursor was in the *n*-butanol (top layer) and the acid catalyst HCl was in the aqueous phase (bottom layer), silica nanorods with 40nm in width and several micrometers in length were readily formed toward the aqueous layer (Figure 3.2(b)).

While these nanowires formed at the liquid/liquid interfaces were not branched out as observed in the homogeneous sol-gel system, the formation for the similar elongated structure between them indicates that the shape control of silica nanoparticles with the HCl/butanol interfacial systems have weak influence on their shapes. This is due to the fast silica condensation with the acid catalysts and under this condition ions at the interface have little time to influence the shape of silica nanoparticles by absorbing specific faces of silica nuclei.

However, striking difference was observed when the organic solvent containing TEOS precursors was changed from *n*-butanol to chloroform for the interfacial silica growth with the acid catalysis. In this case, the TEOS precursor in chloroform phase in the bottom layer was hydrolyzed at the interface by the acid catalyst HCl originated from the aqueous phase in the top layer, which is the reversed configuration of the HCl/butanol interface. This HCl/$CHCl_3$ interface produced triangle-shaped silica nanoparticles as shown in Figure 3.2 (c). The triangular nanoparticle was 200±20 nm on a side. It should be noted that there were areas on TEM grids where the spherical form of silica is more dominant. The electron diffraction pattern (inset of Figure 3.2 (c) showed the polycrystalline nature of nanoparticles and these silica nanoparticles could contain the α-quartz domain based on this diffraction pattern. Although the condensation was still the rate-determining step in the acid catalytic interface, the aprotic organic solvent, $CHCl_3$, made a significant impact on the nucleation kinetics on specific nucleus faces otherwise silica nanoparticles should not grow in a particularly defined shape. The major difference by applying $CHCl_3$ as the organic layer is the silica growth rate at the interface. In order for the silica growth, silanols from the organic

layer of chloroform need to cross the interface toward the aqueous layer and undergo the condensation, however $CHCl_3$ could retard the transfer from the organic to the aqueous layers since this aprotic solvent hydrogen bonds to electrophillic deprotonated silanols at the acidic interface.[91] Due to this reduced rate of overall condensation reaction, chlorine ions at the interface have enough time to selectively adsorb onto certain faces of silica nanoparticles at the nucleation, which controls the shape of resulting particles. Previously, the adsorption of chlorine ions onto the <111> face produced triangular Cu nanoparticles,[92] and the triangular silica nanoparticle grown at the interface between the $CHCl_3$ organic layer and the HCl aqueous layer could undergo the same shape-control mechanism. It should be noted that the control experiment in Figure 3.2(a) to fail growing the shaped particles in a bulk solution without the interface suggests that the interface play an important role on the particle shape; If those particles are simply grown by means of the salt condensation during the drying process, we should observe the triangle particles when the bulk solution of precursors and catalysts were dried.

Figure 3.2 TEM images of (a) silica grown with no interface by stirring the aqueous solution of HCl (b) silica grown at the HCl/butanol interface (c) silica grown at the HCl/$CHCl_3$ interface (right: magnified TEM image, scale bar = 100 nm). Scale bar = 200nm. Insets show the electron diffraction patterns.(by Nurxat)

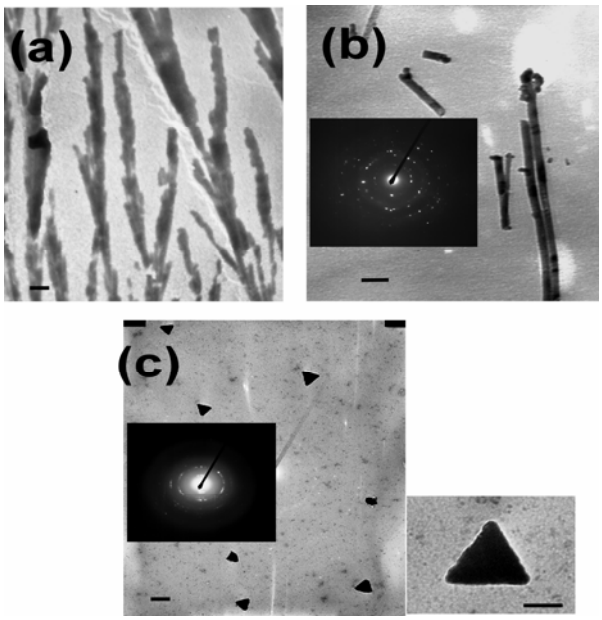

When the TEOS precursor was hydrolyzed in homogeneous media with the base catalysis without the interface by stirring the solution, large polydisperse silica particles were grown as shown in Figure 3.3(a). This type of amorphous particle growth without any particular shape controls was also observed previously in homogeneous sol-gel growth methods with the base catalysis. However, when silica was grown at the liquid/liquid interface with the base catalyst, NaOH, in aqueous layer and the TEOS precursor in the organic layer of *n*-butanol, the shape of nanoparticles was cubic and the average size of the cubic nanoparticles was 100±10 nm on a side (Figure 3.3(b). Some of nanoparticles in Figure 3.3(b) were in a rectangular form since two cubic nanoparticles aggregated side by side. The diffraction pattern in Figure 3.3(b) indicates that this silica nanoparticle is more crystalline as compared to the triangle particles

produced at the $HCl/CHCl_3$ interface, and the pattern has a close match with α-crystabolite. When NH_4OH was applied as a base catalyst in aqueous layer, the polydisperse spherical nanoparticles appeared and their structure was amorphous. Since polydisperse spherical nanoparticles grown at the NH_4OH/butanol interface resembles the nanoparticles grown without the interface, the NH_4OH catalyst at the liquid/liquid interface has no influence on the shape of silica. In the case of the base catalytic growth, *n*-butanol and chloroform yielded the same particle shape at the interface. Among the interfaces with the base catalysts, only NaOH/butanol interfacial system tethered the particle shape to cubic because stronger base NaOH produced higher ion concentrations at the interface, which can cap certain faces of silica nuclei more effectively to control the shape of resulting silica nanoparticles. Previously, the shape of titania nanoparticles was controlled by capping them with Me_4N^+. This small cation could stabilize negative charges of titania at the nucleation stage via the electrostatic interaction and yielded titania nanoparticles with defined shapes.[93] Sodium oleate and sodium stearate could also control the shape of titania nanoparticles to cubic by capping <100> and <001> faces.[94] For this interfacial growth of silica with the base catalysis, abundant sodium ions at the NaOH/butanol interface could influence the silica growth on these faces under the characteristic slow condensation at the liquid/liquid interface. Since the influence of the NH_4OH/butanol interface on the particle shape of silica is much weaker than the NaOH/butanol interface, the cationic concentration is also important in addition to the slowing growth kinetics to control the shape of nanoparticles at the liquid/liquid interfaces. It should be noted that the same phenomena was observed as

the lower anionic concentration at the weak acid/$CHCl_3$ interface failed to influence the shape of silica nanoparticles.

Figure 3.3 TEM images of (a) silica grown with no interface by stirring the aqueous solution of NaOH, scale bar = 200 nm (b) silica grown at the NaOH/butanol interface, scale bar = 70 nm (right inset: magnified TEM image, scale bar = 50 nm, left inset: the electron diffraction pattern) (c) silica grown at the NH_4OH/butanol interface, scale bar = 200 nm. (by Nurxat & Kai)

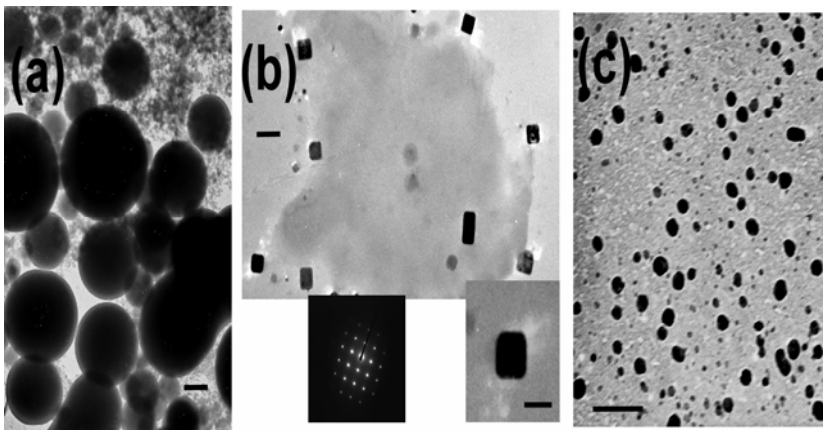

3.4 Conclusion

In summary, negative and positive ions at the liquid/liquid interfaces could change the growth rates on specific faces of silica nanoparticles under the slow nucleation condition and this interfacial growth technique yielded different shapes of silica nanoparticles in triangle, cube, rod, and rope by simply changing the combination of organic and aqueous solvents that formed the interfaces. The aim of this study is to

demonstrate that the particle shape can be changed at the liquid-liquid interface when the shape cannot be controlled at the same condition in the bulk single-phase solution. The interfacial synthesis has an advantage to slow the particle growth, which increases the probability for surfactants and ions to influence the resulting shapes. Silica was used as a model in this study, and this interfacial method will become more practical if the same shape control can be achieved for more important materials such as quantum dots. In theory, this interfacial synthesis should be applicable to control the shapes of various inorganic nanoparticles whose precursors can be dissolved in organic and catalysts or reducing agents in aqueous solutions, respectively. Therefore, this interfacial growth method has a potential to tether the shape of inorganic nanoparticles without using complex multiple synthetic processes. It should be noted that this method enables one to not only tether nanoparticle shapes but also provide means to investigate the effect of solvents on fundamental inorganic nanoparticle growth mechanisms under controlled environments. At last, we would like to emphasize that our interfacial method can be served as an alternative method to the existing colloidal synthesis for the shape control of nanoparticles, and there is a potential that our interfacial method could be applied controlling the shape of some systems whose shape is difficult to change by traditional colloidal methods. And the combination of those two methods could enhance the precision of the shape control.

Chapter 4

Single Crystalline Organic Nanoneedles with Fast Conductance Switching Properties from An Interfacial Polymerization-Crystallization of Conjugated Monomers[85]

4.1 Introduction

Science at the nanoscale has been one of the most exciting areas of recent investigation, with activities that are of both fundamental and technological significance. New physical phenomena and revolutionary nanoeletronic devices based on novel nanomaterials are anticipated. Organic conjugated systems have been successfully applied to electronics because of their versatile electronic properties and their adaptability to a broad range of processing methods.[95-108] However, the development of *polymer electronics at the nanoscale* is in its infancy. Here we report the first synthesis of polythiophene nanoneedles that exhibit fast, field-induced conductance switching in a single nanocrystalline element.

Most bulk conducting polymer systems studied consist of regions of inhomogeneity. The investigation of the processes in the nano-domain representing pure crystals is critical in ascertaining the inherent electronic properties of polymer nano-elements. Single *nano*crystals of conducting polymer have not been reported, although needle-shaped bulk crystals of quaterphenyl cation radical salt were previously studied,[109] and highly ordered polymer structures were prepared by methods including electrochemical epitaxial polymerization,[104] solution spin-coating

on functionalized surface,[110] and solid-state polymerization of monomer crystals.[111] To date, polythiophenes together with polyanilines and polypyrroles represent the most important group of conducting polymers.[112] Applying an interfacial polymerization-crystallization process, we have prepared single crystals of poly(3, 4-ethylenedioxythiophene) (PEDOT) in a nanoneedle form. The aqueous/organic interfacial system used was composed of 3, 4-ethylenedioxythiophene (EDOT) in an organic solvent and an oxidant, ferric chloride ($FeCl_3$), in DI water. The use of ferric chloride as oxidant in the precipitation polymerization of thiophenes has been documented.[113-115] In such cases, polymer chains are generally formed first, followed by precipitation formation of crystals. Our system represents the first use of ferric chloride in the interfacial polymerization of thiophenes. This polymerization proceeds with an attendant crystal growth, thus higher order of crystal packing can be expected.

The liquid/liquid interfacial crystallization could be applied to produce polyaniline (PANI) nanocrystals and polypyrrole (PPY) nanocrystals, in addition to PEDOT nanocrystals. This technique will provide a general route to synthesize conducting polymers via oxidative coupling processes in a single crystal state, which is extremely difficult to achieve by other synthetic methods.

4.2 Conducting Nanoneedle Growth of poly(3,4 ethylenedioxythiophene) (PEDOT)

4.2.1 Experimental

4.2.1.1 Interfacial Polymerization of 3, 4-ethylenedioxythiophene (EDOT)

All reagents for synthetic procedures were purchased from Aldrich Chemical Co. and used without further purification. In the interfacial synthesis, EDOT or 3-hexylthiophene (3HT) (1mg/mL) was dissolved in dichloromethane (DCM), pentane or n-butanol, and ferric chloride (1mg/mL) in DI water. The interfacial polymerization was conducted in a 20-mL vial containing 5mL monomer solution and 5mL $FeCl_3$ solution. The water layers were collected after 48 hours (scheme 4.1).

4.2.1.2 Purification of Nanoneedle Solution by dialysis

Five drops of concentrated HCl solution (37%) were added into the collected suspension. The nanoneedle suspension was then centrifuged and re-suspended three times followed by a final dialysis process for 10 hours using a dialysis tubing (D9277, Sigma-Aldrich) in ultrapure water (resistivity: 18.2 MΩ cm, total organic carbon levels: 10 ppb).

4.2.1.3 Characterization by TEM, Electron Diffraction, HRTEM, SEM/EDS, EPR, and STM/STS

After the purification, the aqueous suspension was 10-fold diluted for the transmittance electron microscopy (TEM), electron diffraction, high-resolution TEM

(HRTEM), Energy dispersive X-ray spectroscopy (EDS), electron paramagnetic resonance (EPR) and scanning tunnelling microscopy/spectroscopy (STM/STS) characterizations. TEM and electron diffraction were conducted on a JEOL 1200 EX microscope. HRTEM was conducted on a Tecnai G2 F20 cryoelectron microscope. EDS studies were conducted on an Amray 1910 microscope combined with a Noran system SIX X-ray microanalysis system (Thermo Electron Corporation). EPR spectrum was recorded on a Bruker EPR ESP 380E spectrometer. STM/STS studies were conducted on a PicoSPM II system (Molecular Imaging). For the STM/STS sample preparation, the diluted nanoneedle suspension was spin-coated onto an Au-111 surface (purchased from Molecular Imaging), which was freshly annealed by the provider and used immediately after delivery. Ir/Pt STM tips were purchased from Molecular Imaging and used for all the STM/STS measurement.

4.2.1.4 Sample Preparation for SEM/TEM

The purified PEDOT nanoneedle suspension was first dried under ambient conditions for 10 days and then dried in vacuo at room temperature. Dark green PEDOT powders was collected and examined by SEM/EDS for the morphological and chemical composition study of the self-assemblies from PEDOT nanoneedles.

4.2.2 Results and Discussion

In a typical synthesis, EDOT dissolved in dichloromethane (DCM, 5 mL, 1 $mgmL^{-1}$) served as the lower organic layer, and $FeCl_3$ dissolved in DI water (5 mL, 1 $mgmL^{-1}$) formed the upper layer. After 2 days, the aqueous layer was carefully collected for

purification (scheme 4.1). To prevent the hydrolysis of $FeCl_3$, 5 drops of concentrated HCl (37%) were added to the collected suspension. The nanoneedle suspension was then centrifuged, and the precipitate was re-suspended. This process was repeated twice and was followed by a final dialysis step in ultrapure water (resistivity 18.2 MΩ cm, total organic carbon level 10 ppb) for 10 h. The oxidative coupling polymerization of EDOT at the aqueous/organic interface was facilitated by $FeCl_3$[116] and is an example of a system in which crystallization in the nanoregime occurs during polymerization. The oxidative coupling of EDOT was much slower than the fabrication of polyaniline (PANI) nanofibers using a similar process.[117] The PEDOT nanoneedle samples were usually collected after 48 h, while the formation of PANI nanofibers using persulfate as the oxidant required at most 10 min. Unlike a typical solution polymerization step, which leads to the formation of insoluble crystals, this slow-coupling polymerization involves an interface, which mediates the development of superior crystal packing in the product. The nanocrystals comprise different chain lengths of PEDOT, as expected from their needle shape, with inner chains longer than the outer ones. The 50 nm length of the nanoneedles indicates that the longest chain contains 126 monomer units (thiophene rings). However, it is also possible that there may be multiple chains stacked tip-to-tip. Because of the very limited solubility of the crystals, the polymer size distribution could not be measured at this time.

Conducting-polymer samples are considered, in general, to be inhomogeneous systems with isolated crystalline domains.[118, 119] The structural order of polythiophene and its derivatives could be very complicated.[119-123] To obtain a highly crystalline conducting-polymer sample, special techniques must be applied. For

example, highly crystalline polythiophene can be obtained by a coupling reaction involving preorganized monomer crystals.[111] The PEDOT products from our system are clearly nanoneedles that are approximately 15 nm wide and 50 nm long with pointed tips (Figure 4.1a and b). To the best of our knowledge, this is the first example of a needle-shaped, nanocrystalline conducting-polymer structure. The initial formation of PEDOT nanoneedles most likely occurs at the aqueous/organic interface, and they subsequently migrate to the aqueous phase as the nanoneedles grow. To determine the extent to which this interfacial polymerization system can be applied, pentane was used in place of DCM as the organic layer for EDOT monomers. In this case, the organic phase formed the upper layer, and as they grew, the nanoneedles migrated down into the aqueous phase. Transmission electron microscopy (TEM) images (Figure 4.2 and 4.3) show similar nanoneedle structures, but the tips of the nanoneedles are not as sharp as those obtained from DCM.

Although varying lattice parameters were obtained for PEDOT depending upon the synthesis, the polymorphs can be assigned as an orthorhombic lattice.[122, 123] The lattice constants *a*, *b*, and *c* are designated as the lateral chain spacing, the p–p stacking distance, and the length of the repeat units, respectively. High-resolution (HR)TEM images (Figure 4.1c) and electron diffraction (Figure 4.1d) data obtained from the sample shown in Figure 4.1a indicate an exceptionally high level of order and provide additional structural details. The HRTEM image clearly shows the lattice structure of the nanoneedle. The lattice distance was assigned as the lateral chain spacing, *a*. The electron diffraction pattern shows well-defined diffraction spots, indicating that the nanoneedles are highly ordered single crystals. Table 4.1 gives the

calculated lattice distances from the electron diffraction spots. From this data, the determined *a*, *b*, and *c* lattice parameters are 0.584 (confirmed by HRTEM, Figure 4.1c), 0.494, and 0.796 nm, respectively. The p–p stacking distance, *b*, is at the low end of the reported range 0.425 to 0.68 nm.[120, 122, 123] The lateral chain spacing, *a*, is very small when compared to the range 1.3–1.5 nm reported for PEDOT with external dopants of different sizes and concentrations.[122, 123] The factors contributing to the short p–p stacking distance and the close lateral spacing include the favorable packing of the incoming monomers on the crystal template and the absence of an external dopant. Energy dispersive X-ray spectroscopy (EDS) data (Figure 4.5 and Table 4.2) support a C/O/S ratio of 6:2:1 and, on average, confirm the presence of one chloride anion for 54 thiophene rings without any observable iron present. Because there was no external doping, chloride anions serve the role of charge compensators. The chains likely consist of macroradical cations and neutral PEDOT depending on whether oxidation or deprotonation is the last step of chain growth.[116] Therefore, the maximum number of thiophene rings per PEDOT chain is 54, which indicates a low-molecular- weight polymer that is still larger than an oligomer. In the acidic environment of the polymerization system (pH 2.45 in the aqueous phase) and in the absence of a proton acceptor in the media, cation radicals should explain most of the charged state of the chains. Sub-micrometer hematite needles were observed by aging $FeCl_3$ in NaH_2PO_4 buffer at 100 °C for 3 days.[124] For our organic nanoneedles, the electron paramagnetic resonance (EPR) spectrum (Figure 4.6) clearly shows the characteristics of PEDOT (linewidth is ca. 3.9 G, g-value is ca. 2.0083) without observable hematite. The presence of hematite would be readily observable as a very

intense EPR signal at a *g*-value of ca. 2.04 with a broad linewidth of ca. 500 G.[125] The analytical results from TEM, HRTEM, electron diffraction, EDS, and EPR converge to support the preparation of single-crystal PEDOT nanoneedles exhibiting a close p–p stacking distance and a small lateral separation. A schematic representation of the polymer chain arrangement with 15 monomer units per neutral segment in the nanoneedle is illustrated in Figure 4.4. Absent is the chloride anion, the charge compensator, which is present for every 54 monomer units (S/Cl atomic ratio = 54 from EDS data; Figure 4.5 and Table 4.2). Because of their special morphology and unique crystalline structure, including a small p–p stacking distance and a short lateral separation, these nanoneedles show novel electronic properties. Using scanning tunneling microscopy/spectroscopy (STM/STS), we studied their electronic conducting behaviors and discovered a field-induced conductance switching with response times in the millisecond regime.The first reported conducting-polymer switch was based on polyaniline nanojunctions electrochemically synthesized as the bridge between gold electrodes.[101] Abrupt switching behavior behavior was observed when the electrode gap narrowed to 1 nm. It was hypothesized that the abrupt switching was due to the formation of single crystalline domains, although the crystalline nature of the junction was not experimentally verified. For PEDOT STM/STS studies, the purified suspension was diluted ten fold with ultrapure water and spin-coated onto a gold(111) surface. Typical STM/STS results are shown in Figure 4.7. STM images were obtained for individual nanoneedles (Fig. 4.7b); following imaging, the STM tip was positioned in the middle of a nanoneedle for STS analysis. The tunneling current–voltage (*I*–*V*) curves, Figure 3a, were recorded from a –4 to 4 V bias range for both the

PEDOT needles and the gold substrate. The gold (111) surface, as a reference, showed typical metallic tunneling *I*–*V* behavior. Unlike the gold surface, PEDOT nanoneedles exhibited abrupt switching behaviors near –3 and 3 V. The conductance behavior most likely involves electron transport along the p–p stacking direction of the PEDOT nanoneedle. The plateau region from –3 to 3 V can be assigned as the OFF or insulating state (tunneling current < 0.04 nA) of the switch. When the bias voltage increased to 3 V, the tunneling current abruptly jumped to a saturated amplitude (tunneling current > 10 nA). The two regions beyond –3 and 3 V are the ON or highly conducting state of the switch. The switching process took place on the order of milliseconds, which is comparable to switching times for molecular switches.[126] At low applied field (0–3 V), the barrier was high enough to prevent the passage of tunneling current through PEDOT, and the switching-off process took over. The reproducibility of the STS behavior was established by the investigation on an ensemble of 12 individual nanoneedles (Figure 4.8 ; switch-off and switch-on bias voltages and their standard deviations, Table 4.3). This noncontact measurement on nanocrystals in the absence of an external dopant differs inherently from the contact measurement on highly doped and charged conjugate bulk systems in that in the present case, we monitor tunneling current.[127]

4.2.3 Conclusion

In summary, single-crystalline PEDOT nanoneedles exhibiting fast conductance switching were synthesized for the first time using an interfacial polymerization process that occurs with simultaneous crystallization. The pointed nanoneedles obtained from this synthesis are, on average, 50 nm long and 15 nm wide. Orthorhombic lattice units

were assigned to single nanocrystals, and these values indicated closer p–p stacking distances and lateral separations than observed in most PEDOT systems. The absence of an external dopant and crystallization during chain growth leads to closely packed crystals, a condition contributing to conductance. These nanoneedles show novel switching behavior with a response time of milliseconds. The discovery of the new nanomaterial reported here can contribute to nanoelectronics by advancing fundamental understanding and providing a foundation for the development of novel organic nanoelements.

Scheme 4.1 Synthetic scheme of the interfacial polymerization-crystallization of EDOT mediated by ferric chloride from the water/DCM system.

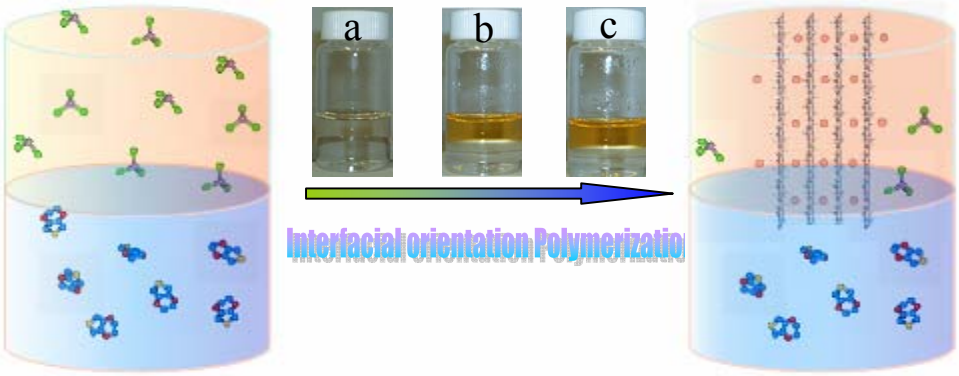

Figure 4.1 PEDOT nanocrystals. **(a)** TEM image; **(b)** Single nanoneedle image; **(c)** HRTEM; and **(d)** Electron diffraction. Scale bar=200nm in a, 20nm in **(b)** The arrows in **(c)** show the chain spacing distance of 0.6nm, which was confirmed by the electron diffraction results (*a*=0.584nm, in **Figure 4.4** and **Table 4.1**).(by Kai & Nurxat)

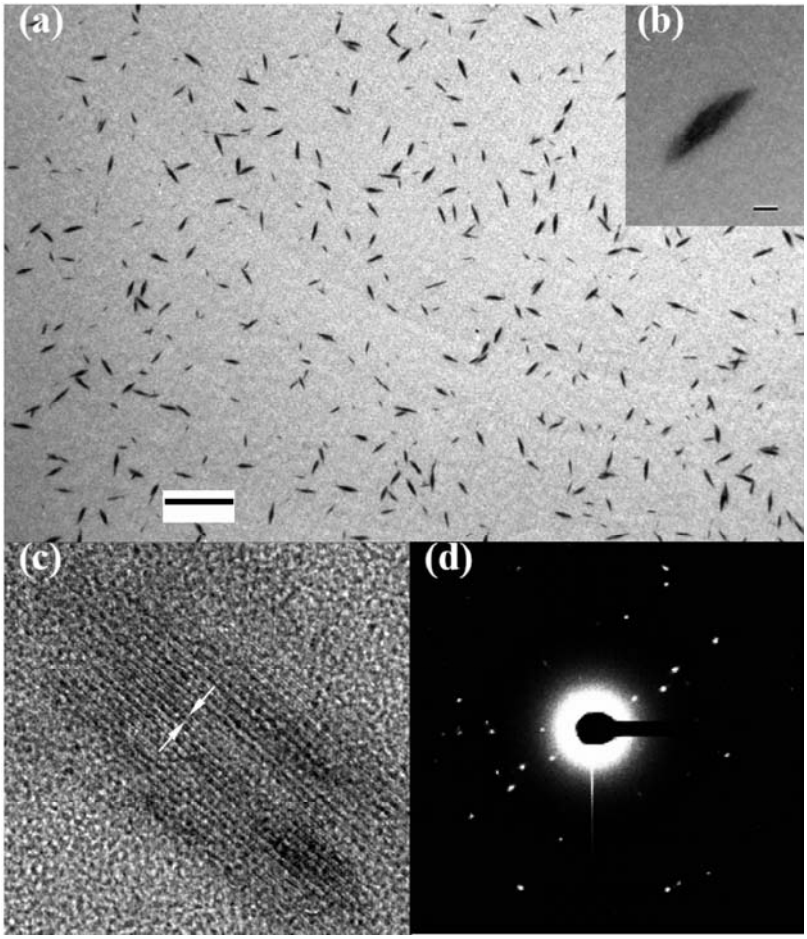

Figure 4.2 TEM images of PEDOT nanoneedles synthesized using pentane as the organic upper layer. Scale bar= (a)1µm, (b)100nm. (by Kai)

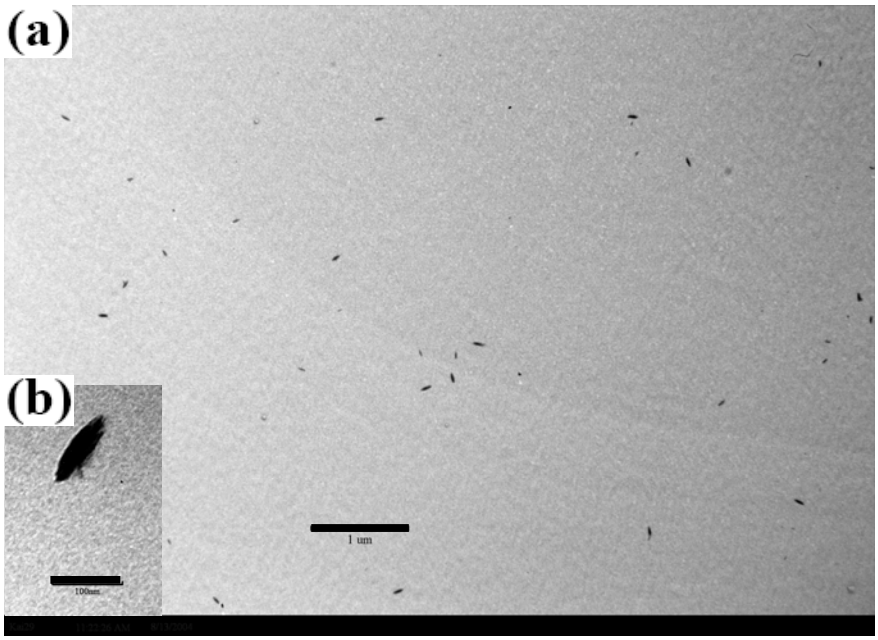

Figure 4.3 TEM images of PEDOT nanoneedles synthesized using n-butanol as the organic upper layer. Scale bar= **(a)** 1µm, **(b)** 100nm. (by Kai)

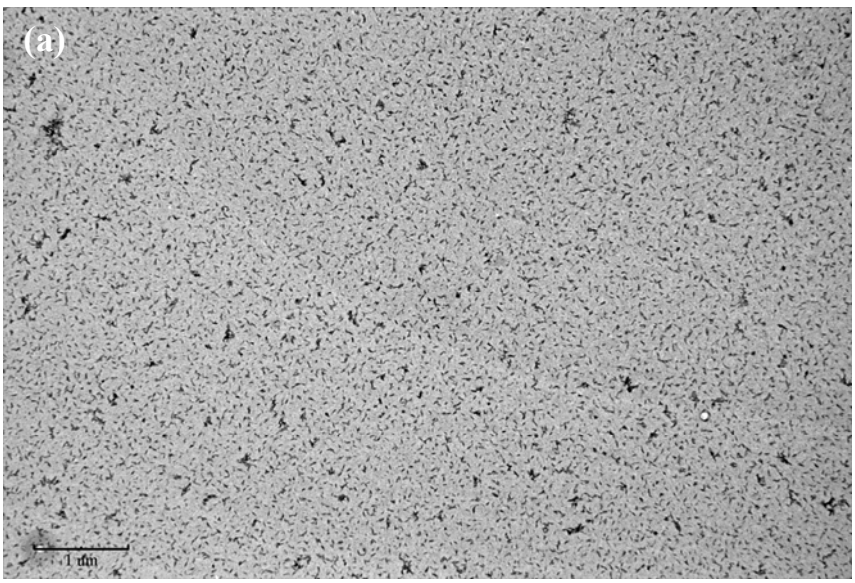

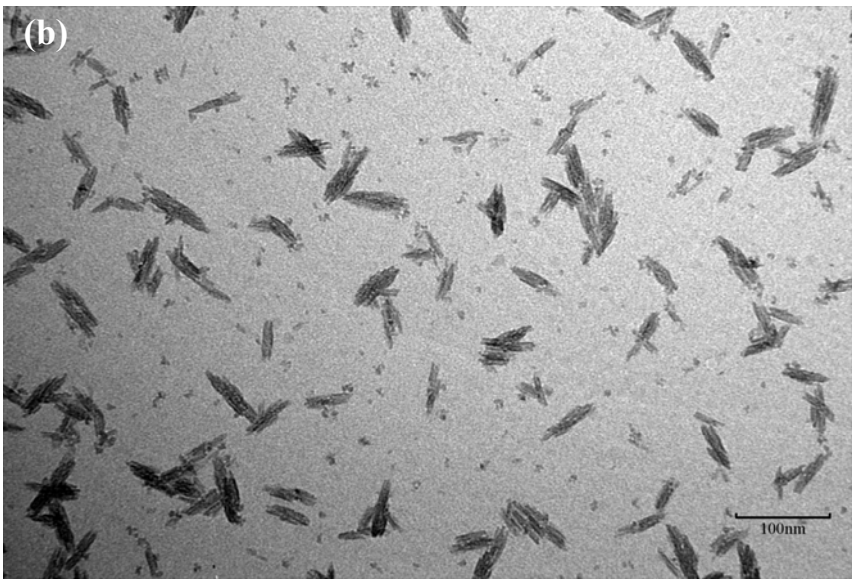
(b)
100nm

Figure 4.4 Schematic representation of chain arrangement for PEDOT nanoneedle with eight PEDOT segments, each with 15 monomer unit, representing partial chains. Not shown is one Cl^- anion, a charge compensator, for every 54 monomer units (S/Cl atomic ratio of 54 in EDS data in **Figure 4.5**). The chains are likely composed of macroradical cation as well as neutral PEDOT depending on the nature of the last step of propagation. As represented in the orthorhombic lattice units: lateral chain spacing a=0.584nm, π-π stacking distance b=0.494nm, and repeating unit distance c=0.796nm.

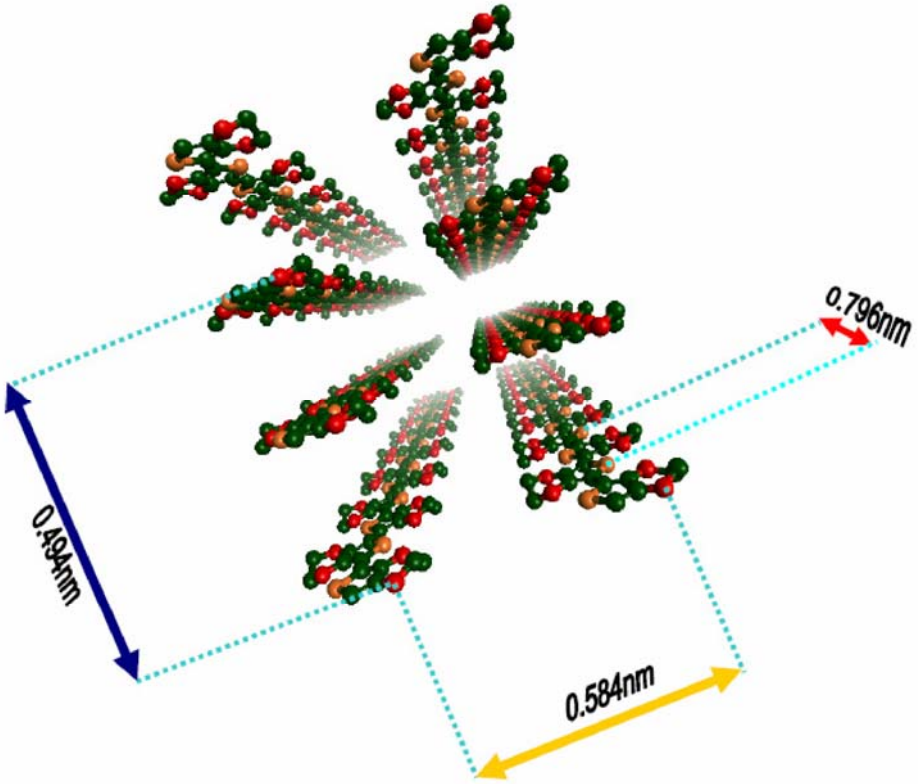

Table 4.1 Lattice assignment of diffraction pattern.

***d*(nm)**	**Indices**
0.796	001
0.584	100
0.494	010
0.427	-
0.398	002
0.344	-
0.292	200
0.265	003
0.231	020

Figure 4.5 EDS spectrum for PEDOT from interfacial crystallization-polymerization. The purified PEDOT sample was deposited on a silicon wafer cleaned by using an UV-ozone cleaner followed by an ultrasonication in HPLC grade methanol. The quantitative result shows a C/O/S ratio of 66.5/21.2/11.8, supporting the theoretical atomic ratio of 6/2/1. The S/Cl atomic ratio of 54 indicates that every 54 monomer units share one Cl^- as a charge compensator.(by Kai & Nurxat)

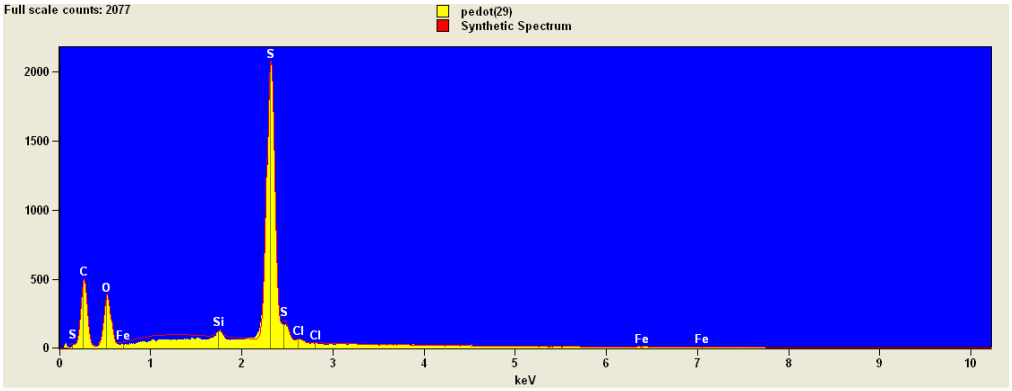

Table 4.2 Quantitative Results.

Filter Fit Chi Squared: 1.116; Correction Method: ZAF; Acc.Voltage: 12.0 kV.

Element	*Net Counts*	*Weight %*	*Atom %*	*Compnd %*	*Norm. Compnd%*
C	4143	52.15	66.51	52.15	52.15
O	3271	22.14	21.19	22.14	22.14
Si	746	0.56	0.31	0.56	0.56
S	25291	24.64	11.77	24.64	24.64
S	0	---	---	---	---
Cl	380	0.51	0.22	0.51	0.51
Cl	0	---	---	---	---
Fe	54	---	---	---	---
Fe	0	0.00	0.00	0.00	0.00
Total		100.00	100.00	100.00	100.00

Figure 4.6 First-derivative EPR spectrum of PEDOT nanoneedle at room temperature (linewidth ~3.9G; g-value ~2.0083); with Mn^{2+} marker signals, 3rd and 4th line signals.(by Kai & Lingzhi)

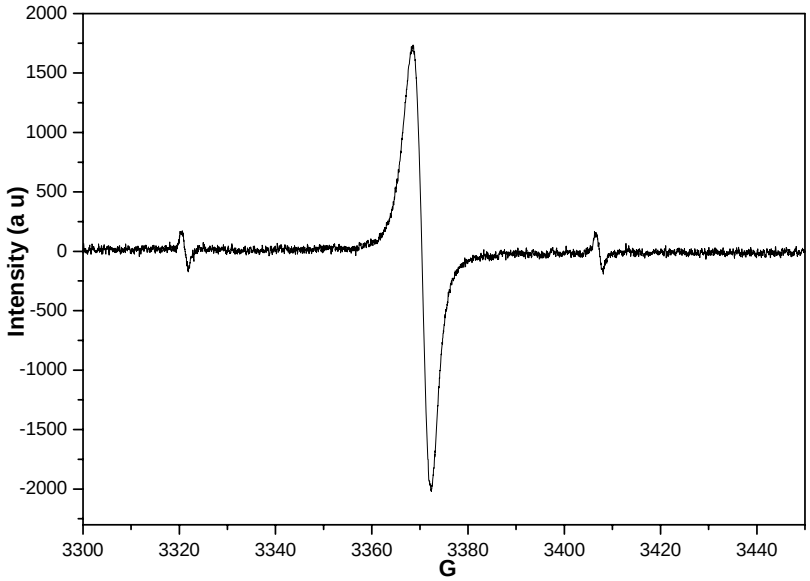

Figure 4.7 Representative switching behavior of the nanoneedle. a) The STS experiments were conducted on STM scanner (PicoSPM II, Molecular Imaging). The yellow square data points show a typical tunneling I-V curve of Gold-111. The red square data points show the tunneling I-V curve of a PEDOT nanoneedle. The plateau between -3 and +3 volts was assigned as the *OFF* (low conductance) state and the two regions beyond ±3 volts were assigned as the *ON* (high conductance) states. The sweep time for both the curves was 10 seconds. Two hundred data points were collected for each curve. The I-V measurement on a single needle can be repeated many times. The switching response was estimated to be in the millisecond time scale. STM experiments were conducted on the same instrument using a constant current (100pA) mode at a low servo level (servo gain %: I=0.3, P=0.1). b) A representative STM topological image was collected at the scanning rate of 0.5Hz, 8.5 minutes per frame. The bias voltage is 0.1 volts. The scale bar = 80nm.(by Nurxat & Kai)

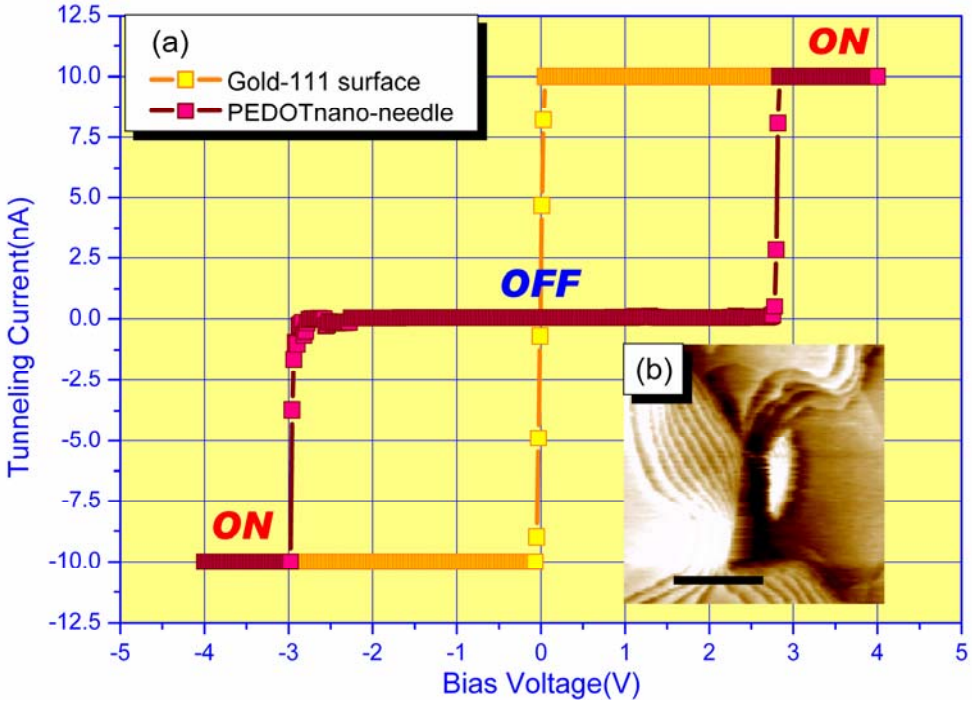

Figure 4.8 STS from twelve different nanoneedles. The Switch-on and Switch-off voltages and the standard deviations were tabulated in **Table 4.3**. Similar STS/STM results were also reproduced in DI's instrument (Veeco's Nanoscope IIIa, St. Barbara, CA). The parameters are the same as that used in MI's instrument. It should be noted that, in DI's instrument, the use of the instrument parameters stated in **Figure 4.7** is stipulated as "constant-height" mode because of the low servo gain setting.(by Kai & Nurxat)

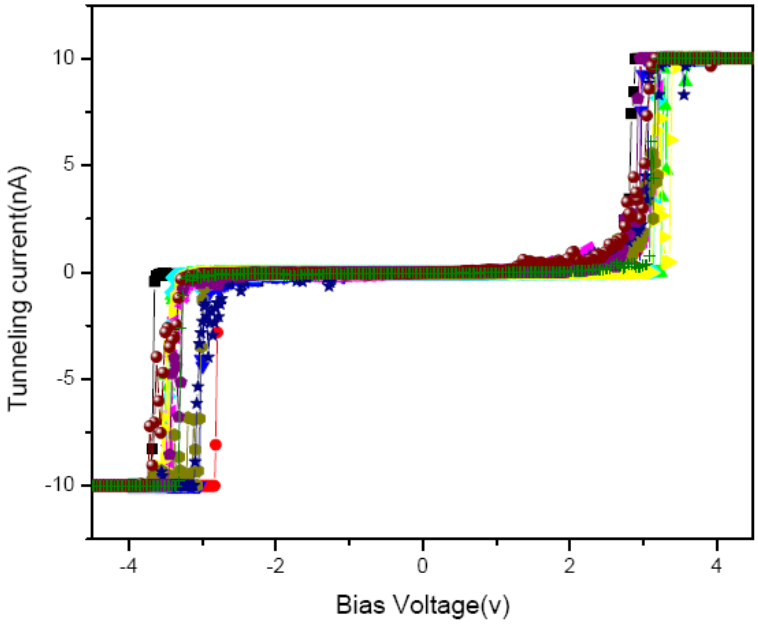

Table 4.3 The Switch-on and Switch-off voltages and their standard deviations.

Curves	Switch-off voltage (v)	Switch-on voltage (v)
1	-3.28	3.11
2	-3.37	2.96
3	-3.34	2.86
4	-2.92	2.98
5	-3.01	3.03
6	-3.37	3.12
7	-3.32	2.94
8	-3.44	3.16
9	-2.95	2.96
10	-3.42	3.25
11	-3.66	2.77
12	-2.81	2.96
Average voltage(v)	-3.24	3.01
Standard deviation (v)	0.257	0.133

4.3 Conducting Nanoneedle Growth of PolyAniline (PANI) and Poly Pyrrole (PPY)[128]

In previous chapter, we discussed the first synthesis of single crystalline conducting polythiophenes, poly(3,4-ethylenedioxythiophene)(PEDOT) with the fast conductance switching property using an interfacial polymerization-crystallization process.[85] An important growth condition necessary to yield highly crystalline conductive polymers was the extended crystallization time at the liquid/liquid interfaces to increase the degree of crystallization. As compared to other interfacial polymerization methods, lower concentrations of monomer and oxidant solutions were employed to further extend the crystallization time.[129] While other interfacial growth of conducting polymers yielded non-crystalline polymer fibers, our interfacial method produced single crystalline PEDOT nanocrystals in the dimension of 15 nm x 50 nm. These nanocrystals displayed the conductance switching behavior between the insulating and conducting state as potentials were applied, and the abrupt changes of the conductivity occurred at ±3.0 V. [85]

In order to demonstrate that our technique could be applied as the general fabrication procedure for the single crystalline conducting polymer growth and the resulting crystalline polymers have the fast conductance switching time between the insulating and conducting state comparable to the switching time of molecular switch, this liquid/liquid interfacial method needs to be extended to other conductive polymer nanocrystal syntheses. To test this hypothesis, we demonstrated in this report that the liquid/liquid interfacial crystallization could yield polyaniline (PANI) nanocrystals and polypyrrole (PPY) nanocrystals, other important conductive polymers, in addition

to PEDOT nanocrystals. This liquid/liquid interfacial method yielded uniform and needle-shaped conductive polymers of PANI and PPY after 48 hours and these conducting polymers had the single crystalline structure with the fast conductivity switching behavior within milliseconds. This technique will provide a general route to synthesize conducting polymers via oxidative coupling processes in a single crystal state, which is extremely difficult to achieve by other synthetic methods.

4.3.1 Experimental

4.3.1.1 Materials and Apparatus

Pyrrole, aniline, ferric chloride, dichloromethane, and dialysis tubing were purchased from Aldrich Chemical Co.. Transmission electron microscopic (TEM) and High resolution transmission electron microscopic (HRTEM) studies were conducted on JEOL 1200 EX and Tecnai G2 F20 cryoelectron microscopes respectively; STM/STS studies followed the processes described in our previous contribution on both PicoSPM II (Agilent) and Nanoscope IIIa MultiMode (Veeco)[85] microscopes for study and comparison.

4.3.1.2 Synthesis of Needle-Shaped PANI and PPY

In a typical synthesis, aniline or pyrrole monomers were dissolved in dichloromethane (DCM, 5mL, 1mg/mL) to form the bottom organic layer and the oxidant, ferric chloride ($FeCl_3$), in deionized water (5mL, 0.1mg/mL) to form the upper water layer. After interfacial system was established, the aqueous layer was

collected after 48 hrs. The purification processes of resulting polymer nanocrystals were described in the experimental part of Section 4.2.

4.3.1.3 Ultraviolet-Visible Absorption of PANI and PPY

The purified conducting polymer nanoneedle suspensions were collected for the Ultraviolet-Visible (UV/Vis) absorption study on a Perkin Elmer Lambda 650 UV/VIS spectrometer. Equation 4.1 is employed for the energy conversion from the wavelength (nm) to the band gap (ev).

$$\text{Band gap (ev)} = 1243/\text{wavelength (nm)} \qquad (4.1)$$

4.3.2 Results and Discussion

Our aqueous/organic interfacial system was composed of water and DCM. The monomers of PANI and PPY were in the organic solvent while an oxidant, ferric chloride, was in the water phase. The oxidative coupling polymerization of monomer was mediated at the aqueous/organic interface (Scheme 4.2). Comparing to the experimental condition to synthesize PANI fibers at the interface,[129] our coupling polymerization was controlled to be much slower by reducing the concentration of the oxidant to 0.1 mg/mL in order to obtain their single crystals. The TEM image (Figure 4.9 A) shows the nanoneedles of PANI with an average length and diameter of 63 nm and 12 nm. The average length and diameter of PPY are 70 nm and 20 nm as shown in Figure 4.10 A. Single crystalline conducting polymers were first nucleated at the interface through oxidative coupling between PANI or PPY monomer from the organic layer and ferric chloride from the aqueous layer. These polymer nanocrystals were grown to the aqueous layer in the oriented direction and then they we dispersed

into the aqueous layer in the nanoneedle form. The high resolution TEM re images of both PANI and PPY resolved their lattice fringes as shown in Figures 4.9B and 4.10 B. The HRTEM images (figures 4.9B and 4.10B) and Electron diffiraction images(Figures 4.14 and 4.15, Table 4.4) of PANI and PPY confirmed the single crystalline nature of the monodisperse nanoneedles.

We hypothesize that those single crystalline conducting polymers are grown by "*interfacial polymerization-crystallization*" mechanism (Scheme 4.2). Previously it was reported that when polymerization of PANI occurs in two-phase matrix, these polymers grow in the non-crystalline fiber form at the interface and the polymerization terminates as polymers dispersed into aqueous phase due to hydrophilic nature of the polymer.[130] When the monomer and the oxidant concentrations higher than those described in our experimental section were applied to polymerize PANI and PPY, the formation of amorphous nanofibers or granular particles were observed with fast growth kinetics, thus consistent with our hypothesis. To grow polymers in single crystalline structure at the interface, the interfacial reaction needs to be slow down significantly. We could achieve this condition by employing the low concentrations of the PANI/PPY monomer and the $FeCl_3$ oxidant. After attacked by the oxidant, the monomers around the interfacial region are charged positively by losing electrons to Fe^{3+} ions. And then the counter ions, Cl^-, bind these positive charges and bridge the repeated units as shown in the right illustration of Scheme 4.2. Due to the hydrophilic nature of these primary species, the polymerization proceeds along the normal of the interface followed by further coupling reactions. In our method, those oriented polymers could be aligned between

positively charged repeated units and negatively charged Cl ions during the slow interfacial reaction (Scheme 4.2) to form elongated rice-like crystals as shown in Figures 4.9A and 4.10A. The polymerization with the disordered monomer alignment is also suppressed when freshly formed nanoneedles diffuse away from the reactive interface.[130] Since fewer monomers are attacked by radical cations, the oxidative coupling reaction could be terminated in relatively short time scale, which also favors the formation of the shorter rice-shaped crystals rather than long fibers. The binding between the repeated units and Cl^- ions was confirmed by the energy dispersive spectroscopy (EDS) (Figure 4.11). The ratio between the counter ion (Cl^-) and the monomer unit of PANI is 1:12 while the ratio for PPY is 1:20. The difference of the ion-monomer ratio between PANI and PPY reflects the difference in their ability to accommodate positive charges, in consistence with the lower ionization potential of PANI. The EDS results of PANI and PPY show that there was no iron traces in the spectrum. Furtheremore, the EDS results of PANI and PPY proved that the electron diffraction was originated from single crystalline conducting polymers.

These nanoneedles displayed interesting electronic properties due to their unique morphological and crystalline structure. We applied scanning tunneling spectroscopy (STS) to probe their electronic properties. In our STS studies for PANI and PPY nanoneedles, each suspension was collected from upper aqueous layer and dialyzed for 10 hours in *nano-water* (resistivity 18.2 MΩ cm, total organic carbon level 10 ppb) to remove impurities. The purified suspension was then 10-fold diluted with *nano-water* and spin-coated on a gold-111 substrate surface. The tunneling I-V curves were recorded from -5 to 5 V scale for these polymers between the STM tip and Au

substrate. While bare Au substrate showed a typical metallic tunneling I-V behavior, the abrupt switching behaviors were observed for PANI at ±3.5 V and PPY at ±4 V as shown in Figure 4.12. The PANI nanoneedles were insulated in the range of -3.5V ~ +3.5V, and in the case of PPY nanoneedles the "OFF" state is between -4.0 V and +4.0 V for PPY. Beyond these critical points, both PANI and PPY nanoneedles turned on the conducting state, and this switching process from the "OFF" to the "ON" states was in millisecond scale. This result indicates that the barrier for electron injection is high in the range of "OFF" region to prevent the passage of tunneling electrons. Previously, the rapid transition from the "OFF" to the "ON" states with the sharp raising slope in the I-V curves was only observed in PANI in molecular scale, grown electrochemically between electrodes in the length of 1 nm.[101] Therefore, this is the first example to observe the fast conductance switching behavior in large conducting polymer crystalline domains.

Since the voltage range of "OFF" state is larger in PPY than PANI in Figure 4.12, this comparison indicates that the band gap for PPY nanoneedles is larger than the band gap for PANI nanoneedles. This is consistent with Ultraviolet-Visible (UV) absorption spectra of PANI and PPY, as shown in Figure 4.13. From those spectra, the PPY nanoneedle has the higher band gap (2.5eV) as compared to the PANI nanoneedles (2.21eV). It should be noted that we did not observe characteristic NIR peaks in Figure 4.13 because our polymer systems do not contain high level doping, typically observed in the conductive polymer samples synthesized in the classical one phase methods.[131]

Scheme 4.2 Slow interfacial polymerization-crystallization through oil/water interface.

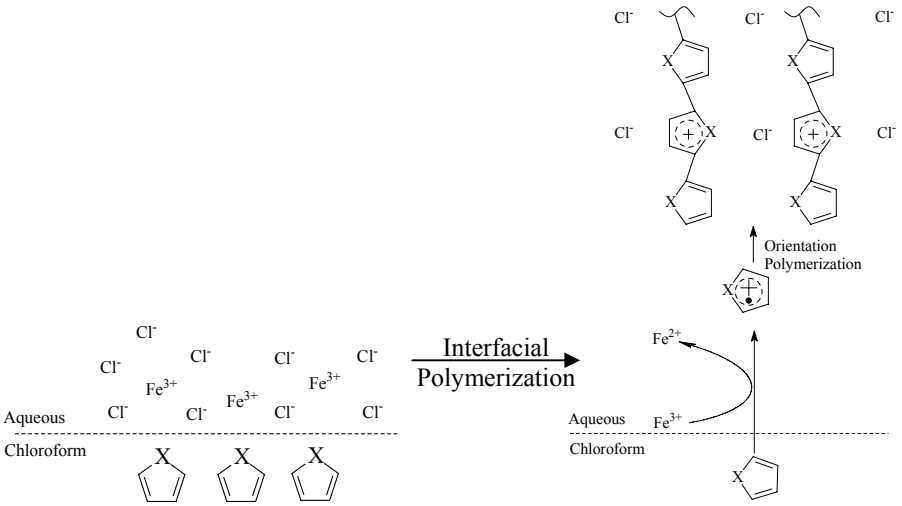

Figure 4.9 (a) TEM image of PANI nanoneedles; **(b)** HRTEM image of PANI. (by Nurxat)

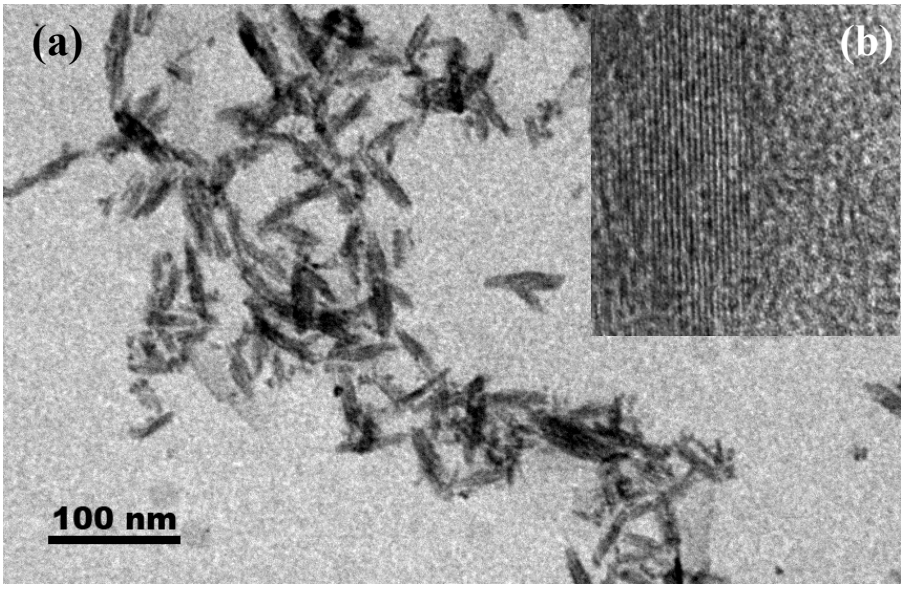

Figure 4.10 (a) TEM image of PPY nanoneedles; **(b)** HRTEM image of PPY. (by Kai & Nurxat)

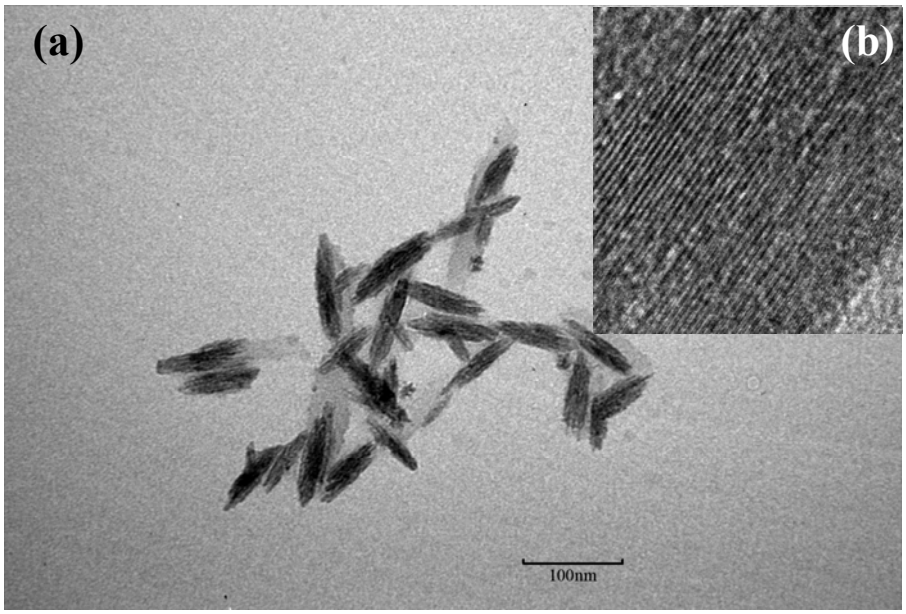

Figure 4.11 EDS spectra of polymer nanoneedles: **(a)** PANI; **(b)** PPY. (by Kai & Nurxat)

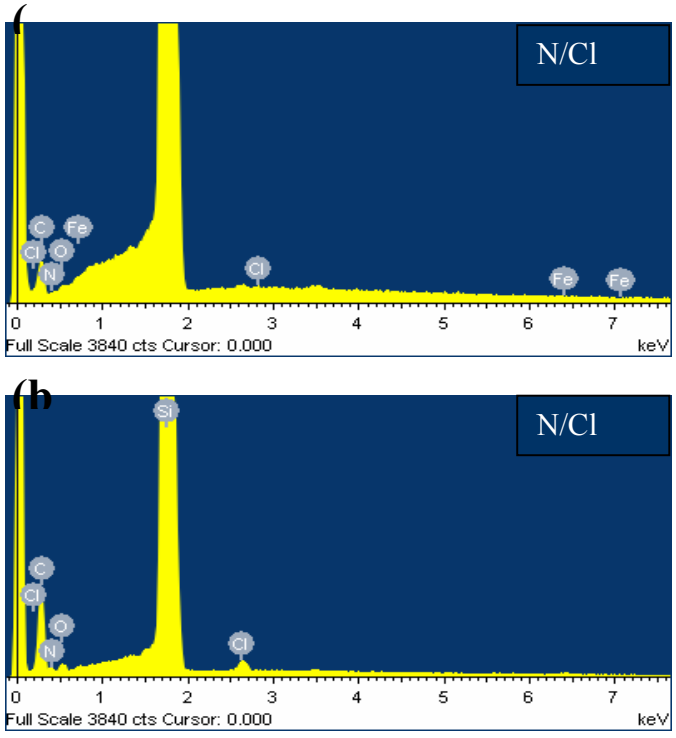

. **Figure 4.12** STS spectroscopy of conducting polymer nanoneedles and the gold-111 substrate surface. (by Kai & Nurxat)

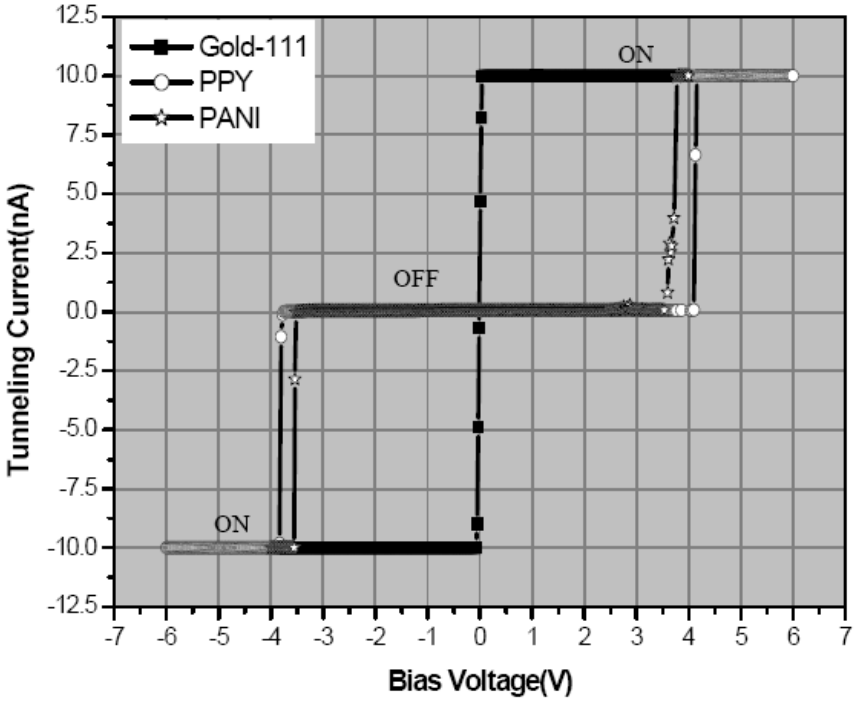

Figure 4.13 UV spectra of conducting polymer nanoneedles. Calculated bandgaps are 2.21 (PANI) and 2.50 (PPY) eV. (by Kai & Nurxat)

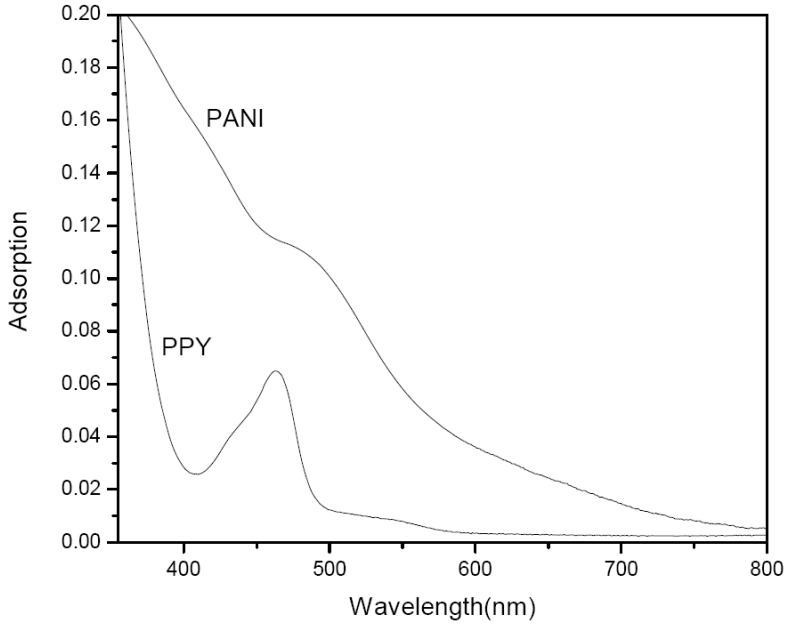

4.3.3 Conclusion

Single crystalline nanoneedles of PANI and PPY were synthesized using an interfacial polymerization process for the first time. An "*interfacial polymerization-crystallization*" at the liquid/liquid interface allowed PANI and PPY polymers to form single crystalline nanocrystals in the rice-like shape in the dimensions of 63 nm x 12 nm for PANI and 70nm x 20nm for PPY. The conductance switching properties of these crystalline polymers were observed in their I-V curves, and the conductance switching was fast in the time scale of milliseconds. Since this liquid/liquid interfacial synthesis method yielded conducting polymers of EDOT, PANI, and PPY in the single crystal state, our technique could be applied as the general fabrication process of single crystalline conducting polymers.

Figure 4.14 The electron diffraction image of Polyaniline nanoneedles.
(by Nurxat & Kai)

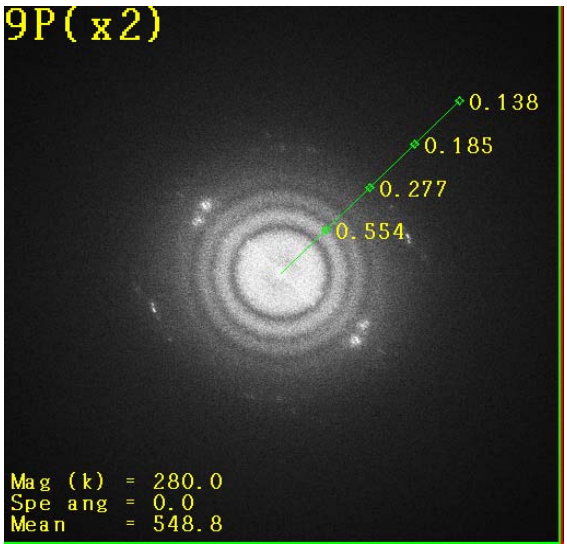

Figure 4.15 The electron diffraction image of Polypyrrole.(by Nurxat & Kai)

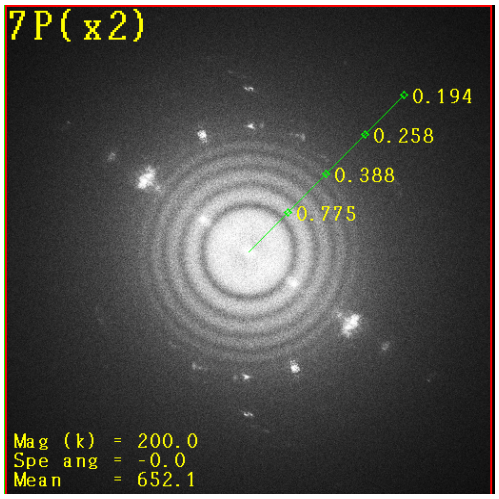

Table 4.4 Lattice assignments based on the diffraction pattern. The polymers assigned as an orthorhombic lattice.

d(nm) PEDOT	d(nm) PANI	d(nm) PPY	indices
0.796		0.792	001
0.584	0.734	0.792	100
0.494	0.544		010
0.427	-		-
0.398	-	0.387	002
0.344	-		-
0.292	0.369	0.387	200
0.265	-	0.264	003
0.231	0.277	0.331	020
	0.246	0.264	300
		0.246	-
		0.238	-
		0.194	004

Chapter 5

Simple separation of Size-selected Peptide Nanotubes Using Size-exclusion Columns and use as Templates for fabricating one-dimensional single chains of Au nanoparticles[174]

5.1 Introduction

Recently, 1D single chain of metal nanoparticles (SCMNPs, i.e. nanocrystal necklaces) have been attracting great attention due to their unique electron transport properties via their coulomb blockade and quantum confinement effect.[179-184] The transport properties are sensitive to the size and the gap between them, and the necklaces have potential applications as single electron transistors or conductivity-tunable nanowires for microelectronics.[27, 148, 149, 185-192] The ability of SCMNP's also attractive for application as plasmon waveguides.[193-196] While electron beam etch lithography have been reported extensively to prepare SCMNPs,[191-196] more scalable and economical methods to synthesize SCMNPs are desirable for industrial applications. In general, wet chemical methods are more straightforward to synthesize 2D or 3D patterns of nanoparticles, but controlling the NPs to align along a straight 1D direction is more difficult without any templates. Various nanoparticles were grown on various wire-like templates as single chains such as surfactants, DNAs, and polymers;[197-201] however those chains tend to aggregate and more straight SCMNPs are necessary to incorporate them as building blocks to the device configurations. The quality of nanoparticles on the templates is also desired to improve so that nanoparticles are more monodisperse and the distance between nanoparticles is more

uniform to control the transport property of electron more precisely via quantum confinement effect for applications in microelectronics and optics.

Previously, peptide nanotubes in the diameter of >100 nm, self-assembled from peptide bolaamphiphile monomers via 3D intermolecular hydrogen bonds between amide and carboxylic acid groups,[202] were coated by a synthetic peptide, A-H-H-A-H-H-A-A-D (HRE), on the nanotube surfaces and these HRE peptides mineralized Au ions to grow monodisperse Au nanoparticles in the diameter of 6 nm on the nanotubes.[150] The HRE peptide, whose sequence is known to mineralize Au ions efficiently,[139] was bound to free amide groups of the nanotubes via hydrogen bonding and regulated the size, the monodipsersity, and the packing density (i.e., the distance) of Au nanoparticles on the nanotubes.[148] Recently, peptide nanotubes from peptide bolaamphiphile monomers were found to grow in the range of 10 – 300 nm in diameter at room temperature and these nanotubes do not aggregated in aqueous solution. Therefore, if we can separate the HRE peptide-coated peptide nanotube whose diameter is comparable to the size of metal nanoparticles, it may be possible to grow Au nanoparticles as straight 1D single chains in the controlled size and the controlled particle-to-particle distance along the straight peptide nanotubes that act as templates. Here we report the simple method to separate peptide nanotubes by using size-exclusion columns and grow Au nanoparticles in the diameter of 6 nm as a straight 1D single chain on the HRE peptide-coated nanotube in the diameter of 10 nm (scheme 5.1). Our method for the SCMNP fabrication grows highly-monodispersive nanoparticles directly on wire-like templates via biomineralization instead of attaching pre-formed nanoparticles on the templates.

5.2 Experimental

5.2.1 Peptide Bolamphiphile monomer synthesis

The synthesis of peptide bolaamphiphile was followed by the published method.[29] To asolution of glutaric acid (0.5g) and 1-hydroxylbenzotriazole (0.65g) in dimethylformamide (DMF) was added 1-ethyl-3-(3 dimethylaminopropyl)-carbodiimide hydochloride (0.92g) dissolved in chloroform (10ml) with stirring at -5°C. After 1hour, a solution of glycin-glycin benzyl ester hydrochlorate (1.88g) in methanol (10ml) and triethylamine (0.67ml) was added to the reaction mixture. It was stirred for 24 h at 0°C and allowed to slowly warm to room temperature. Evaporation of the solvent resulted a white powder, which was washed with 1% citric acid (50ml), water (50ml), and 4% sodium hydrogencarbonate (50ml). To a solution of powder (0.82g) in DMF (200ml) was added 0.1N NaOH (35ml) at 80°C-85°C, and stirred for 4h. The solution was acidified with 1N HCl (4ml). The solvent was evaporated under reduced pressure leave a white solid product. The product was washed with cold acetone and water to give a white powder of bis(*N*-□-amido-glycylglycine)-1,3-propane dicarboxylate (0.53g, 55%). All chemicals were purchased from Sigma. 1H NMR spectra were recorded with the 500 DRX BUKER by using DMSO-d6 as an internal standard for the organic solutions. 1HNMR (DMSO-d6, 500MHz): δ1.72 (quintet, 2H, CH2(C*H*2)CH2); (t, 4H, C*H*2(CH2)C*H*2); 2.1 (t, *J*=7.3 Hz, 4H, COC*H*2(CH2)C*H*2CO); 3.76 (d ×2, *J*=5.9 Hz, 8H, NHC*H*2CO2); 8.17 (t ×2, *J*= 5.8 Hz, 4H, N*H*); 12.1 (s, *J*=5.9 COOH ×2). ^{13}C NMR δ 22.245, 39.92, 40.01, 42.722, 170.6, 172.17, 173.25; FABHRMS Calcd for $C_{13}H_{20}O_8N_4$ (M+H+) : 361.13.

5.2.2 Experimental conditions for peptide nanotube assembly

The peptide bolaamphiphile monomer (0.018g) was dissolved in a 10 ml NaOH solution (0.1N). After sonicating it for 1 minute with a ultra-sonicator (Fisher Scientific FS20H), the resulting solution was filtered by a syringe equipped a 400 nm Millex-HV membrane. The 5 ml citric acid (50mM) was added to the solution to adjust the pH value to 4.7. After the solution was kept at 5~6 C° for 20 days, the peptide nanotubes were produced in the solution. All nanotubes were centrifuged by an Eppendorf mini centrifuge and washed by distilled water for three times. These nanotubes were dissolved in 2 ml distilled water in an eppendorf tube.

5.2.3 Preparation of the size-exclusion column and experimental conditions for the nanotube separation process

First, glass wool (100mg, Fisher) was inserted in the bottom of 9″ glass pipet (Fisher), and then 250mg Sephadex G-50 medium beads were placed in the glass pipet on the glass wool. After the column was dipped in deionized water for 72 hrs, 1 mL of the peptide nanotube solution was run through the column and rinsed with 23 ml deionized water. The fluent rate of rinsing water was 0.5ml/mins. Every 1ml fraction of the sample was collected at sequential time. The nanotubes were centrifuged to be collected and dissolved in tris-buffer (pH 8.6, 0.1M).

5.2.4 The growth of Single Chain of Metal Nanoparticles on the peptide nanotubes

After the column separation, the peptide nanotubes with diameter of 10nm were centrifuged to be collected, and then dissolved in 200μl of tris-buffer (0.1M, pH 8.6). The HRE peptide (1mM, 10 μl) was incubated in the nanotube solution for 24 hours

at room temperature. Then 3 mg of the chloro(trimethylphosphino)gold was introduced into the system and stored for 72 hrs to adsorb Au ions onto the nanotubes. In order to separate free Au ions in the solution, the nanotube solution was centrifuged under 14,000rpm for 30 minutes in the Eppendorf mini centrifuge. The nanotubes on the bottom of the eppendorf tube were dissolved in 200 μl tris-buffer (pH 8.6, 0.1M). A reducing agent, hydrazine hydrate (16 M, 6 μl) was added to the system to reduce Au ions on the nanotubes for 3 days, and the Au nanoparticle coating was confirmed by the color change of solution to purple.

5.3 Results and Discussion

Peptide nanotubes were self-assembled from peptide bolaamphiphile monomers, bis(*N*-α-amido-glycylglycine)-1,3-propane dicarboxylate, in a pH 4.7 NaOH/citric acid solution (50 mM).[202] After the solution was kept at 5 – 6 ˚C for 20 days, the peptide nanotubes were observed in the diameter of 10 – 320 nm. Then a size exclusion column with Sephadex G-50 beads was used to separate peptide nanotubes in diameter. The 9″ glass pipet was first filled with glass wool at the bottom, and then 250 mg of the Sephadex G-50 medium beads were loaded in the column in the height of 4″. For the size separation of peptide nanotubes, 1 mL of the nanotube solution was run through the resulting column and rinsed with 23 mL deionized water. The fractions of nanotube samples from the column were studied by transmission electron microscopy (TEM) in an accelerating voltage of 120kV. The specimens were prepared by depositing one droplet of the nanotube solution on carbon film-coated copper grids and drying in the air. The first fraction, 6 mL of the sample from the column, contained the peptide nanotubes in the diameter of 320 nm. The second

fraction, another 6 mL of the sample, included the peptide nanotubes in the diameter of 180 nm. The third and fourth fraction contained 120 nm and 10 nm peptide nanotube, respectively. This outcome is summarized in Figure 5.1a, and typical TEM image of the separated peptide nanotube is shown in Figure 5.1b. In the inset of Figure 5.1b, the hollow structure of peptide nanotube was clearly observed. We also examined every 1 mL fraction from the column, and only four diameters, 10, 120, 180, and 320 nm of peptide nanotubes were observed by TEM. The separated peptide nanotubes in the diameter of 10 nm were used to fabricate the SCMNPs.

Scheme 5.1 Procedure for the fabrication of Au nanoparticle chains on peptide tubes.

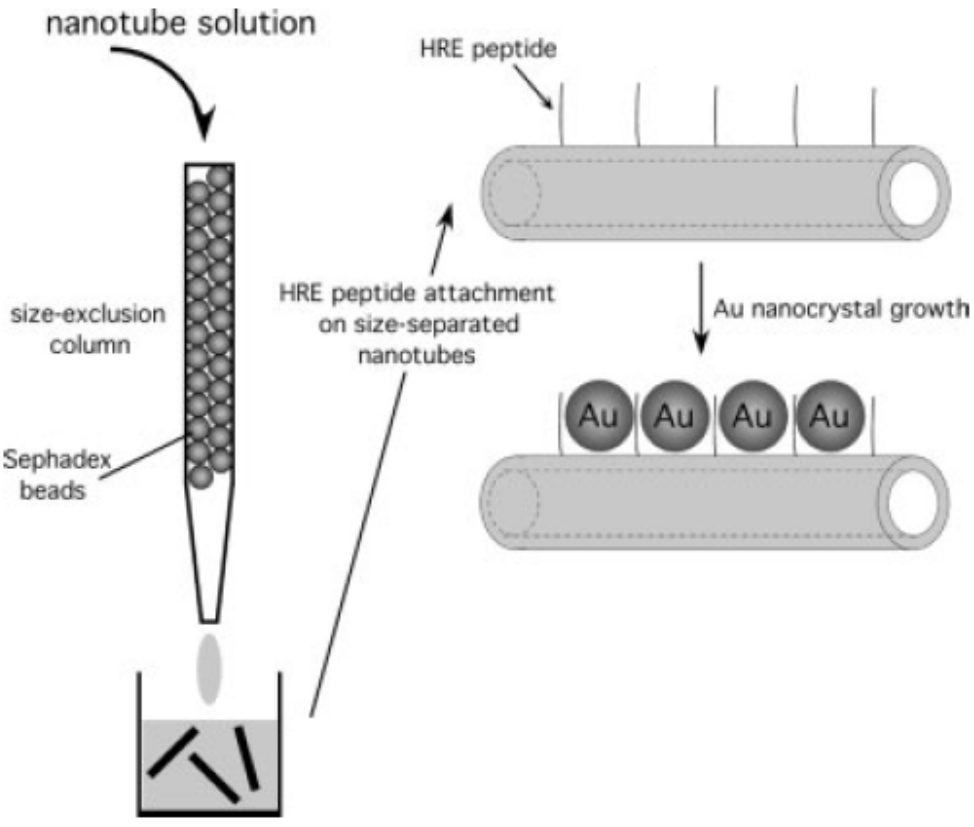

Figure 5.1. (a) Diameters of peptide nanotubes separated by a size exclusive column. Each fraction was in the volume of 6 mL and whole nanotube solution was 24 mL. (b) TEM image of peptide nanotube in the diameter of 10 nm (fraction 4). Scale bar = 50 nm. Inset: The magnified TEM image of peptide nanotube in the diameter of 10 nm. Scale bar= 30 nm. (Gao & Nurxat)

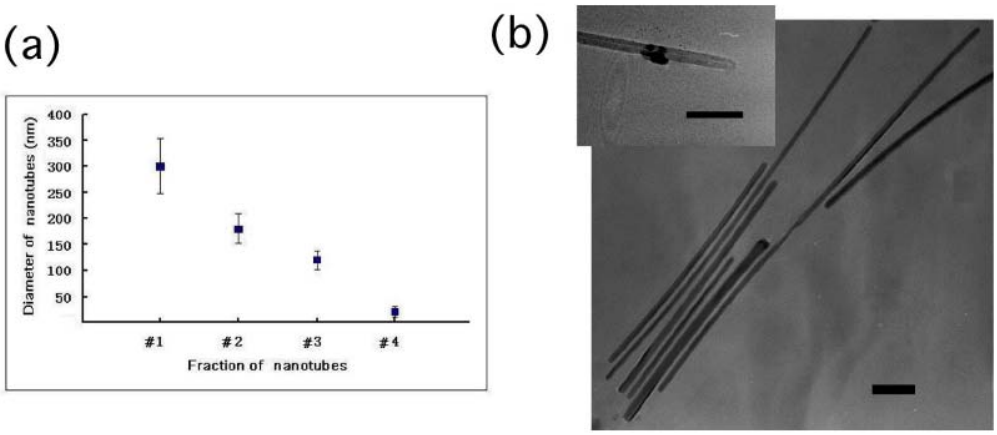

To grow Au nanoparticles on the template nanotubes, the HRE peptides, purchased from GeneScript Corporation, were incubated in the nanotube solution for 24 hours at room temperature.The coating of HRE peptide on the peptide nanotube was confirmed by Raman microscopy.[150] Then the chloro(trimethylphosphino)gold was mixed in the peptide nanotube solution. After 72 hrs, those Au ions on the nanotubes were reduced by hydrazine hydrate (16 M) for 3 days. The growth of SCMNPs on the nanotubes was confirmed by color change of the solution to purple. The detailed information about peptide bolaamphiphile monomer synthesis, the experimental condition of peptide nanotube assembly, preparation of the size exclusion column, the nanotube-separation process, and the growth condition of SCMNPs on the peptide nanotubes were shown in the experimental section. Figure 5.2 a shows TEM image of SCMNPs grown on the peptide nanotubes in the diameter

of 10 nm. In the magnified TEM image of SCMNPs in Figure 5.2 b, monodispersive Au nanoparticles in the diameter of 6 nm were aligned as a 1D single chain on the nanotube surfaces. The size of Au nanoparticles on the 10 nm-peptide nanotube was consistent with Au nanoparticles grown on larger peptide nanotubes in the diameter of 200 nm.[148, 150] In the fraction 4 of peptide nanotubes, long peptide nanotubes in the length of > 1 μm were also observed in the small population of the sample. After the coating process of Au nanoparticles, those long nanotubes were also coated by Au nanoparticles to form long SCMNPs, as shown in Figure 5.2 c. Electron diffraction of the SCMNPs in Figure 5.2 a shows that (111), (200), (220), (311), and (331) faces of cubic Au crystal (Figure 5.2 d). It should be noted that polydisperse Au nanoparticles were grown on the nanotubes in much lower coverage without the single chain alignment when the Au ions were reduced on the nanotubes without the HRE peptide coating.

Figure 5.2. (a) 1D single chain of Au nanoparticles grown on peptide nanotubes in the diameter of 10 nm. Scale bar = 100 nm. (b) The magnified TEM image of single peptide nanotube coated by SCMNPs. Scale bar = 50 nm. (c) 1D single chain of Au nanoparticles grown on long peptide nanotubes Scale bar = 200 nm. (d) Electron diffraction of (a). (by Gao & Nurxat)

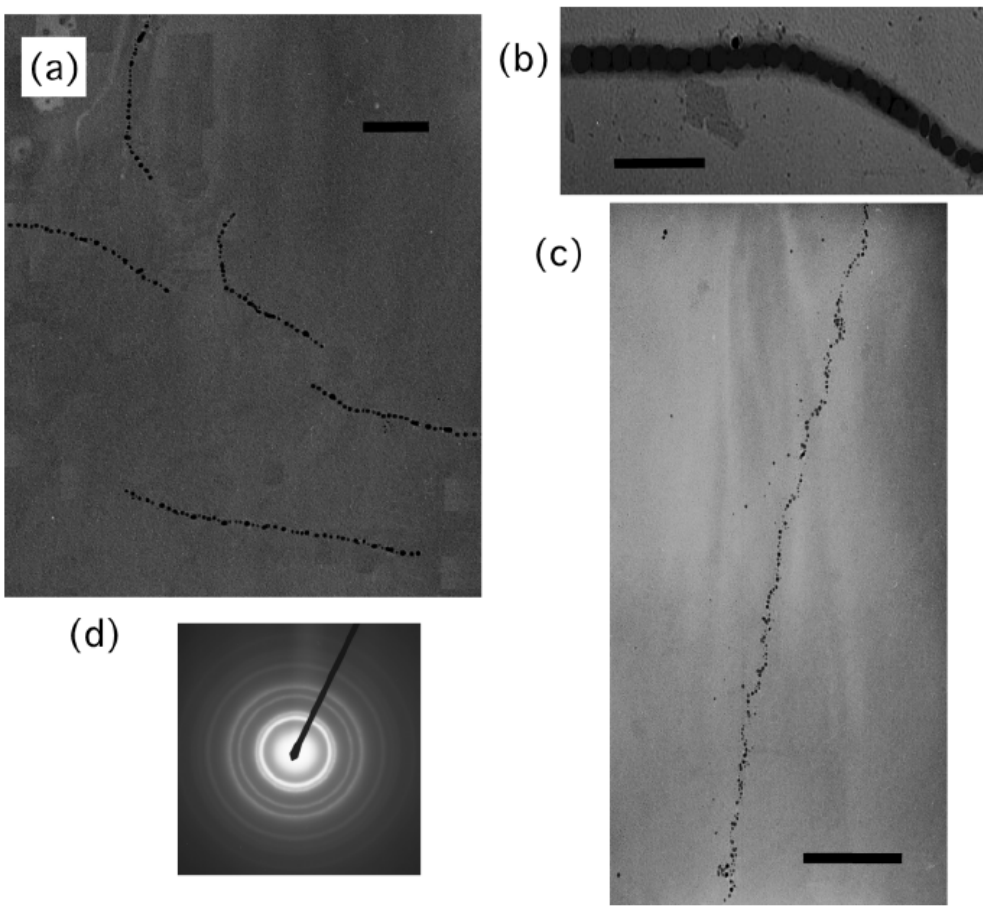

5.4 Conclusion

In conclusion, the straight 1D single chain of Au nanoparticles, whose diameter was 6 nm, was synthesized on the template peptide nanotubes in the diameter of 10 nm. The HRE peptides on the nanotubes regulated the size, the monodispersity, the particle-

toparticle distance and the high crystallinity of Au nanoparticles. The length of 1D single chain of Au nanoparticles could be extended in the order of a few μm on the long nanotube, which may be very useful for practical applications in single electron transistors, plasmon waveguides, and liquid-crystal displays (LCDs).

PART II Biomimetic Assembly of Nanomaterials

Chapter 6

Biological Bottom-Up Assembly of Antibody Nano-tubes on Patterned Antigen Arrays[132]

6.1 Introduction

The bottom-up approach in nanofabrication has been studied extensively due to the potential to develop devices such as electronics, actuators, and sensors more efficiently and economically compared to existing technologies.[133-135] Application of biotechnology in nanofabrication also has an advantage to produce functional building-block materials that may not have synthetic counterparts in much milder experimental conditions, such as room temperature and ambient pressure.[136] Various building blocks have been developed for the biological bottom-up approach;[17, 18, 137-142] however, it is necessary for these building blocks to be addressed to the exact locations with high precision and reproducibility to function in the nanometer-scale devices.[133, 143, 144] Recently, carbon nanotubes were assembled on regions coated with the polar chemical groups on large scale.[145]

Here we introduced a new type of building block, antibody nanotubes, and demonstrated anchoring them on complementary antigen arrays via antibody-antigen recognition. Biological recognition between the antibody nanotubes and the antigen arrays permitted recognition-driven assembly of ordered nanotube arrays. The array

of antigens was written by using the tip of an atomic force microscope (AFM) on alkylthiol self-assembled monolayer (SAM)-coated Au substrates via nanografting.[146] After antigens were immobilized onto the shaved regions of the alkylthiol SAMs with the AFM tip, antibody nanotubes, produced by incubating antibodies in template nanotube solutions, were selectively attached onto the antigen regions (Scheme 6.1).

Scheme 6.1. Schematic diagram of the antibody nanotube assembly on the complementary antigen substrates via biological recognition. (a) Self-assembly of alkylthiol monolayers on Au substrates. (b) Shaving trenches on the alkylthiol SAM by using the AFM tip (nanoshaving). (c) Deposition of antigens in the shaved trenches (nanografting). (d) Location-specific immobilization of the antibody nanotube onto the complementary antigen regions via the biological recognition.

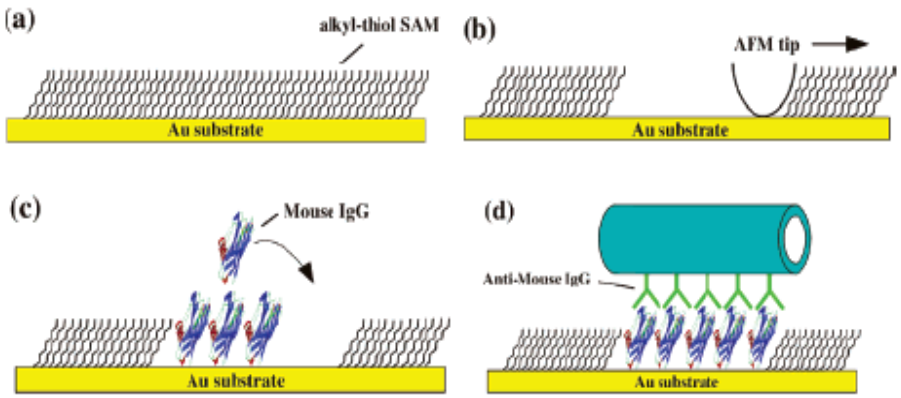

6.2 Experimental

A template nanotube self-assembled from bolaamphiphile peptide monomers in NaOH/citric acid solution via three-dimensional intermolecular hydrogen bonds[28, 29] has been demonstrated to im-mobilize various proteins and peptides on nanotube surfaces.[27, 147-149] This template nanotube immobilizes proteins and peptides at free amide sites on the nanotube sidewall via hydrogen bonding by means of simple

incubations, the detailed procedures of which were published previously.[148, 150] After those nanotubes were centrifuged and run through size-separation columns, a 1-mL solution of the resulting nanotubes (10 mM) with an average diameter of 100 nm were incubated with a 1-mL solution of goat anti-mouse IgG in a pH 7.2 phosphate buffer (50 μg/mL). After 48 h, the anti-mouse IgG was coated on the template nanotubes to form the antibody nanotubes. The anti-mouse IgG nanotubes were washed with Nanopure water and centrifuged twice to remove unbound anti-mouse IgG before mixing with the antigen-coated substrates.

6.3 Results and Discussion

The attachment of anti-mouse IgG on the nanotube was confirmed by fluorescence microscopy. The 1 mL solution of the template nanotubes (10 mM) were incubated with a 1mL solution of the Alexa Fluor 546–labeled goat anti-mouse IgG in a pH 7.2 phosphate buffer (50 μg/mL). After 48 hrs, the anti-mouse IgG was coated on the template nanotubes to form the antibody nanotubes in the fluorescence micrograph, as shown below (Figure 6.1). It should be noted that this nanotube sample was not centrifuged and run through size-separation columns because the nanotubes were necessary to be in the form of the bundle to be clearly observable by fluorescence microscopy.

Figure 6.1 Fluorescence micrograph of the Alexa Fluor 546–labeled anti-mouse IgG-coated nanotube. (by Ipsita, Rob, and Nurxat))

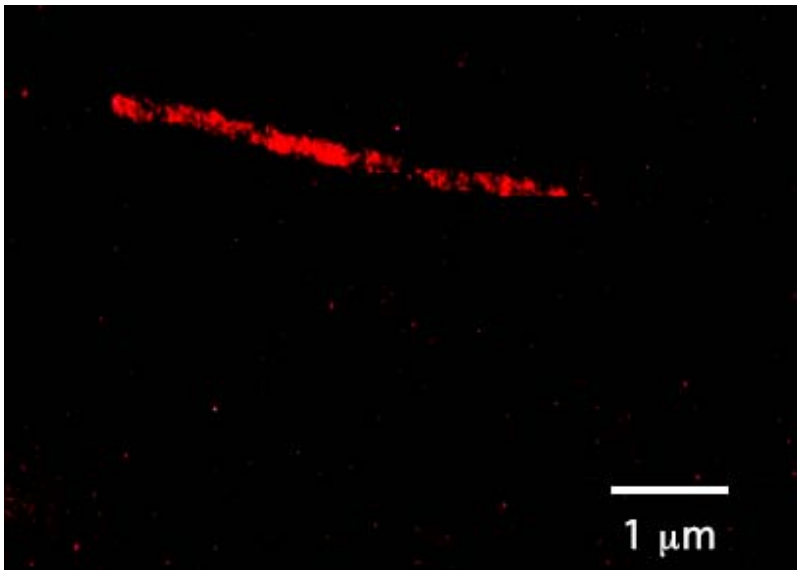

The FITC-labeled anti-mouse IgG on the nanotube was confirmed to recognize and bind the mouse IgG in solution. The anti-mouse IgG nanotubes were incubated with a 1 mL solution of the FITC–labeled mouse IgG in a pH 7.2 phosphate buffer (50 μg/mL). After 5 hrs, the FITC-labeled mouse IgG was coated on the anti-mouse IgG nanotubes in the fluorescence micrograph, as shown below(Figure 6.2). This result indicates that the anti-mouse IgG on the nanotube does not lose the recognition function and binds the mouse IgG.

Figure 6.2 Fluorescence micrograph of the anti-mouse IgG nanotube coated with the FITC-labeled mouse IgG. (by Rob, Ipsita, & Nurxat)

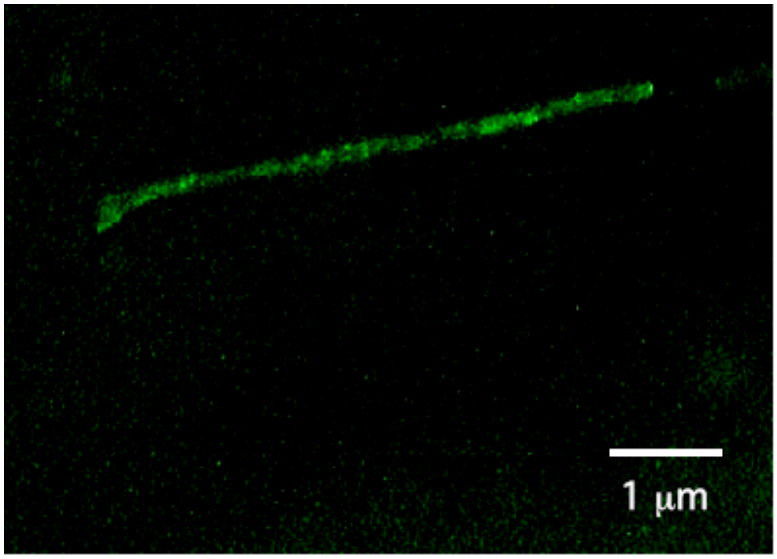

To observe the selective immobilization of antibody nanotubes on the mouse-IgG arrays, systematic AFM analyses for the resulting substrates were applied (Figure 6.3). After 1-octadecanethiol (0.01 mM) was self-assembled on Au substrates in 99% ethanol at room temperature for 24 h (Figure 6.3 a), a series of trenches (400 nm _ 4 ím) were made by shaving the alkylthiol SAM with a Si3N4 tip (Veeco Metrology) of the AFM (Nanoscope IIIa and MultiMode microscope, Digital Instruments), as shown in Figure 6.3 b (left). These trenches were patterned by using a customized Nanoscript software (Veeco Metrology). The section analysis of the trenches in Figure 6.3 b (right) shows that the depth of all trenches (marked by black dotted lines) is 10 nm. The substrate was washed sequentially first with ethanol and then with hexane, but the alkylthiol molecules removed by the AFM tip were still partially piled

up and remained at the edges of trenches as shown in Figure 6.3 b (left). After the mouse IgG was incubated with the resulting substrates for 1 h at room temperature, the mouse IgG was deposited on the trenches via the thiol-Au interaction (Figure 6.3 c (left)).[151] The average height of trenches was observed to increase from -10 to +10 nm after incubating the mouse IgG, indicating the deposition of mouse IgG in the trenches (Figure 6.3 c (right)).[152] When the anti-mouse IgGcoated nanotubes were incubated in the buffer solution containing the mouse IgG-patterned substrate for 5 h, the antibody nanotubes were observed to attach to the mouse IgG regions (Figure 6.3 d (left)) after washing the substrates with Nanopure water. The section analysis of this AFM image, Figure 6.3 d (right), also supports the biological recognition-driven nanotube immobilization by increasing the height from +0 to +100 nm, which is consistent with the diameter of template nanotube. Figure 6.3 e, the magnified AFM image of Figure 6.3 d, shows that the multiple antibody nanotubes in the diameter of 100 nm were attached to the mouse IgG regions. The magnified AFM image of the anti-mouse IgG nanotubes in the height mode (inset in Figure 6.3 e) shows that the antibody nanotubes were aligned along the trench while elongated particles were also observed at the upper side of mouse IgG region. At this point, we are still investigating whether those particles are the aggregations of mouse IgG or the nanotube fragments.

Figure 6.3 AFM images of (a) alkylthiol SAMs on Au substrate; (b) the array of trenches shaved by the AFM tip (left), the section analysis of (b) along a blue dotted line in the image (right), scale bar) 2 ím; (c) the array of trenches filled with mouse IgG (left), the section analysis of (c) along a blue dotted line in the image (right), scale bar) 1 ím; (d) anti-mouse IgG-coated nanotubes immobilized on the mouse IgG-deposited regions (left), the section analysis of (d) along a blue dotted line in the image (right), scale bar) 1 ím; (e) anti-mouse IgG-coated nanotubes immobilized on the mouse IgG-deposited regions in a higher magnification (inset: in the height mode), scale bar) 300 nm. The positions of trenches in the section analyses (b), (c), and (d), are shown by black dotted lines. (by Nurxat)

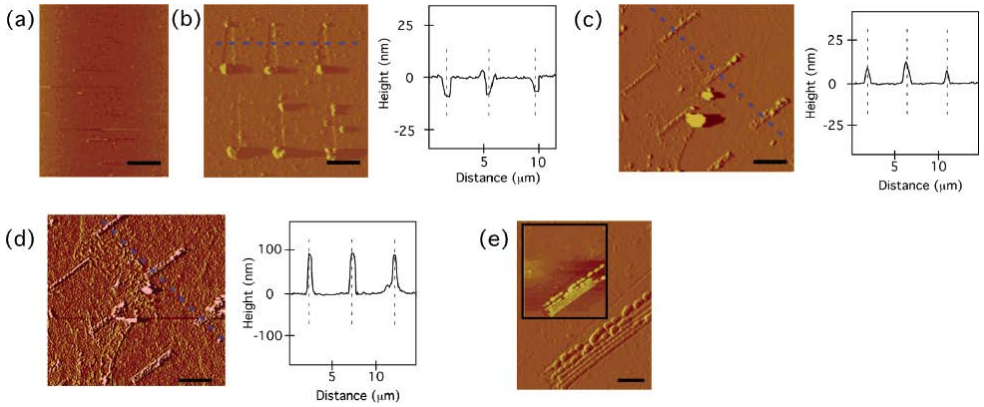

To demonstrate that the assembly of antibody nanotubes is location-specific via biological recognition, the anti-mouse IgGcoated nanotubes were incubated on the substrate patterned with the human IgG instead of the mouse IgG. As shown in Figure 6.4, no anti-mouse IgG-coated nanotubes attached to the human IgG regions patterned on the alkylthiol SAM/Au substrates via nanografting. This control experiment indicates the potential that multiple antibody nanotubes can be addressed onto patterned antigen regions respectively because the biological recognition and complexation of antibody nanotubes with complementary antigen SAMs are very specific, as observed in nature.

Figure 6.4 AFM image of the human IgG-deposited regions after the incubation of anti-mouse IgG-coated nanotubes. Scale bar)2 μm. No anti-mouse IgG nanotubes were observed to attach onto the human IgG regions. Inset: The section analysis along a blue dotted line in the image. The positions of trenches in the section analyses are shown by black dotted lines. (by Nurxat, Ipsita, & Rob)

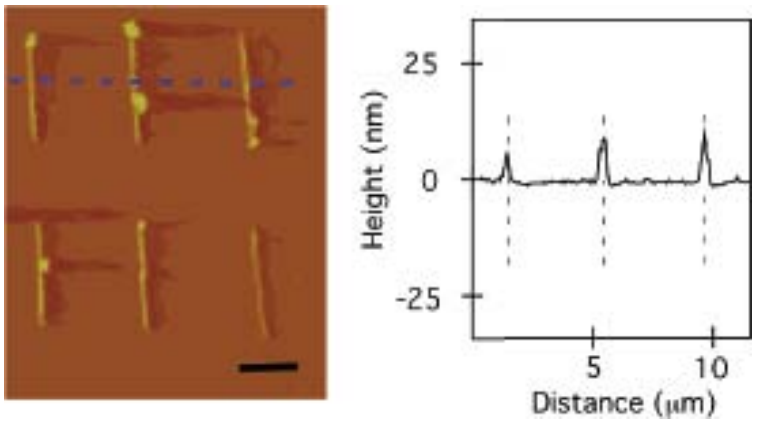

6.4 Conclusion

In summary, we observed that the biological recognition between the antibody nanotubes and the antigen arrays organized the antibody nanotubes as the ordered arrays. This technique is very useful to fabricate advanced nanometer-scale devices with complex functionalities because multiple building blocks with a variety of protein functions can be addressed to specific locations on substrates respectively in a simple process.

Chapter 7

Crossbar Assembly of Antibody-functionalized Peptide nano-tubes via Biomimetic molecular recognition[153]

7.1 Introduction

It is widely accepted that conventional top-down methods such as photolithography is about to hit the limit for further reduction of the patterning scale of electric components. The further miniaturization is necessary to pursue microelectronics with the increased speed and the complexity of device designs. Since various nanotubes and nanowires have been developed to possess superior and distinguished physical properties in last decade, it is natural to seek for new bottom-up technologies to assemble these superior nanoscale building blocks into the device configuration. However, addressing nanowires at precise locations for the interconnection between electrodes is a serious obstacle to overcome in the bottom-up fabrication. Recently, various nanowires and nanotubes have been assembled on substrates by electric fields, microfluidics, drying effect controlled by surface topology, direct mechanical transfer, and assembly on blown bubble films.[154-163] These techniques demonstrated that a large scale assembly of nanowires in a parallel array configuration is possible, and one type of nanowire could interconnect two electrodes in the high wire density.

However, to assemble nanowires into practical logic gate configurations in integrated circuits, we need more than the parallel assembly of nanowires. For example, when the assembling nanowires are monopolar semiconductors, logic gates such as AND, OR, and NOR are necessary to be assembled from two types of semiconducting

nanowires, *n*-type and *p*-type, and some of these nanowires must cross perpendicularly to form a crossbar geometry for the logical operation.[158] In general, this non-parallel assembly of nanowires is extremely difficult and there were only a few examples to demonstrate the crossbar assembly in the bottom-up approach. For example, the crossbar assembly of nanowires could be achieved by microfluidics in two step; after the first array of nanowires was aligned in one direction, the second array of nanowires was assembled perpendicularly by changing the flowing direction.[164] Some of nanowires can be crossed by the two-step fluidic method with no control of the crossing point of the nanowires, however it cannot fabricate more complex geometry necessary for realistic logic gates. For example, how can we align three nanowires parallel in vertical direction and let one nanowire intercept these three nanowires at the middle point in horizontal direction when the type of these vertical nanowires is different from the type of the horizontal nanowire? One of smart ways to achieve this complex crossbar assembly is to let nanowires recognize binding locations and directions and assemble them in a programmed manner in one step. By this way, right nanowire elements can attach and interconnect desired electrodes to fabricate complex electric circuits.

Previously carbon nanotubes were aligned in a parallel array using a simple molecular interaction, hydrophobic interaction in the single step. This recognition-driven assembly method immobilized carbon nanotubes parallel in a large scale, however this method may not be suitable to assemble multiple types of nanotubes simultaneously in different directions due to the lack of complex recognition function. Therefore, we need to apply molecular recognitions with more specificity to assemble

nanowires in complex geometries. Recently, DNAs were applied to the building blocks with their recognition functions[165, 166] and they successfully interconnected two electrodes.[167] In theory, the base-pairing of DNA oligonucleotides can be used as a driving force to locate DNAs as nanowires at well-defined positions,[168] however the cross-bar alignment of DNAs has not been reported, which may be due to the cross-reactivity, the rigidity, and the straightness of DNAs. On the other hand, in nature smart recognition functions of proteins routinely address the biological nanomaterials to exact locations in cells with the high specificity,[169, 170] and therefore antibody is a better candidate to fulfill this task. Recently, we applied the antibody-antigen recognition function to assembly antibody-functionalized peptide nanotubes at targeted locations on substrates in parallel arrays where their complementary proteins were patterned.[132] In our system, very rigid and straight peptide nanotubes were self-assembled from peptide monomers via three-dimensional hydrogen bonds, and antibodies binding at amides on the surfaces of nanotubes[147, 171] could anchor them onto the antigen-patterned areas for their targeted placement on substrates. This fabrication method could also be applied to assemble two types of antibody nanotubes in different rows of parallel arrays respectively where the corresponding antigens were patterned, due to their highly-specific molecular recognition. [172]

While multiple nanotubes could be placed in different positions by the antibody-antigen recognitions in parallel arrays by this biomimetic assembly method, the crossbar assembly of peptide nanotubes has not been accomplished yet. In this report, we applied the antibody-antigen recognition to assemble two types of peptide nanotubes in the cross-bar geometry. Assembling one type of antibody nanotube in

horizontal and the other in vertical directions is very difficult to achieve in one step, however their molecular recognition toward antigens and patterned grooves on the substrate aligned them crossing perpendicularly. The peptide nanotubes were demonstrated to be smart electric functional nanomaterials since their electric properties could be tunable by controlled metal/semiconductor coatings on mineralizing peptides of the nanotubes,[173] and therefore the targeted assembly of these peptide nanotubes will enable one to produce complex electric circuits from the biomimetic bottom-up technique.

7.2 Experimental

7.2.1 Materials

α-hydroxy ω-thiol terminated polyethylene oxide (thiol-PEG, Mw 650) was purchased from Polymer Source Inc. Human IgG, anti-human IgG, mouse IgG, anti-mouse IgG, bovine serum albumin(BSA), N-hydroxysuccinimide (NHS), N-ethyl-N'-(3-dimethylaminopropyl)carbodiimide hydrochloride (EDAC), and 11-mercaptoundecanoic acid (MUA) were purchased from Sigma-Aldrich. All chemicals were used as received. Gold CD was purchased from Delkin Company. Si_3N_4 AFM tips (NSC15/Si3N4/Al BS) were purchased from MikroMasch.

7.2.2 3D assembly of peptide nanotubes on patterned gold substrate

Peptide nanotubes were self-assembled from bis(N-α-amido-glycylglycine)-1,7-heptane dicarboxylate with the previously published method.[28] In this experiment, the nanotubes in the diameter of 100 nm were used after they were extracted by the size-separation column.[174] A groove-patterned Au substrate was obtained by removing the polycarbonate layer covered on commercial Au compact disk (CD) (Delkin). To remove this layer, concentrated nitric acid (12M) was dropped on the backside of Au CD. Five minutes later, the Au substrate was rinsed with deionized water thoroughly and dried in N_2 atmosphere to complete the cleaning process. To coat the Au substrate with the protective layer, this Au substrate was immersed in thiol-PEG/ethanol solution (1mg/mL) at room temperature for 24 hrs for the formation of the self-

assembled monolayer (SAM) of PEG. The thiol-PEG SAM was used as the protective layer because it has the strong resistance for non-specific protein binding.[175, 176] Then the line was shaved on the PEG SAM in the groove by a Si_3N_4 tip of AFM (MFP 3D, Asylum research) and the dimension of line was designed by the MFP 3D nanolithography software. The resulting substrate was immersed in MUA/ethanol solution (1mg/mL) for overnight at room temperature to attach MUA molecules onto the shaved line via thiol-Au interaction. After rinsed with ethanol and dried the resulting substrate was incubated in the aqueous solution of NHS (25mg/mL) and EDAC (25mg/mL) for 30 min.[177] Then the substrate was rinsed with deionized water thoroughly and immersed with human-IgG in pH 7.4 PBS buffer solution (1mg/mL) for 12 h at 4 ˚C. Human-IgG was bound on the shaved line covalently via the condensation reaction between amino group of IgG and carboxylic group of MUA on the substrate. After the IgG-patterned substrate was rinsed with nanopore water and dried in N_2 atmosphere, the anti-human IgG-coated nanotubes was incubated in the pH 8 buffer solution containing the resulting substrate for 24 h at 4 ˚C. Next, we shaved the line in y-direction on the top level of the Au substrate by the AFM tip to cross the second nanotube perpendicularly on the first anti-human IgG nanotube. Mouse IgG was deposited on the newly shaved line covalently by the same method we patterned the human IgG line. The resulting substrate was rinsed with nanopore water thoroughly. When the anti-mouse IgG-coated nanotube was incubated in the pH 8 buffer solution containing the resulting substrate for 24 h at 4 ˚C, the anti-mouse IgG nanotube attached on the mouse IgG line on the top level of Au substrate to complete the crossbar fabrication from these nanotubes. This fabrication procedure is summarized in Scheme 7.1.

Scheme 7.1 The schematic representation of biological assembly of antibody-coated bionanotubes into the crossbar configuration.

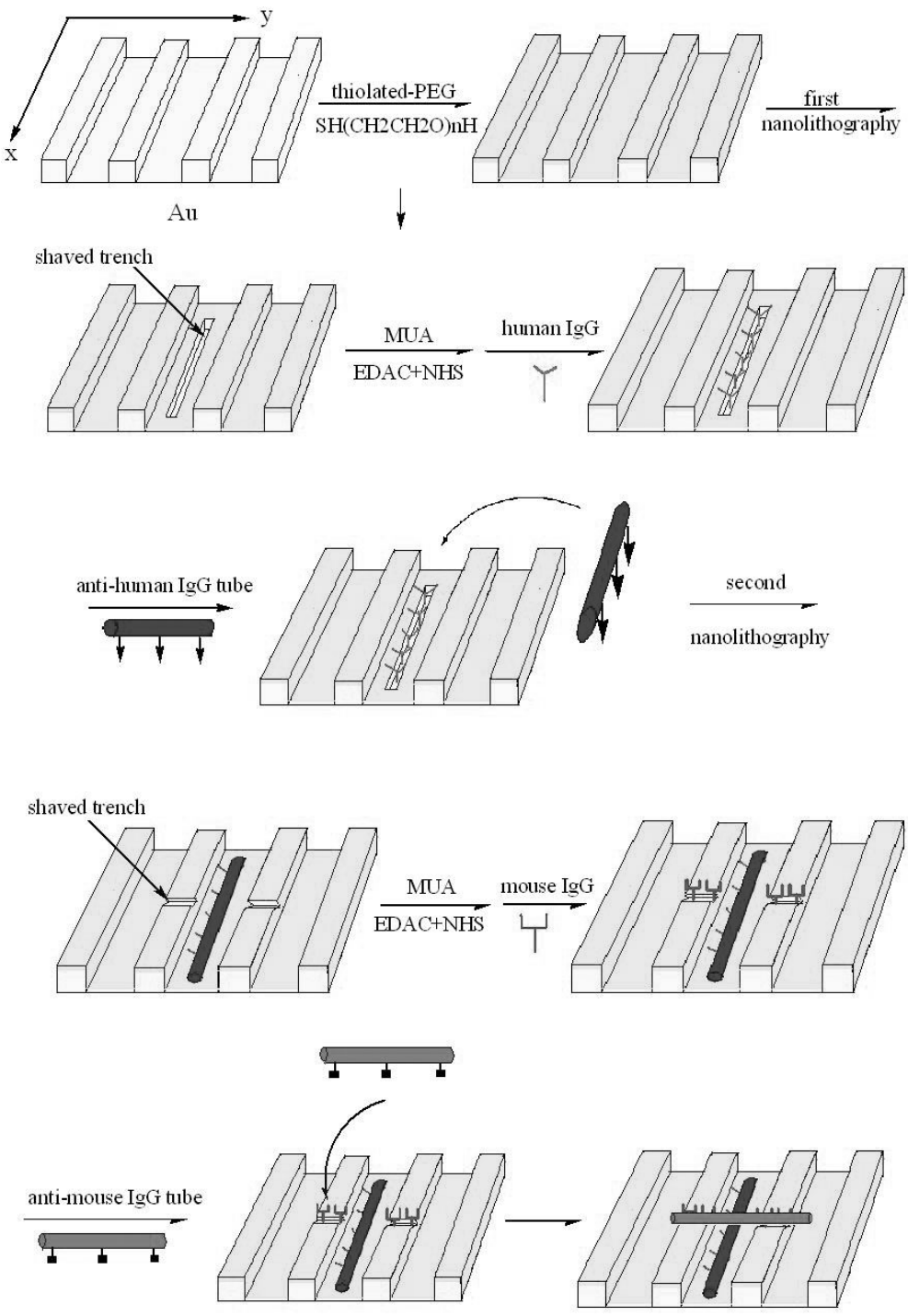

7.3 Results and discussion

In this work, we used peptide nanotubes as templates to decorate them with selected antibodies. These peptide nanotubes were self-assembled from the peptide monomer, bis(N-α-amido-glycylglycine)-1,7-heptane dicarboxylate, by three-dimensional hydrogen bonds between amide and carbonyl groups, and amides on the surfaces of nanotubes that do not be involved in the tube formation could bind antibodies to produce antibody nanotubes by using these peptide nanotubes as scaffolds. This antibody functionalization on the nanotube surfaces allowed the biomolecular-recognition-driven nanotube alignment on the antigen-patterned substrate as shown in Scheme 7.1. In this experiment, we used the peptide nanotubes in the diameter of 100 nm, extracted by size separation column.

To assemble these nanotubes into the crossbar geometry, we applied substrates that have grooves, as shown in Figure 7.1. As shown in Scheme 7.1, one type of nanotube was attached at the bottom of the groove in the horizontal direction while the other type of nanotube was placed on the top level of the substrate in the vertical direction via molecular recognition (Scheme 6.1). The gap of created by the groove gave special clearance for these nanotubes to cross each other. For this crossbar assembly of nanotubes, a commercial Au CD disk was used as the groove-patterned substrate. Figure 7.1A shows AFM image of the gold substrate (Delkin), and the darker areas and brighter areas correspond to the grooves and the top level of the CD substrate, respectively. From its sectional analysis (Figure 7.1B) the width of the groove is 600 nm and the depth of concave is 120 nm. This depth is large enough to accommodate the anti-human IgG-coated nanotube in the diameter of 100 nm inside the groove.

In order to immobilize the anti-human IgG nanotube in the groove, we patterned human IgG on the bottom of the groove by nanolithography.[146] The patterning of the antigen was achieved by two step; shaving protective layer, thiol-PEG SAMs, on Au substrate with the Si_3N_4 tip of AFM to expose Au surfaces and then attaching the antigen on the shaved area covalently via the amine (antigen) – carboxylic acid (MUA) conjugation. Figure 7.2A shows the AFM image of the shaved substrate. The fainted line appeared in a darker contrast in the middle of each groove is the shaved line, however these lines could not clearly imaged due to the fine dimension of the line; the depth and the width of the line is about 5 nm and 60 nm, respectively. After MUA was attached on the shaved areas via thiol-Au interaction and then human IgG was covalently immobilized with MUA via the NHS-EDAC coupling reaction, the originally darkened lines in Figure 7.2A turned to much brighter lines in the grooves as seen in Figure 7.2B. The sectional analysis of these lines before and after the IgG incubation further confirmed that the immobilization of human IgG in the groove was successful; Figure 7.2C showed that the height of the line on the groove is - 5 nm, however it is increased to + 10 nm after the immobilization of human IgG, as shown in Figure 7.2D.

When anti-human IgG-coated nanotubes were incubated on the human IgG-patterned Au substrate in solution, these antibody nanotubes selectively attached onto the human-IgG-patterned areas on the Au substrates (Figure 7.3A). This selective attachment on the antigen areas indicates that this nanotube assembly is driven by the antibody-antigen interaction. Next, in order to assemble the anti-mouse IgG-coated nanotube perpendicularly to the anti-human IgG nanotube on the Au substrate, we shaved a new line of mouse IgG along y direction on the top level of the substrate (black arrows in

Figure 7.3B). Here, we applied the same method used for the patterning of the human IgG line; first the MUA immobilization on the shaved areas and the covalent attachment of mouse IgG on the MUA lines via the NHS-EDAC coupling reaction. After MUA was attached on the shaved areas via thiol-Au interaction and then mouse IgG was covalently immobilized with MUA, the much brighter lines of the mouse IgG appeared on the top level of Au substrate in AFM image in Figure 7.3C. The section analysis of this mouse IgG line (Figure 7.3D) shows that the height of this line is consistent with the height of the human IgG line in the groove. Finally, when the anti-mouse IgG-coated nanotube was incubated on the resulting substrate in the solution for one day, this nanotube was attached on the mouse IgG line and this attachment completed forming the crossbar configuration of the nanotubes, as shown in Figure 7.3E. Here we fabricated the crossbar geometry of nanotubes in the two-step process since by that way we could clearly show that two antibody nanotubes could be placed in different locations and directions in a controlled manner; the anti-human IgG nanotube was aligned along the groove direction and the anti-mouse IgG nanotube was immobilized perpendicular to the groove direction. However, it is totally feasible to attach both anti-human and anti-mouse IgG-coated nanotubes simultaneously in one step on the Au substrate where the human IgG line and the mouse IgG line are already patterned by nanolithography before the nanotube immobilization.

It should be noted that the yield of the nanotube attachment along the groove direction was almost 100 %, however only around 20% trenches that are perpendicular to groove is anchored by antibody modified nanotubes. Recently, there were reports showing that the capillary force could have a significant effect to drive nanowires aligning parallel to

the groove direction.[160, 178] In the case of our nanotube alignment, the nanotube needs to resist against this capillary force to be immobilized perpendicular to the groove. While this capillary force likely diminishes the yield of the perpendicular attachment of the nanotube, 20 % of the nanotubes should not be immobilized in the direction normal to the groove without the antibody-antigen interaction. In other words, the antibody-antigen interaction could drive the nanotube to align against the capillary force. If the stronger molecular recognition such as the avidin-biotin system is applied for the perpendicular alignment of the nanotube, the yield of the perpendicular attachment could be increased drastically.

Figure 7.1 (A) AFM image of the bare Au substrate with grooves. (B) The sectional analysis at a white line drawn in (A). (Linglu & Nurxat)

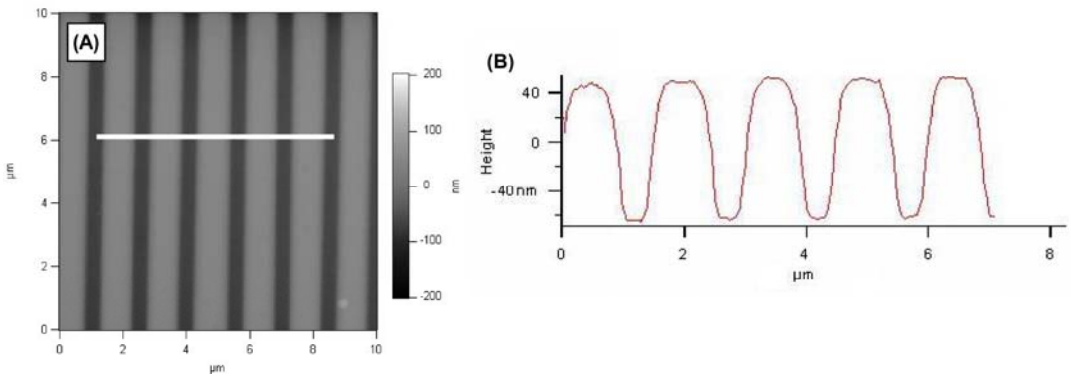

Figure 7.2 (A) AFM image of the Au substrate where the trench was shaved by AFM tips in the groove. (B) AFM image of the Au substrate where human-IgG was immobilized in the trench. (C) The sectional analysis at a white line drawn in (A). (D) The sectional analysis at a white line drawn in (B). (by Linglu & Nurxat)

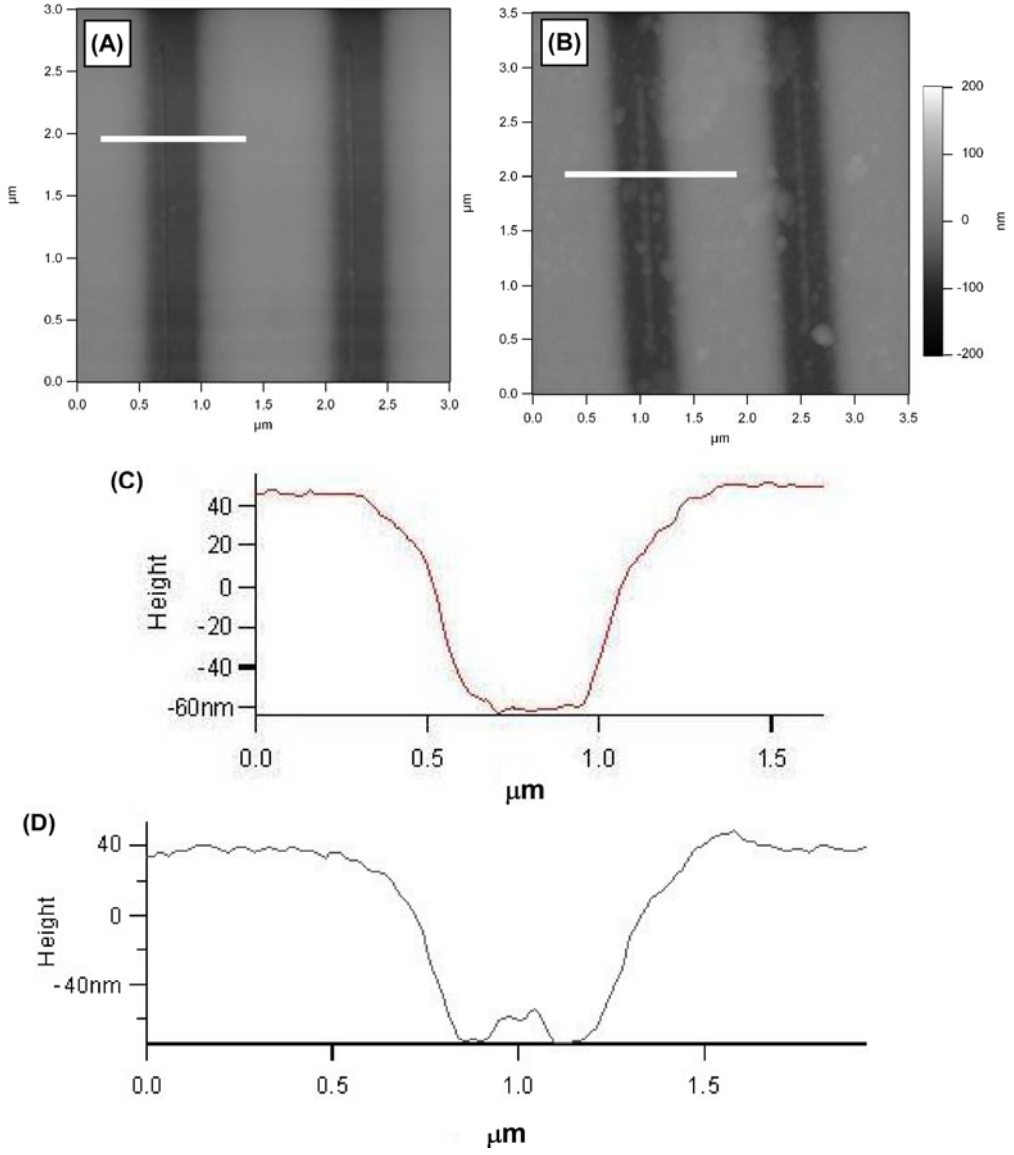

Figure 7.3. (A) AFM image of the anti-human IgG nanotube attached on the human-IgG line on Au substrate. (B) AFM image of the Au substrate (A) where the trench was shaved by AFM tips perpendicular to the groove. Black arrows show the position of the shaved line. (C) AFM image of the Au substrate (B) where mouse-IgG was immobilized in the trench. (D) The sectional analysis at a white line drawn in (C). (E) AFM image of the Au substrate (D) where the anti-mouse IgG nanotube attached on the mouse-IgG line. (by Linglu & Nurxat)

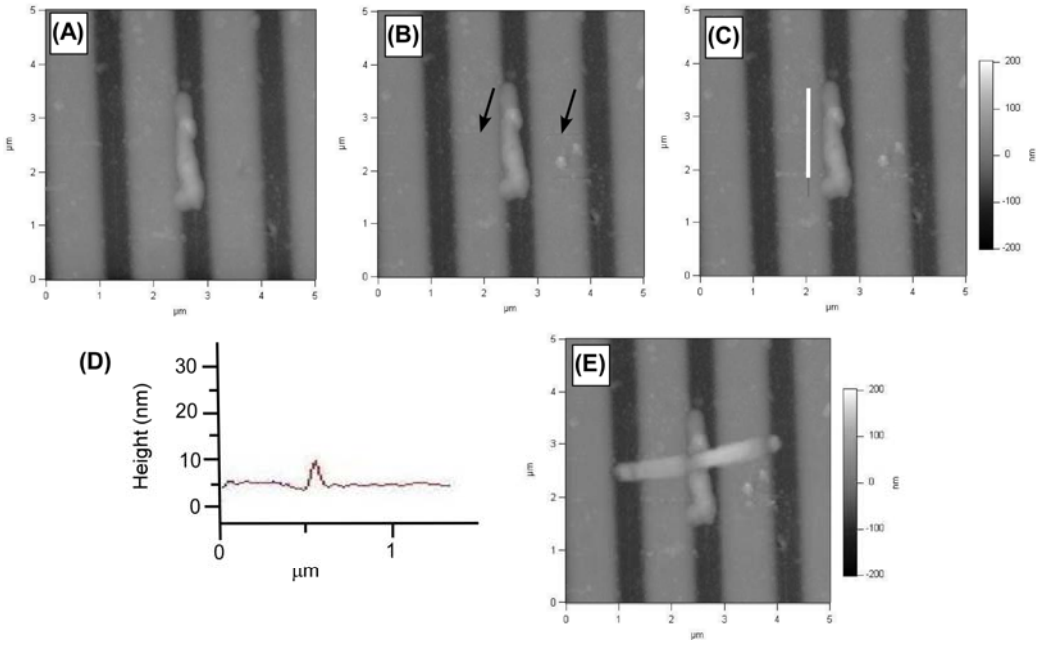

7.4 Conclusion

Antibody-antigen molecular recognitions enabled two types of antibody-functionalized bionanotubes to place them onto specific locations on substrates, where their complementary antigens were patterned. When two rectangular pads of antigens, human IgG and mouse IgG, were patterned perpendicularly on a Au substrate by nanolithography and then the anti-human IgG nanotube and the anti-mouse IgG nanotube were incubated on the Au substrate in solution, these bionanotubes were

attached onto corresponding locations to form the crossbar configuration. This biomimetic bottom-up fabrication method is robust and practical, and the crossbar assembly can be expanded to more complex logic gates such as AND, NOR, and OR by integrating multiple crossbared nanotubes.

Chapter 8

Self-Assembly of Au nano-particle containing peptide nano-rings on Surface[203]

8.1 Introduction

Recent improved two-dimensional and three-dimensional nanofabrication techniques allow one to build precisely designed structures in nanoscale for various photonic applications.[204-206] While the top–down approach has been applied for photonic crystal fabrications, the bottom–up approach via self-assembly of photonic nano-building blocks is also showing promising outcomes.[184, 207-214] For the bottom–up approach for the optics fabrications, synthesis of photonic nanomaterials and their alignments need to be accomplished efficiently and precisely. Biomineralization process, where peptides or proteins are utilized to mineralize metals and semiconductors, has been shown to produce various types of nanocrystals.[19, 20, 22, 23, 173, 215-222] Since the amino acid sequences are very sensitive to elements for their mineralization, optimized peptide sequences can produce nanocrystals efficiently.[150] In addition to the effective crystal growth, the amino acid sequences of mineralizing peptides could also influence the size, the alignment, and the shape of resulting nanocrystals.[17, 18, 27, 149] Further more, in some cases, peptides could mineralize nanocrystals in solution at room temperature that do not grow under the ambient condition.[136, 223] Because the size, the alignment, the shape, and the crystalline structure of photonic nanocrystals control optical properties of those assembled nanocrystals, the tunabilities of these features and the potential of new material

synthesis by using peptides will provide a significant advantage to apply peptides for photonic material syntheses. The one of smart approaches to create photonic materials by using mineralizing peptides is to pattern these peptides on surfaces based on photonic device designs and grow photonic crystals on the patterned peptides. For example, a hologram was applied to pattern silica-mineralizing peptides as an array and resulting silica nanostructures exhibited a nearly fifty-fold increase in diffraction efficiency over a comparable polymer hologram.[216] Recently, microfluidics and lithography were also used to pattern silica- and silver-mineralizing peptides for photonic applications.[17, 224]

In this report, we assembled ring-shaped peptide nanostructures as an array on surfaces. Previously, we developed the ring-shaped peptide nanostructures by self-assembling a peptide monomer, bis(N-a-amidoglycylglycine)- 1,7-heptane dicarboxylate and an organic Au precursor, trimethylphosphinegold chloride (AuPMe3Cl) in solution.[30] After reduction of Au ions trapped inside the cavities of nano-rings, the peptide nano-rings could template Au nanoparticles. In this report, after Au nanoparticleswere grown inside the cavities of the peptide nano-rings, these nano-rings containing Au nanoparticles were aligned on the chemically functionalized arrays patterned by nanolithography (Scheme 8.1). Since these peptide nano-ringswere self-assembled in a closely packed manner along the array of those dithiolated self-assembled monolayers (SAMs), these Au nanoparticles were positioned in the equal spacing on each line without touching each other as the peptide nano-rings functioned as spacers. This type of alignment of nanomaterials with spacers can be very useful for improved photonic crystal designs.

Scheme 8.1 Illustration of Au nanoparticle-containing peptide nano-ring assembly on the patterned Au substrate.

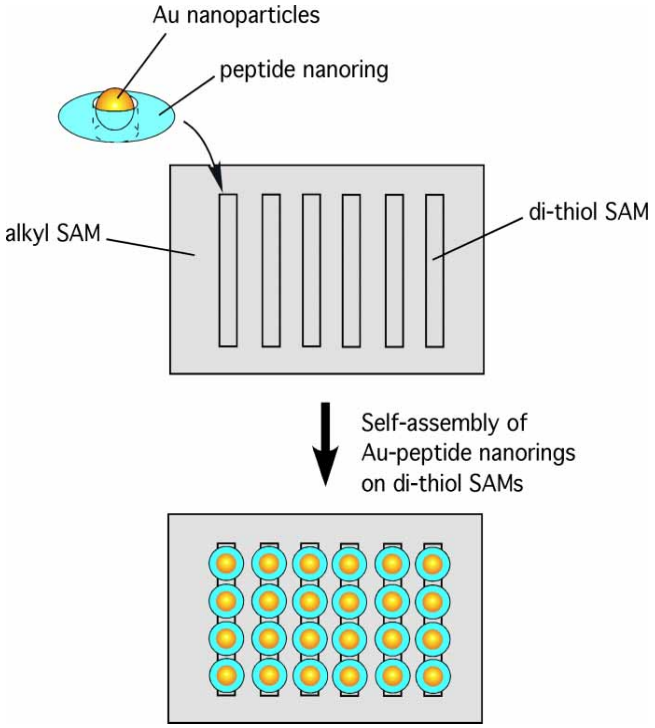

8.2 EXPERIMENTAL

8.2.1 Materials

Bis(N-a-amido-glycylglycine)-1,7-heptane dicarboxy-late was synthesized and recrystallized in our lab by the published manner.[28, 29] 1-Ethyl-3-[3-(dimethyl-amino)propyl]carbodiimide hydrochloride (EDAC), N-hydroxysuccinimide(NHS),2-mercaptoethylamine, trimethylphosphinegold chloride, 16-mercaptohexa-decanoic acid and octadecanothiol from Aldrich. Annealed gold substrates from Molecular Imaging. Aseriesoftrenches(100 nm 1 mm) were made by shaving the alkylthiol SAM with a Si_3N_4 tip (Veeco Metrology) of the AFM (Nanoscope IIIa and MultiMode microscope,

Digital Instruments). Thesetrencheswereмadeby customized Nanoscript software (VeecoMetrology). Formvar Film 200 Mesh Cu TEM grids were obtained from Electron Microscopy Sciences. UV-Lamp (14 mW/cm^2, 254 nm).

8.2.2 Preparation of Peptide Nano-rings

After peptide monomer of bis(N-a-amido-glycyl-glycine)-1,7-heptane dicarboxylate, 0.028 g, was dis-solved in 10 mL of water and the pH of this solution was adjusted to 5.5 with citric acid, an excess amount of an organic Au precursor, trimethylphosphinegold chloride ($AuPMe_3Cl$) was added to this solution. After 5 days in the dark, the peptide nano-rings were observed in an outer diameter of 50 nm and an inner diameter of 15 nm. The nano-ring solution was washed with deionized water and centrifuged at 14.5 krpm, and then Au ions trapped inside the peptide nano-rings were reduced by a UV light (14 mW/cm^2, 254 nm) for 20 min. The resulting Au nanoparticles were observed to be about 15 nm in an average diameter from AFM images.

8.2.3 Nanolithography on Au Substrates

In order to pattern the peptide nano-rings containing Au nanoparticles in their cavities as an array on Au substrates, an array of dithiolated SAMs was patterned by a cantilever of an atomic force microscope (AFM) with the following sequence. First, 1-octadecanethiol (0.01 mM) was self-assembled on Au substrates in 99% ethanol at room temperature for 12 h. Then, an array of trenches (100nm 1 mm) was created by removing the alkylthiol SAMs by the tip of AFM via nanolitho-graphy technique[132, 146, 172, 225]. On these trenches where Au surfaces were exposed, 16-mercaptohexa-decanoic acid (0.01 mM) was self-assembled for overnight. After the resulting substrates were

washed by deionized water, the end groups of the SAMs on trenches were functionalized by thiol via substituting carboxylic acid groups with thiol groups as shown in Scheme 8.2. In Scheme 8.2, 400 mL of ethyl-3-[3-(dimethylamino)propyl]carbodiimide (EDAC, 75 mM) and 400 mLof N-hydroxy succinimide (NHS, 15 mM) were immersed in aqueous solution containing the functionalized Au substrates for 30 min. Then, as shown in the step 3 in Scheme 1, 800 mL of 2-mercaptoethylamine (15 mM,) was incubated in the solution for 24 hrs to modify the ends groups of the SAMs in trenches to thiol groups.

8.2.4 Self-assembly of Au Nanoparticle-containing Peptide Nano-rings on Surfaces

When the peptide nano-rings containing Au nano-particles in their cavities were mixed with the dithiolated SAM-patterned surfaces in aqueous solution for 8 hrs, the nano-rings were self-assembled on the trenches with the thiol-Au interaction. After these substrates were washed with deionized water, the attachment of the peptide nano-rings on the arrayed trenches was confirmed by AFM. While the height mode of AFM imaging was used to probe the topology of the nano-ring assembly, the phase mode of AFM imaging was applied to probe the location of Au nanoparticles since the distinguished hardness of surfaces between Au nanoparticles and peptide nano-rings allows us to image them respectively in the trenches.

We also assembled the peptide nano-rings contain-ing Au nanoparticles on TEM grids by spin-coating to examine whether the nano-rings can be packed on surfaces without distraction. To obtain smooth surfaces of TEM grids, these grids were fixed on the top

of mica substrates, which were also attached on AFM metal pucks. After the Au nanoparticle-contain-ing peptide rings were spin-coated on the TEM grids, the resulting coatings were examined by AFM.

8.3 RESULTS AND DISCUSSION

When the peptide monomers were self-assembled in the presence of the water-insoluble trimethylphosphinegold chloride ($AuPMe_3Cl$) for 5 days in the dark, the ring-shaped peptide assemblies were observed in solution. The average outer diameter of nano-ring was 50nm and the average inner diameter was 15nm.[30] Our previous spectroscopic investigation showed that these peptide nano-rings were self-assembled from the peptide monomers and the organic Au salts by chelating Au with amide groups of the peptide monomers. After UV light was irradiated to the nano-ring solution for 20 min Au nanoparticles were grown inside the cavities of nano-rings, however the organic Au salts, trapped inside the cavities, were reduced to grow Au nanoparticles in the middle of nano-rings.[30, 148] In a TEM image of the nano-ring after reduction of Au ions, the Au nanoparticle appeared darker at the center of the nano-ring (Figure 8.1a). These particles in the cavities were also confirmed as Au nanoparticles by electron diffraction before their surface assembly on the dithiol SAMs. When the peptide nano-rings were previously synthesized, they were observed to be stable in solution[30] however these nano-rings have not been assembled on surfaces. Therefore, it was necessary to examine their stability via the simplesurface-assembly. Before fabricating the structure shown in Scheme 8.1, we examined whether the Au nanoparticle-containing peptide nano-rings are rigid enough to be self-assembled on surfaces by spincoating them on

TEM grids. A height image of AFM in Figure 8.1 b confirms that the nano-rings were deposited

FIGURE 8.1 (a) TEM image of the peptide nano-ring containing a Au nanoparticle inside the cavity, scale bar 50 nm. (b) AFM image of spin-coated peptide nano-rings containing Au nanoparticles in their cavities on TEM grids in height mode, scale bar 80 nm (c) AFM image of spin-coated peptide nano-rings containing Au nanoparticles in their cavities on TEM grids in phase mode, scale bar 80nm (d) the phase AFM phase image in high magnification, scale bar 40nm. (by Nurxat & Jacopo)

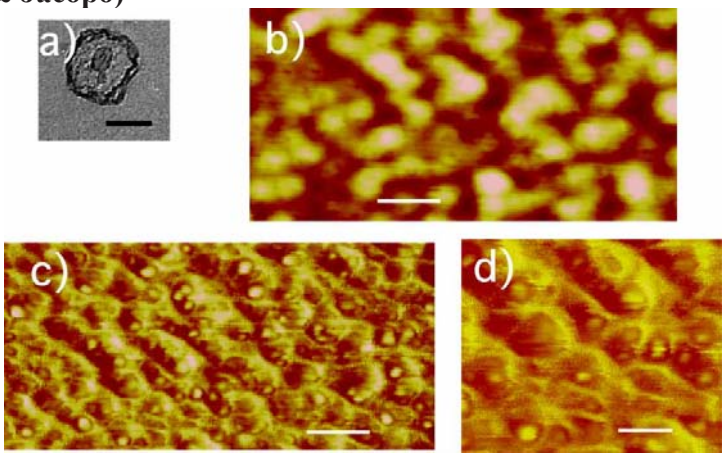

on a TEM grid. This figure imaged the assembly of the nano-rings on the surface, but the Au nanoparticles inside the nano-rings could not be resolved in this AFM height image. However, when this assembly was imaged by the phase mode of AFM as shown in Figure 8.1c, the Au nanoparticles were observed as a brighter contrast inside the nano-rings because harder surfaces of Au nanoparticles appeared brighter than softer surfaces of the outer peptide nano-rings. In the magnified phase image of Figure 8.1d, these Au nanoparticles were not exactly located at the center of the nano-rings, which may be due to the deformation of the nano-ring shape via spin-coating and the multiple orientations of the nano-rings on TEM grids. Since the peptide nano-rings were stable enough to be assembled on TEM grids via spin-coating, we examined the targeted

self-assembly of the peptide nano-rings on the functionalized surfaces. The functionalized array of dithiol SAMs was patterned by three steps. First, alkyl SAMs were deposited on a Au substrateandthearraywaspatternedbyremoving the alkyl SAMs with the AFM cantilever. Then, mercaptohexadecanoic acid was assembled on the curved array where Au surfaces were exposed. The carboxylic groups on the top of these SAMsontrenches were substituted by thiol groups, as shown in Scheme 8.2.

SCHEME 8.2 Fabrication of dithiol SAMs on patterned Au substrates.

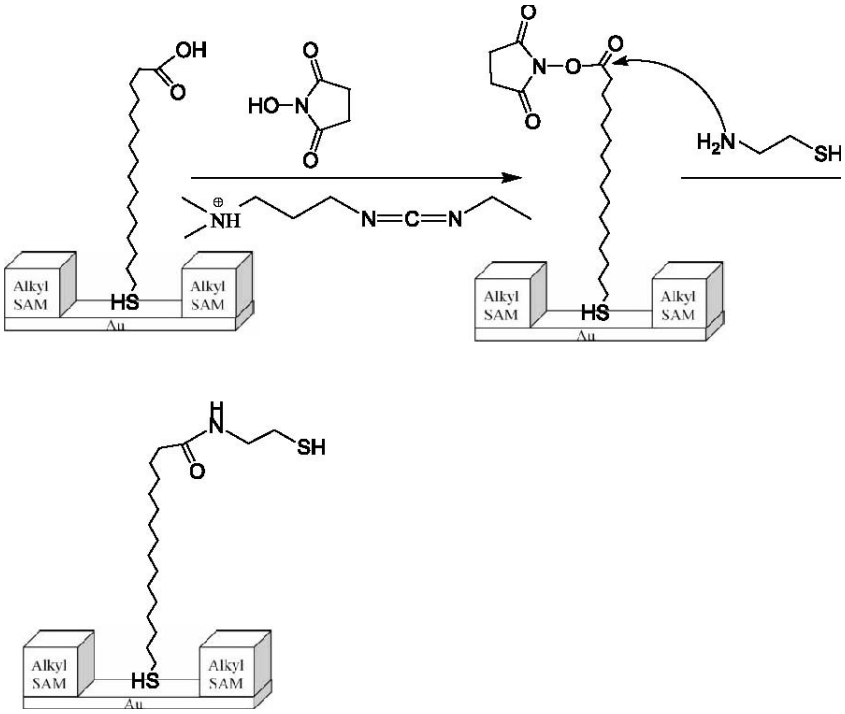

To align the peptide nano-rings containing Au nanoparticles on the dithiol SAM array patterned on a Au substrate as shown in Scheme 8.1, these nano-rings were incubated with this substrate in solution for 8 h. Because the end groups of the SAMs on the trenches were functionalized by thiol (Scheme 8.2), this incu-bation process allowed the nano-rings to self-assemble onto these trenches with the thiol-Au interaction, as

shown in Figure 8.2. Figure 8.2 a is the AFM image of the patterned substrate in the height mode after the nano-rings were incubated in the substrate-containing solution. The peptide nano-rings were closely packed to form the array of continuous lines along the trenches

FIGURE 8.2 AFM images of Au nanoparticle-containing peptide nano-rings assembled on the dithiol SAM-patterned in (a) height mode, scale bar 300 nm (b) phase mode, scale bar 300nm (c) height mode in high magnification, scale bar 50 nm, (d) phase mode in high magnification, scale bar 50nm. (by Nurxat, Jacopo, Kai, & Amit)

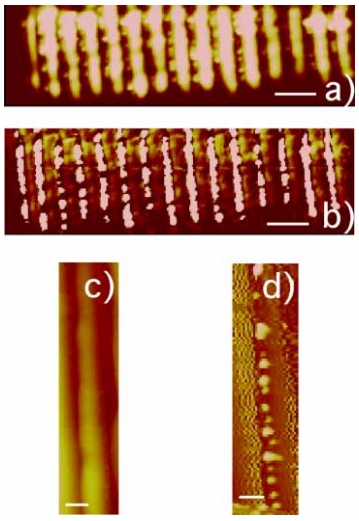

In Figure 8.2 a. As seen in the height mode AFM image of the spin-coated samples in Figure 8.1b, the individual Au nanoparticle inside the nano-ring could not be identified in Figure 8.2 a due to their small height difference between the peptide nano-ring and the Au nanoparticle. However, when the phase mode of AFM was applied to image this substrate, the deposited spheres on the trenches looked less continuous in Figure 8.2b since the brighter spheres in this phase image are more likely Au nanoparticles due to

their surface hardness as compared to the one for the peptide nano-rings. While these AFM images in the phase mode in low resolution do not explicitly show the discrete positioning of Au nanoparticles inside the nano-rings aligned on the trenches as shown in scheme 8.1, the high-resolution image of the single trench containing the peptide nano-rings in the phase mode assisted visualizing the peptide nano-ring alignment more clearly. When the single trench was imaged with the height mode image in high-resolution (Figure 8.2 c), still only continuous packing of the nano-rings was observable as a line along the trench and the discrete Au nanoparticles could not resolve. But when the single trench was imaged in the phase mode in high-resolution, the discrete alignment of Au nanoparticles was observed, as shown in Figure 8.2 d. In this high-resolution image, the harder Au nano-particles appeared to be brighter and the spacing between these nanoparticles was visible. The most of Au nanoparticles in Figure 8.2d were self-assembled discretely without touching each other due to the spacing of the peptide nano-rings (scheme 8.1). The darker nano-ring contrast around the Au nanoparticle, observed in the spin-coated sample in Figure 7.1b, was not observed clearly in Figure 8.2 d, however this phase contrast difference between the spin-coated nano-rings and the self-assembled nano-rings may be caused by their topological difference. For the spin-coated sample the nano-rings were forced to pack closely by the external force on very smooth and flat TEM grids, and the resulting nano-ring monolayer also became relatively flat. Therefore, the detailed structure of nano-rings and Au nanoparticles was resolved in the AFM image of the spin-coated nano-ring sample due to the flatness of the coating. However, for the self-assembled sample, the nano-rings were self-assembled on rough surfaces consisting of alkyl

SAMS and dithiol SAMs in different heights. The trenches were also not flat because the AFM cantilever could not shave alkyl SAMs smoothly and it further scraped the Au substrate partially. Shaved SAMs and Au substrate were piled at the edges of trenches, which also increased the roughness of the substrate. Since all different heights of SAMs, trenches, and edges contributed unevenness of the surface topology, the AFM resolution in the phase image on this self-assembled sample was degraded due to its surface roughness and it prevented to map the locations of the nano-rings and Au nanoparticles in the phase image.

When the neat Au nanoparticles without the peptide nano-rings were assembled on the same dithiol-functionalized trenches, those Au nanoparticles were aligned as continuous lines without spacing in their phase AFM image. This observation supports that the Au nanoparticles observed in Figure 8.2 d were separated by the peptide nano-rings otherwise the spacing between Au nanoparticles should not be imaged. It should be noted that some of these nanoparticles seem to contact each other in Figure 8.2 d due to the deformation of the nano-rings during the self-assembly, which was also observed in the spin-coated sample in Figure 8.1.

8.4 CONCLUSION

The peptide nano-rings containing Au nanoparticles inside their cavities were aligned on dithiol SAMs patternedasanarraybyAFM-basednanolithography. The peptide nano-rings were self-assembled as lines on these SAMs, and Au nanoparticles inside the nano-rings also formed lines with the spacing between these nanoparticles as the peptide nano-rings functioned as spacers. This type of fabrication will provide improved tunability in their optical properties of resulting nanoparticle-assembled

arrays. In addition, optimization of the inter-particle distance of nanoparticles in the array with various spacers may allow one to design new types of photonics with desired optical properties. However, for those optical applications, the stability and the rigidity of the nano-rings will be more desirable to be improved since some of the nano-rings were deformed during the self-assembly and this deformation caused the uneven spacing of the nanoparticles on the array. For realistic photonic applications, the nanoparticle assembly needs to be accomplished without deformation because they require the perfect alignment of nanoparticles with minimum defects. The additions of hydrogen-bonding functional groups or polymerizing groups to the monomer may increase the rigidity of the nano-rings, which may help overcome this problem.

Chapter 9

Study of Au Nanoparticle Growth on the Au Mineralizing Peptide Patterns drawn by AFM- Nanolithography

9.1 Introduction

Superior and distinguished physical properties of nanomaterials such as nano-tubes and nano-wires have been widely exploited in last decade, however assembly of the device configuration using these superior nano-scale building blocks is currently challenging[154, 156-159]. Bottom-up methods have been extensively explored to fabricate nano- scale devices in electronics, optics, actuators, and sensors[135, 184, 226, 227]. For the bottom–up approach for the optics fabrications and addressing nano-wires at precise locations for the interconnection between electrodes, synthesis of the nano-material building blocks and their alignments need to be accomplished efficiently and precisely.

Various types of nano-crystals have been synthesized by biomineralization process, where peptides or proteins are utilized to mineralize metals and semiconductors[19, 22, 215, 216]. The amino acid sequences of mineralizing peptides could also influence the size, the alignment, and the shape of resulting nanocrystals[17, 18, 149]. In certain condition, peptides could produce unusual crystalline structure in solution at room temperature that do not grow at ambient condition[43, 55, 228]. Since the size, the alignment, the shape, and the crystalline structure of nano-crystals could tune optical and electrical properties of those assembled nano-crystals, the synthesis and assembly

of new materials using biomineralizing peptides will provide a significant route to fabricate the new device.

In our previous work, in order to fabricate electronic circuits, we used the bionano-technology approach to create nanometer-scale electronic circuit geometries by anchoring peptide nanotubes[132, 153, 171, 229], whose ends were functionalized by "linking proteins" on the complementary receptor-placed areas of the substrate. The electronic properties of the circuit can be tuned by controlling size and packing density of particles on the sidewall of tube, which was coated with "mineralizing peptides"[150, 174]. The tubes, in which the sidewalls of tube were coated with metal or semi conductor nano-particles and the ends of tube were coated with "linking proteins", are designated to make logic gate geometries. In addition, we assembled these ring-shaped peptide nanostructures [203]as arrays on surfaces using SPM-based nanolithography. The tunable spacing between the nano-crystals was adjusted by the controlling the dimension of the peptide nano-rings and functioned as photonic spacers. The novel fabrication methodology provided a feasible approach to control the photonic properties of resulting nano-partisqcle arrays.

To in situ fabricate tunable and aligned nano-particles on the surfaces for nano-devices, the biomineralization process was applied in the SPM based nanolithography bottom–up approach. The mineralizing peptides were firstly patterned on to the surface combining with bioresistive spacers. Corresponding peptides were used to implement the requirement of materials in device. Parameters including pH of solution, spacer, and the nature of peptides were monitored to control the size, inter-particle distance, and shape of nano-particle arrays.

9.2 EXPERIMENTAL

9.2.1 Materials

1-Ethyl-3-[3-(dimethyl-amino)propyl]carbodiimide hydrochloride (EDAC), N-hydroxysuccinimide(NHS),2-mercaptoethylamine, trimethylphosphinegold chloride, 16-mercaptohexa-decanoic acid (MHA) and octadecanethiol from Aldrich. Annealed gold substrates from Molecular Imaging. Silicon substrate from Virginia Semiconductor, Inc. Si_3N_4 AFM tips (NSC15/Si3N4/Al BS) were purchased from MikroMasch.

9.2.2 Nanolithography on Au Substrates

In order to pattern Au nanoparticles as an array on Au substrates, an array of HRE peptide was patterned by a cantilever of an atomic force microscope (AFM) with the following sequence. First, $SHC_{11}H_{22}$ (CH_2CH_2O) $_3OH$ (1 mM, 2 ml) was self-assembled on Au substrates in 99% ethanol at room temperature for 12 h. Before the substrate was removed, a 5-10 fold excess volume of ethanol was added. The substrate was grasped with clean forceps and removed quickly from the solution to minimize the formation of a langmuir film of compound over the SAM surface. After removal from the SAM solution, the substrate was swished in 3 successive beakers filled with 100% ethanol. After that, it was dried in a stream of nitrogen. Next, an array of trenches was created by removing the thiol SAMs by the tip of AFM via nanolithography technique in air. The resulting substrate was immersed in 16-mercaptohexadecanoic Acid (MHA)/ethanol solution (1 mM, 2 ml) at room temperature overnight to attach MHA molecules onto the shaved trenches via thiol-Au interaction. Next, the substrate was

removed from the solution and rinsed with ethanol and dried. The resulting substrate was incubated in 1 ml of the aqueous solution of NHS (50mM) and EDAC (200mM) for 15 min at room temperature.[153] Then the substrate was rinsed with MES buffer thoroughly and immersed in 1 ml of 1 mg/ml of AAHAAHAAD (HRE) in pH 7.4 PBS buffer solution for 12 h at 4 ˚C. The substrate was passivated with 2 ml of 10 mM solution of ethanol amine. Then it was rinsed with PBS buffer and it was incubated in 3 ml of 0.1 mM $HAuCl_4$ for one day. Next, 30 ul of 1% $NaBH_4$ was added to the 3ml solution of 0.1 mM $HAuCl_4$. The substrate was removed from that solution after incubating for two hours and it was rinsed with water upon removal. Finally, the substrate was dried by nitrogen gas flow. The substrate was then checked by Tapping Mode AFM for results. When an organic gold salt (Chloro-trimethyl-phosphine gold) was used instead of $HAuCl_4$, the procedure followed is described in the literature[174].

When silicon substrate was used, the substrate was incubated with the mixture of nitric acid and hydrochloric acid at the ratio (3:7) for 30 minutes. The substrate was rinsed with water and ethanol respectively. Then it was incubated in 2ml of toluene solution of 0.1 mM PEG silane overnight for SAM formation. After the substrate was rinsed with ethanol and dried, trenches were made with silicon nitride coated AFM tips using nanolitho-program. The resulting wafer was incubated in 2ml Toluene solution of 0.1 mM aldehyde silane ($OHC(CH_2)_{10}Si(OC_2H_5)_3$) to form the self assembly monolayer of aldehyde molecules following the siloxane bond formation between hydroxyl groups on the silicon wafer and alkoxyl group of aldehyde silane. After being rinsed with water, the resulting substrate was incubated with 1 ml PBS

buffer solution of 1 mg/ml HRE. A 2 ml solution of tris buffer (0.1 M, pH 8.6) and 3 mg of organic gold salt was prepared in which the silicone wafer was incubated for two days. The vial containing the entire assembly was wrapped with aluminum foil to avoid light. After two days, 6 ul of 16 M hydrazine hydrate was added to the above solution and incubated for 1 day. The substrate was checked with TM AFM after rinsing it with water.

9.3 Results and Discussion

In this work, both dip pen nanolithography (DPN) and nano-grafting techniques were applied to provide designated areas for immobilization of biominerilizing peptides, which were used to grow the metallic[148] or semiconducting[19, 22, 215] nanocrystals. The bio-mineralizing peptides for specific ions were selected from phage display library technique[55].

This work is to study the controlled growth of metal and semiconductor nano-particles on silica and gold surface using bio-mineralization and apply them as potential electronic logic gates and photonic device. Various types of nano-crystals have been synthesized by biomineralization process, where peptides or proteins are utilized to mineralize metals and semiconductors[19, 22, 215, 216]. The amino acid sequences of mineralizing peptides could also influence the size, alignment, and the shape of resulting nanocrystals[17, 18, 149]. In certain conditions, peptides could produce unusual crystalline structure in solution at room temperature that do not grow at ambient conditions[1, 43, 228]. Since the size, alignment, shape, and the crystalline structure of nano-crystals tune the optical and electrical properties of those assembled

nano-crystals, the synthesis and assembly of new materials using biomineralizing peptides will provide a significant route to fabricate the new device.

The purpose of the in situ fabrication of tunable and aligned nano-particles on the surface using biomineralization process for nano-device in this report is to avoid the complicated process of fabrication of nano-devices. For example, in the traditional way, first of all, the tunable building blocks are manufactured, and then they are assembled. However, in this study, we fabricated the nano-structured materials and formed the tunable building blocks simultaneously using a combination of bio-mineralization process and SPM-based nanolithography. The SPM-based nanolithography provides the chance of generating nano-scale building blocks and patterns. The immobilized bio-mineralizing peptides on the solid surface generate the tunable building blocks on the device surface, not on the template of building blocks.

For the study of nano-crystal growth, gold nano-particle was chosen since synthesis procedure of gold was well-developed, and also the specific peptide (HRE) was readily available in our group.

1) Dip Pen Nanolithography (DPN)

In DPN methodology, the bio-mineralizing peptides were transported to the area from AFM tip: peptides as ink and AFM tip as a pen. In order to successfully deposit the peptides from AFM tip, first of all, the silicon wafer containing self assembly monolayer (SAM) should have a strong affinity for the peptides. As a result, the silicon wafer was incubated with toluene solution of aldehyde (OHC $(CH_2)_{10}Si(OC_2H_5)_3$) and afterwards, cleaned with a mixture of concentrated hydrochloric acid and concentrated sulfuric acid (the volume ratio 1:3). The transported peptides were

chemically bound to the aldehyde surface with amide bond formation between the amine group of peptide and aldehyde group of silane moleculues from SAM. The rest of the area was deactivated with bio-inert amine functionalized polyethylene glycol molecules. Next, the silicon wafer was incubated in tris buffer solution of 3mg organic gold salt(Chloro(trimethyl phosphino)Gold(I)) for two days. Then 6ul of 16M hydrazine hydrate was added to reduce the gold(I) ion into gold metal[148].The whole procedure is illustrated in scheme(9.1).

Scheme 9.1 The procedure of gold NPs on silicon wafer using DPN methodology

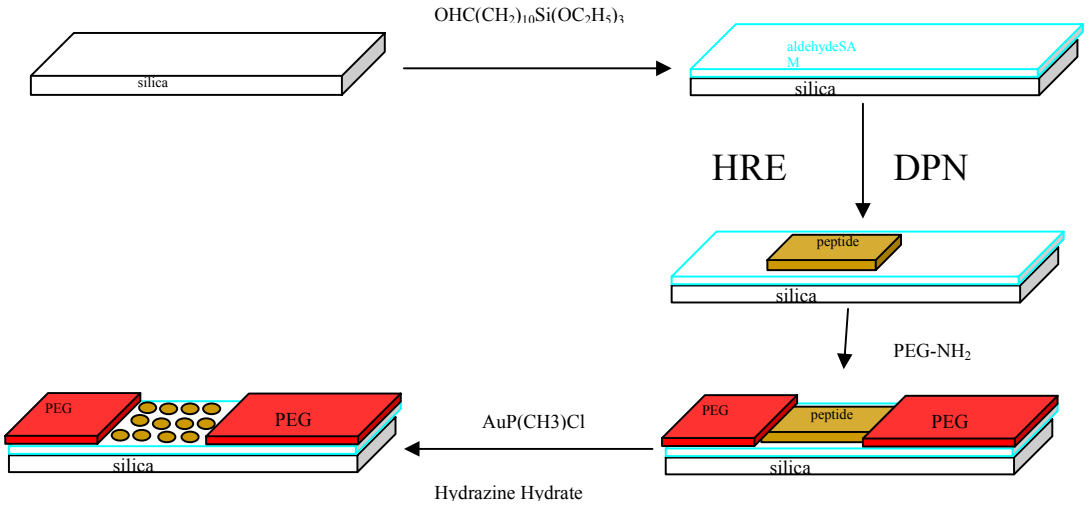

The surface roughness of silicon wafer was found to be around 1nm from the section analysis (Figure 9.1). The silicon tip was incubated with 1 ml of 500ug/ml peptide solution for 5minutes, and immediately after, the tip scanned 25um^2 area with contact mode and sample lines of 125. Due to the surface roughness of silicon wafer, it is very difficult to obtain the LFM image of the patterned area for further verification of covalently bound peptide. However, the patterned area was easily

differentiated by phase image and height image (figure 9. 2 & 9.3) after the solution containing Au(I) ion and wafer was reduced by hydrazine hydrate. In the far-sighted view of the gold nanoparticle patterned image (Figure 9.2 (A),(B),(C)), the patterned area seems square in that as the peptides were transported from tip as ink. The tip exactly scanned 25um^2 area. After the growth of gold nano-particles in the patterned area, the region became more visible. The appearance of discontinues lines in the pattern is due to the roughness of the surface and the difficulty in controlling the parameters such as humidity, temperature, the tip velocity, etc. Especially, the phase image of the patterned area clearly shows that the gold particles existed in the patterned areas. Also gold particles in the area had a different contrast due to their hardness compared to the peptide assembled region. The height of the gold nano-particles was 6nm. This is consistent with the data provided by literature[150]. Due to the difficulty in reproducibility of DPN method, the nano-grafting method was applied to the silicon wafer.

The transportation of the molecules by DPN is related to a lot of parameters such as humidity, temperature, the affinity of molecules to the surface of substrate, surface roughness, contact force, tip velocity, etc. For example, in the literature[230], the transportation of alkane thiol to gold surface was performed in 40% humidity. However, for transporting peptide molecules to surface, higher than 70% humidity[231] was required. The molecules should have strong affinity to the surface, i.e. gold thiol interaction etc., otherwise it is very difficult to transport molecules from tip to surface.

Figure 9.1 height image of silicon wafer and section analysis of surface roughness. (by Nurxat)

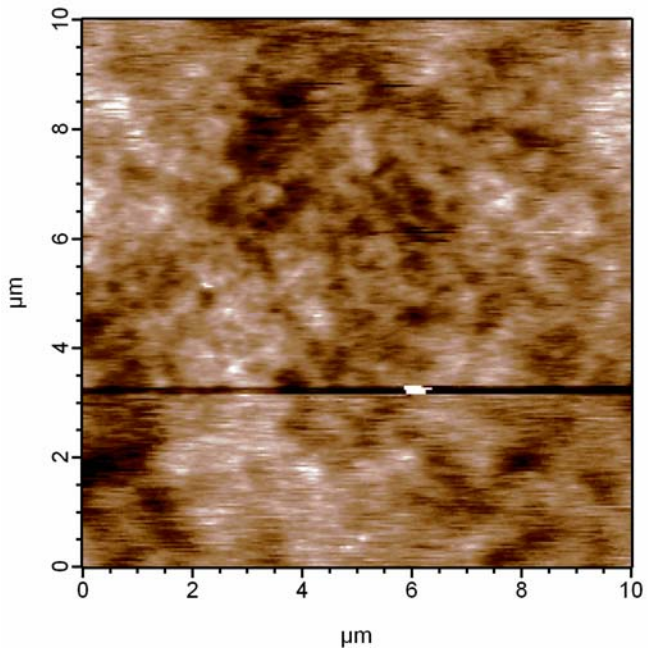

Figure 9.2 Far-site view: (A) Height image (B) Amplitude image (C) Phase image of gold nanoparticle growth after peptides transported by DPN and the reduction of gold ions. Near-site view: (D) Height image (E) Amplitude image (F) Phase image of the images (A),(B), and (C). Height image of random gold nanoparticles on one layer PEG-coated silicon wafer surface without addition of HRE peptides. (by Nurxat)

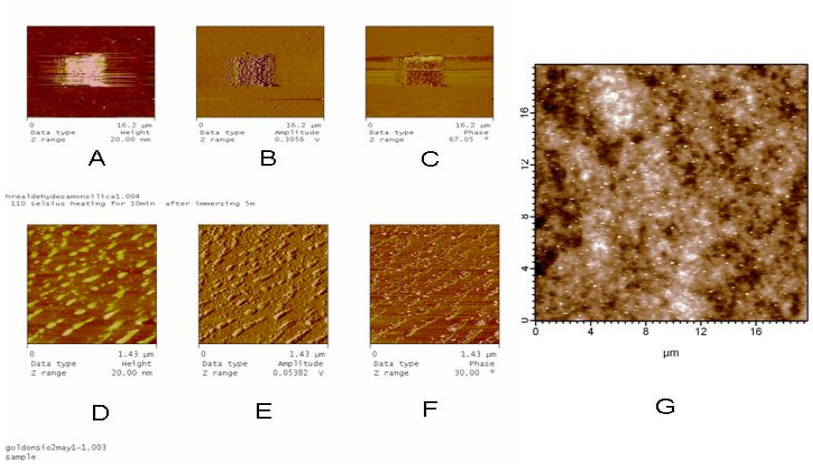

2) nanografting method for silicon wafer

As shown in scheme 9.2, bioresistive PEG monolayer was formed on silicon wafer surface and then the silicon nitride tip removed the layer by scraping with the contact force of 20uN(Figure 9.3). Due to the roughness of silicon wafer and small size of peptide molecules, the observation of the patterned area with height increase was very difficult. However, the substrate was scanned after gold reduction. The formation of gold nanoparticles in the patterned areas was clearly visible as shown in the figure 9.4. Compared to the gold substrate, it is relatively difficult to get good self assembly monolayer on silicon wafer surface due the inter molecule polymerization of alkoxide silane when the alkoxide silane start to assemble on the silicon surface. The very important step of assembly of protective layer is to generate more hydroxyl groups on silicon wafer. Otherwise this affect the formation of SAM on silicon wafer surface. The above uncontrollable parameters caused that the background had small particles and discontinuity in the patterned areas in figure 9.4.

Scheme 9.2. Procedure to form gold array on the silicon wafer

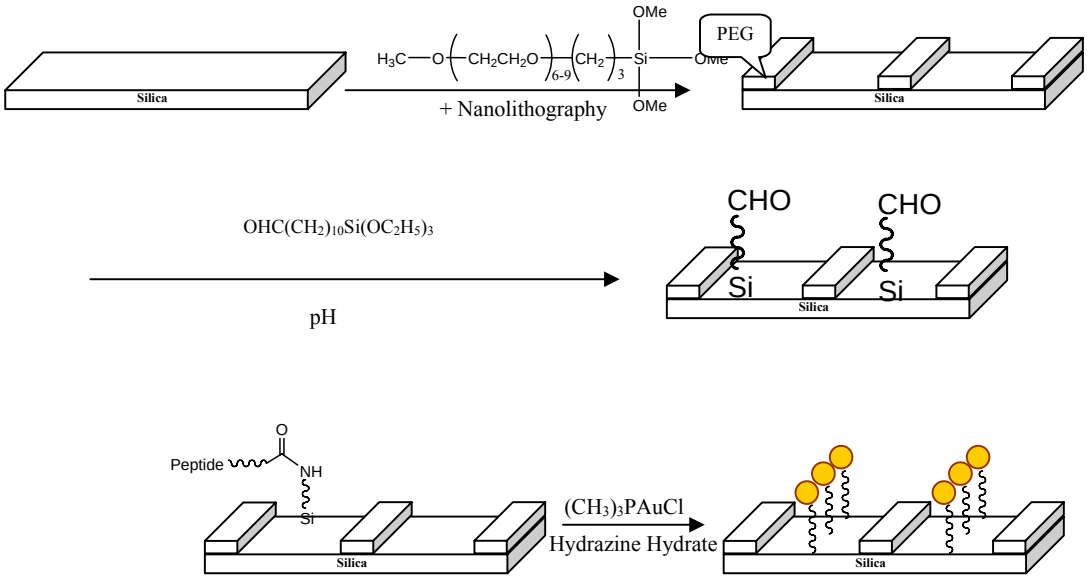

Figure 9.3 The height image of silicon wafer after scratched with Silicon nitride tip at contact force of 20uN. (by Nurxat)

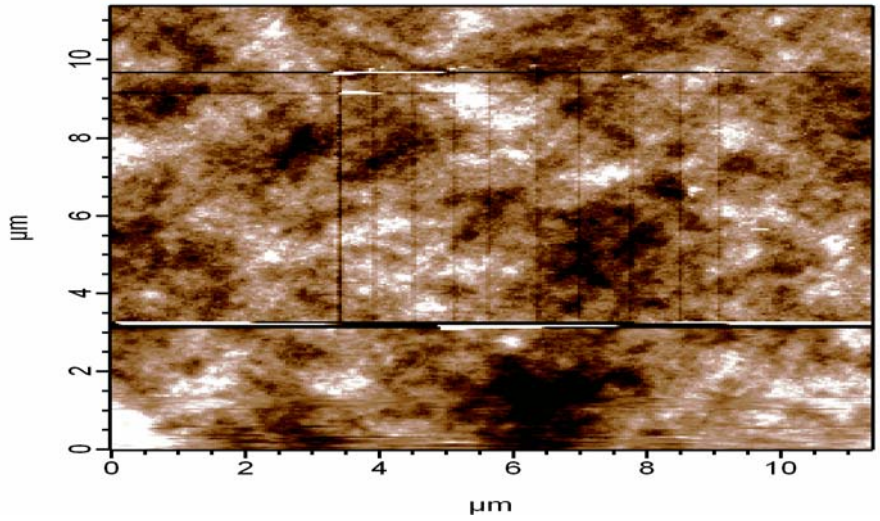

.

Figure 9.4. Height image of patterned area after gold(I) reduction. (by Nurxat)

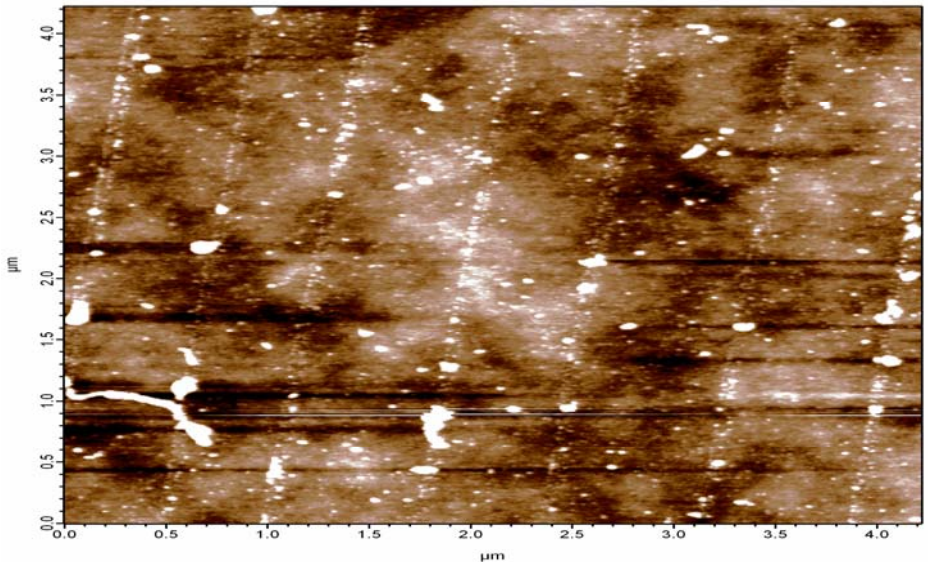

Although we successfully generated the gold arrays on the silicon wafer using nano-grafting method, we experienced the difficulties in the following aspects. For example, silicon nitride-coated layer of AFM tip was easily ruined due to the hardness of silicon substrate. For these reasons, we changed to gold substrate from silicon wafer for demonstrating the gold array formation using bio-mineralization method. Compared to the silicon substrate, the thiol monolayer of gold substrate was easily formed, not multilayer. The youngs modulus of gold is lower than that of silicon, so the regular silicon tips can be used for longer time for trench-making purposes. Also, most of thiol-functionalized molecules are commercially available.

3) **Nano-grafting method for gold substrate**

The gold substrate was incubated overnight in 1mM $SHC_{11}H_{22}$ $(CH_2CH_2O)_3OH$. To avoid the formation of langmuir- Blodgett on gold substrate during removal from

the solution, ten-fold 100% ethanol was added to the incubation vial and the substrate was removed quickly. Then gold substrate was dipped in three successive vials containing pure ethanol. The substrate was dried with nitrogen gas blow, and silicon chip was used to make patterned trenches on the SAM formed on the substrate using nano-litho program. The patterned substrate was incubated in 1mM 16-mercaptohexadeconic acid for 12 hrs for formation of a monolayer of mercaptohexadecanoic acid in the trenches. The acid groups in the patterned areas reacted with amine group of the peptide following the formation of intermediate between carboxyl groups and EDC/NHS. The intermediates in the areas other than the patterned trenches, including EDC in the solution, were deactivated with 10mM ethanol amine. The final substrate was treated with gold salt and a reducing agent. In this procedure, the final treatment was divided into two parts. In first case, the substrate was incubated in 0.1mM $HAuCl_4$ for 24 hours. After the incubation period was over, the substrate was rinsed with *nanowater*, and was incubated in sodium borohydrate with a final concentration of 0.01% for 2 hours. Last, the substrate was rinsed with *nanowater* and observed with Tapping mode AFM for the growth of gold nano-particles(scheme 9.3). In the second case, the gold substrate was incubated in a tris buffer solution containing organic gold salt ($AuP(CH_3)_3Cl$) for 2 days and the reducing agent was Hydrazine Hydrate.

In order to tune the distance between the nano-particles, we should isolate 16-mercaptohexadecanoic acid molecules from one another, which are linked to the bio-mineralizing peptides. The bio-mineralizing peptides have functions in growing nanoparticles on the substrate. The molecules used as spacers for isolating 16-

mercatohexadecanoic acid should have compatibility with 16-mercatohexadecanoic acid. Also, the molecule should be inert to peptides, which means that peptides should not be adsorbed on the spacers, and they should have a chemical structure similar to 16-mercaptohexadecanoic acid.

Scheme 9.3 Gold array formation on gold substrate using Nanolithography and Biomineralization.

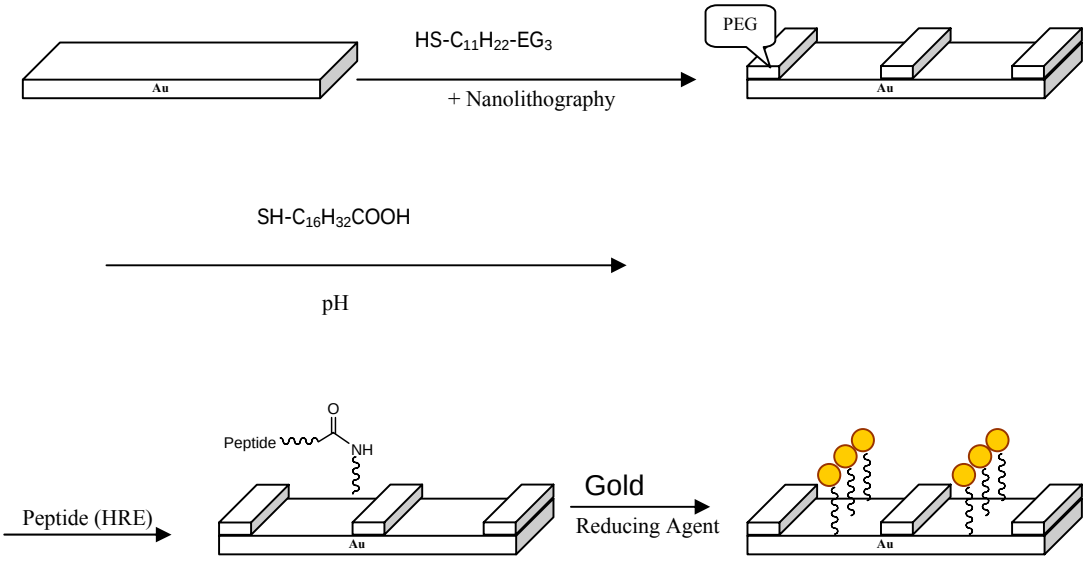

For the inorganic gold salt case, shown in Figure 9.5(A), 150nm wide trenches were created on the SAM surface. After the gold ion was reduced by sodium borohydrate, three visible gold arrays formed along the trench. In order to confirm the formation of the gold arrays, we performed another experiment. Trenches with 80nm width and 2.5nm depth were made on PEG coated gold surface. After the peptides were immobilized in the trenches, the gold surface was observed with SEM (Figure 9.6). The trenches are visible as dark lines due to the low electron density of peptides. However, the two gold arrays formed on the trenches became more visible as shown

in Figure 9.7; this is due to higher electron density compared to the trenches containing only peptides. This also provides evidence of gold particle formation

Figure 9.5 (A) Height image of trenches before reduction of gold ions. Width of trench: 150nm. (B) Height image of gold nano-particle growth in the trench. (by Nurxat & Samia)

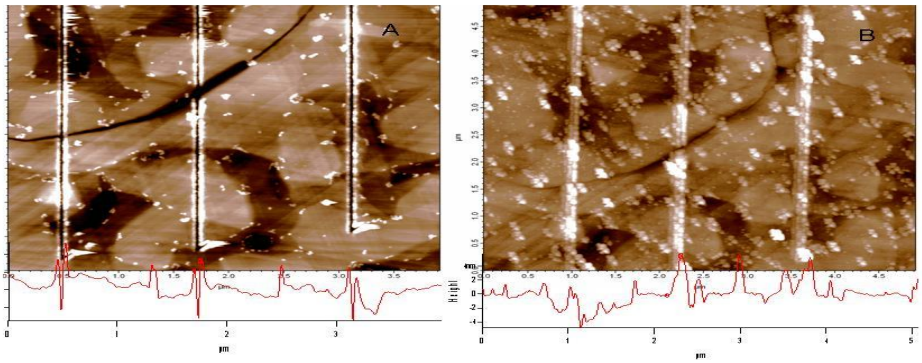

Figure 9.6 SEM image of trenches on the gold surface after the peptide immobilization. (Nurxat, Linglu & Kai)

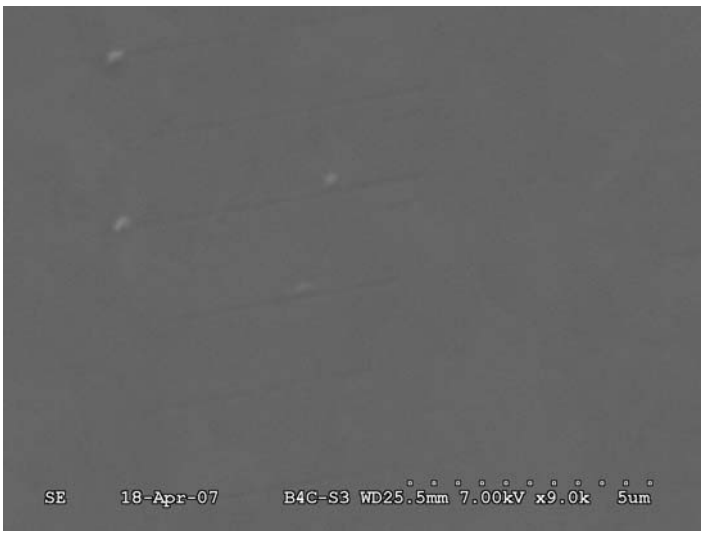

Figure 9.7 Gold array formation on the patterned area after the gold solution was reduced by sodium borohydrate (Nurxat, Linglu, & Kai)

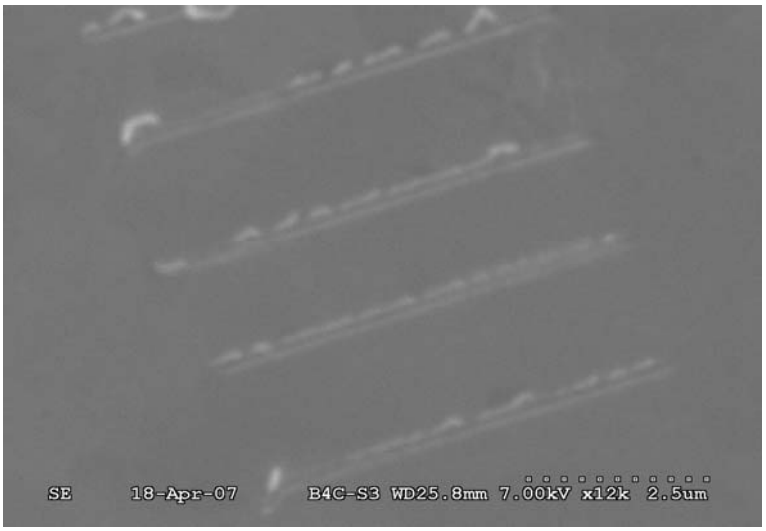

From figure 9.5 (a) and (b), it can be seen that despite incubation in peptides solution, the trenches do not have any height increase (Figure 9.5 (a)). However, after gold ions were reduced, the trenches were filled up with nanoparticle arrays (Figure 9.5(b)). Also, the trenches had more tightly packed nano-particles compared to other areas. This result indicates that biomineralizing peptides play certain function in growing gold nanoparticles. To further confirm the peptide function in growing gold nanoparticles, a control experiment was performed. In this procedure, we incubated the substrate with trenches containing monolayers of 16-mercaptohexadecanoic acid in gold salt solution in the absence of the peptides altogether. Without changing the other steps in scheme 3, in Figure 9.8(A) and (B), no gold particles formed in the trenches.

In order to tune the distance of gold nano-particles, we used $SHC_{11}H_{22}(CH_2CH_2O)_3OH$ as spacers. The following ratio between 16-

mercaptohexadecanic acid and $SHC_{11}H_{22}(CH_2CH_2O)_3OH$ (2:8, 1:9, 5:95, 1:99, 0.5:99.5) was prepared to control the distance between gold nano-particles. The results from the ratio of 16-mercaptohexadecanoic acid to $SHC_{11}H_{22}(CH_2CH_2O)_3OH$(1:9) and (2:8) showed the same result as the result without any spacers. From figure 9.9, it can be seen that as the ratio between 16-mercaptohexadecanic acid and $SHC_{11}H_{22}(CH_2CH_2O)_3OH$ was lowered to 5:95, the particles in the trenches became more diluted. When the ratio was lowered to 1:99, the particle growth was sparse forming no arrays (figure 9.10).

Figure 9.8 (a) Amplitude image of the patterned trench area after formation of mercaptohexadecanoic acid in the trenches. (b) Amplitude image of patterned areas after reduction of gold ion in the absence of HRE. (by Nurxat & Samia)

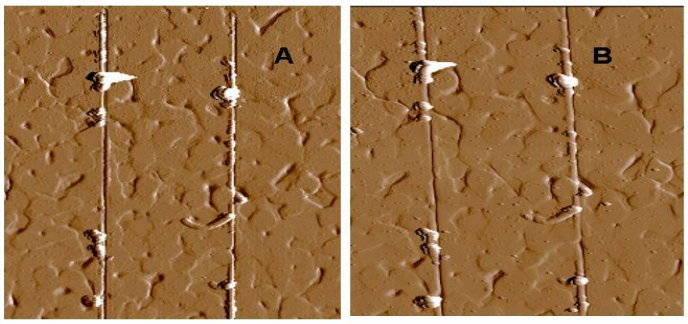

Figure 9.9 (a) Height image of patterned trench area before gold reduction (b) Height image of patterned trench area after gold reduction. The ration: 5:95. (by Nurxat & Samia)

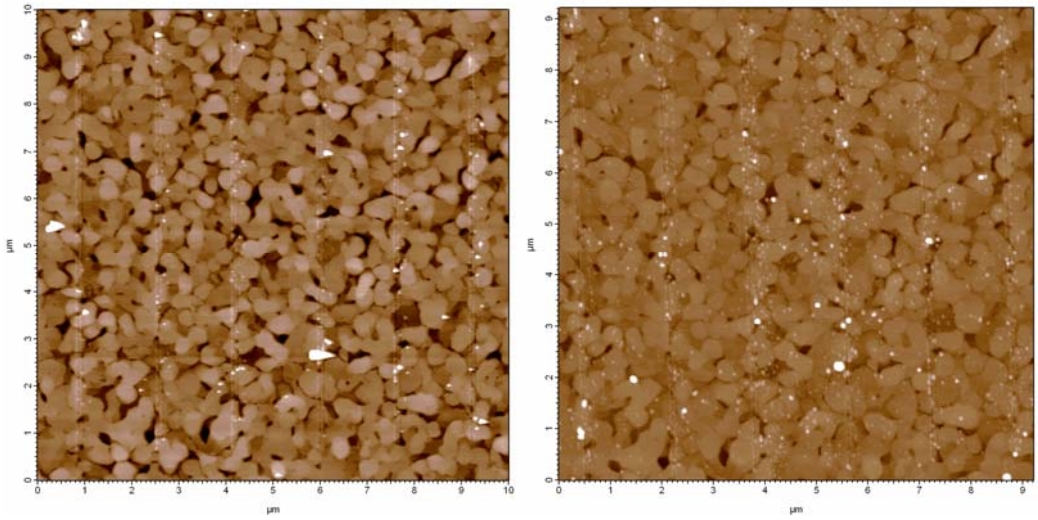

(a) (b)

Figure 9.10 (a) Height image of patterned trench area before gold reduction (b) Height image of patterned trench area after gold reduction. The ratio between 16-mercaptohexadecanic acid and $SHC_{11}H_{22}(CH_2CH_2O)_3OH$: 1:99.
(by Nurxat & Samia)

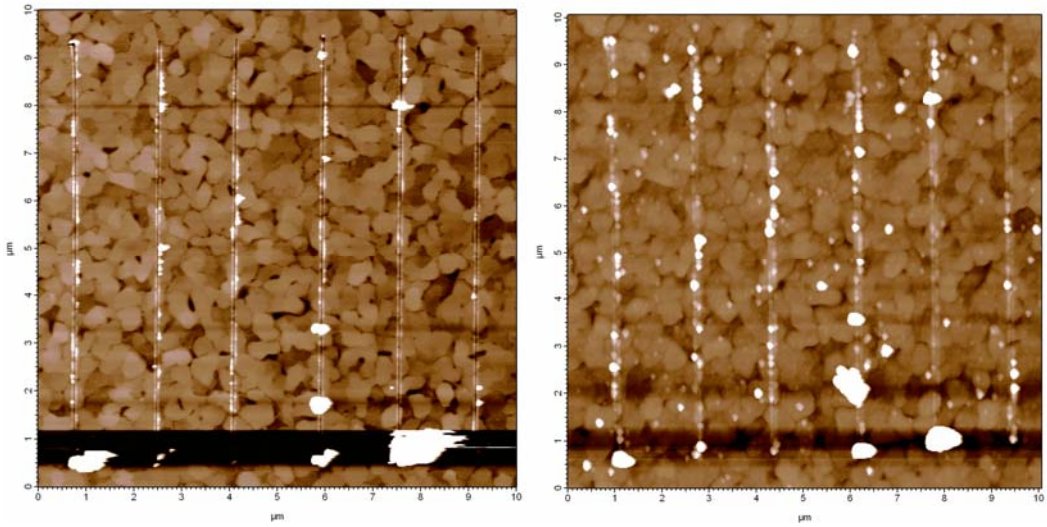

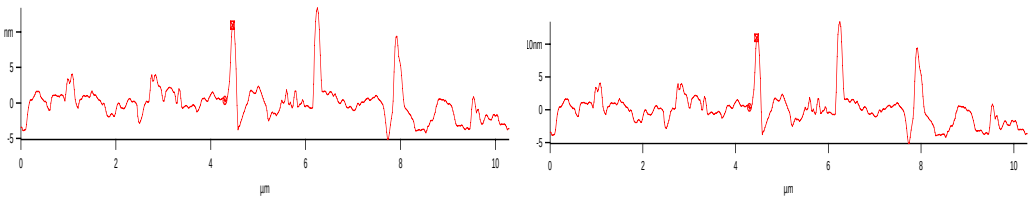

(a) (b)

Though the ratio makes the particle arrays more diluted, the particles arrays were not well packed. This explains that $SHC_{11}H_{22}(CH_2CH_2O)_3OH$ was not a good spacer for our system. All of the ratios (5:95, 1:99, 0.95: 99.5) give us the same results. After considering the difference in the chemical structures of the above two molecules, 16-mercaptohexadecane was chosen as an alternate spacer for our system (figure 9.11). However, the resulting gold substrate became dirtier. This is probably because alkane thiol is not bioresistive, or it absorbs more peptides; also alkane thiol could replace the bioresistive layer of ($SHC_{11}H_{22}(CH_2CH_2O)_3OH$) on the surface.

Figure 9.11 (a) height image of formation of gold nanoparticles in the trenches (b) amplitude image of formation of gold nanoparticles in the trenches. (by Nurxat & Samia)

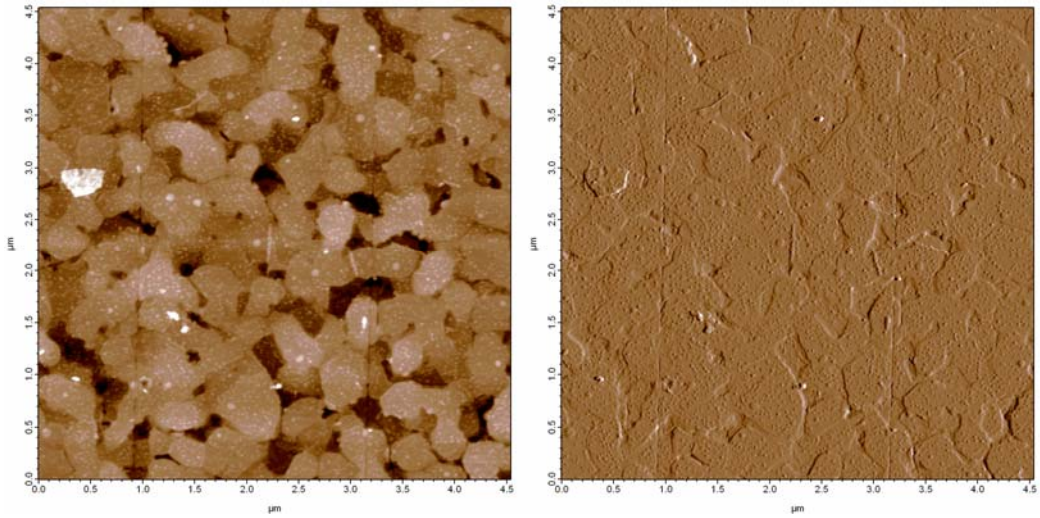

(a) (b)

We studied the correlation of the formation of particle arrays with the width of the trenches. Three different kinds of trenches were made. They were respectively as follows: First: 80nm-100nm, Second: 150nm-170nm, third: 340nm-360nm.

When the concentration of the reducing agent was 0.01% $NaBH_4$ and the gold ion concentration ($HAuCl_4$) was 0.1mM, the size of the formed gold nano-particle was around 6nm as shown in Figure 9.12. This was consistent with the height of the nano-particles on the gold substrate, not with the width of gold nano-particles from Height Image (AFM). The width of gold nano-particles on the gold surface from section analysis was 60nm. This is a well known phenomena in AFM image that the width of a height image is not reliable. However, this can be evaluated when the same materials and the same set up for AFM operation were performed. In Figure 9.13 A-1, A-2, B-1 and B-2, when the width of the trenches was around 90nm, the only two arrays were aligned. From the analysis of the width of one particle (60nm) from section analysis of height image of particles on the gold surface, at maximum, the two particles were fit in the 90nm wide trench. When the width of trenches increased to 150nm, the maximum number of particles should be three. From the Figure 9.13 D-2, we clearly see the three particles arrays along the trench. As the width of trenches increased to around 340nm, the figure 9.13 F-2 shows the six arrays along the trench. It can be concluded that the width of the trenches is related to the number of arrays generated along the trenches.

The gold ion in the organic gold salt is Au^{+} and this is different from Au^{3+} gold in the inorganic gold salt. The whole procedure of fabrication of gold array was the same except the last two steps. i.e. the inorganic gold was replaced by Trimethylphosphine Gold chloride. The reducing agent used was Hydrazine hydrate.

Figure 9.14 shows, when the width of the trenches were 170nm, the gold nano-particle array along the trench was three and consistent with the results, in which inorganic gold salt was applied. This is the reason why the size of the nano-particle (6nm) grown by the condition that used organic salt and hydrazine hydrate[148] is also the same as the gold particle size when inorganic salt is used. Due to limited facilities, we did not clearly observe the accurate width of trenches and nanoparticles.

Figure 9.12 TEM image of nano-particles at fixed concentration of $HAuCl_4$(III)(0.1mM) and $NaBH_4$(0.01%). (by Samia)

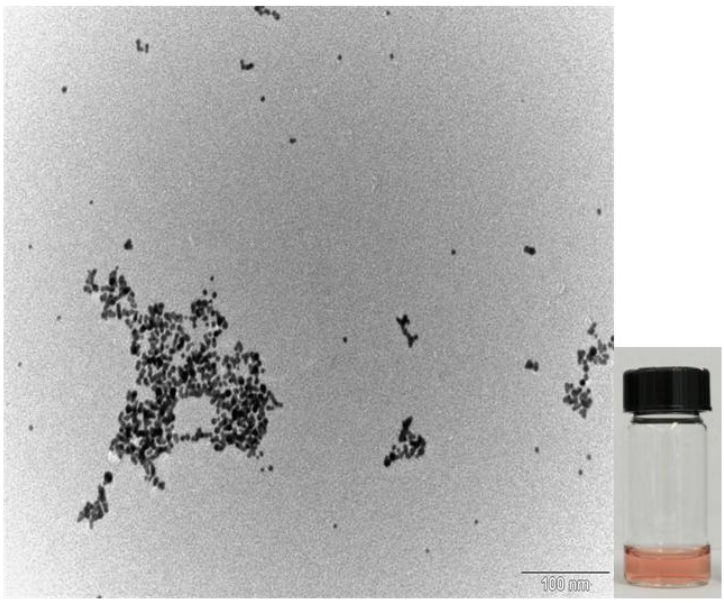

Figure 9.13 A-1 (Far-site view) Height image of trenches with width of 90nm , A-2 (near-site view) Height image of one trench from A-1, B-1 (Far-site view) Height image of trenches after gold reduction, B-2 (Near-site view) Height image of the one trench from B-1, C-1 (Far-site view) Height image of trenches with width of 150nm, C-2 (Near-site view) Height image of one trench from (C-1).D-1(Far-site view) Height image of trenches after gold reduction, D-2 (Near-site view) Height image of the one trench from D-1. E-1 (Far-site view) Height image of trenches with width of 340 nm , E-2 (near-site view) Height image of one trench from E-1, F-1 (Far-site view) Height image of trenches after gold reduction, F-2 (Near-site view) Height image of the one trench from F-1. (Nurxat & Samia)

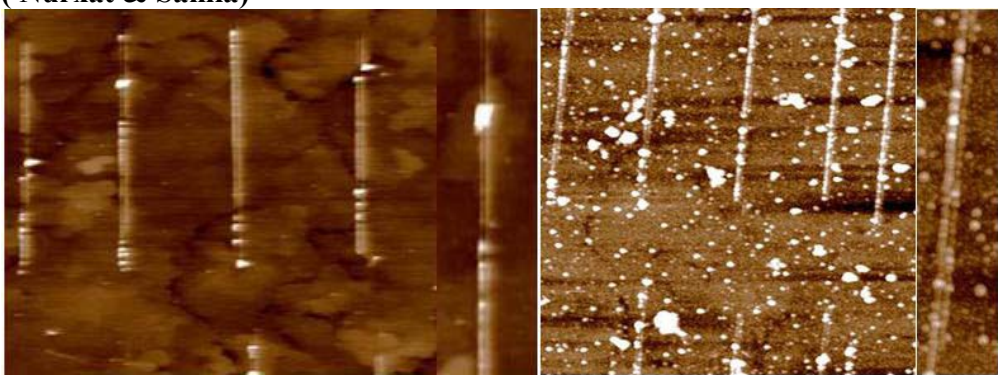

(A-1) (A-2) (B-1) (B-2)

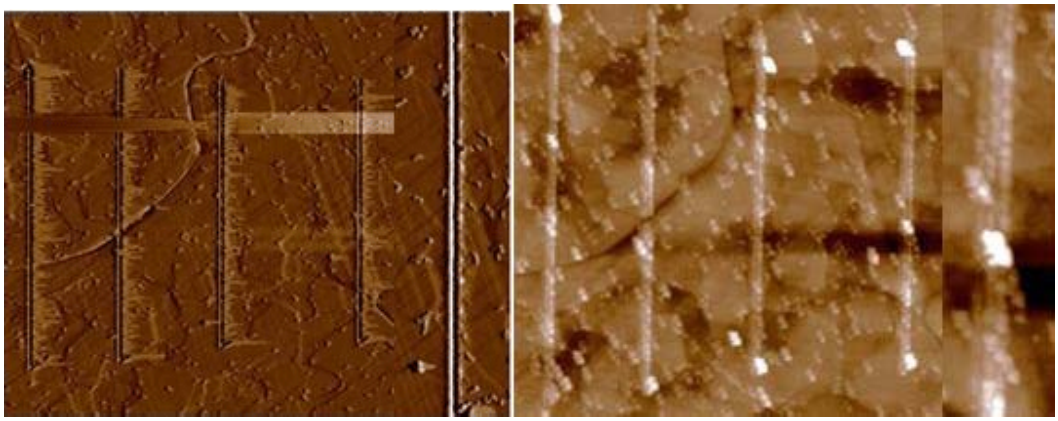

(C-1) (C-2) (D-1) (D-2)

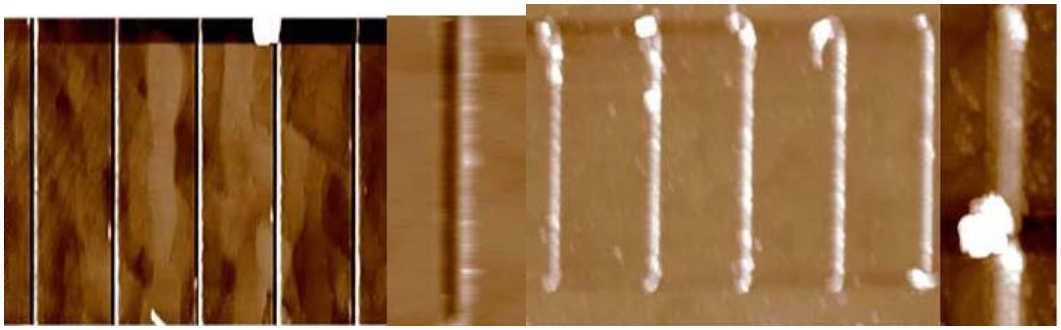

(E-1) (E-2) (F-1) (F-2)

Figure 9.14 Left image: Amplitude image of trenches before the formation gold NP formation. Right image: Amplitude image of gold NPs in the trenches.(by Nurxat & Samia)

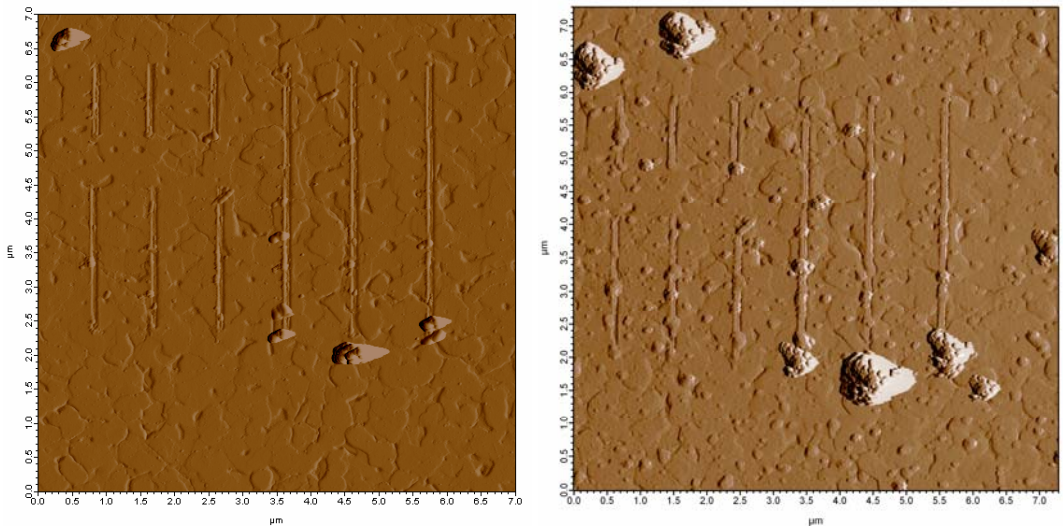

9.4 Conclusion

In conclusion, we successfully demonstrated the direct growth of gold nanoparticle in the liquid / sold interface using bio-mineralization after the bio-mineralizing peptides were immobilized on the gold surface. The resolution pattern was determined by the local geometry of AFM tip. The number of patterned nanoparticle arrays was controlled by the width of the trenches. The direct fabrication of gold patterns provides a pave to simplify the complicated process of logic gate using bottom-up approach. Combination of biomineralization and nanolithography method has an advantage to create any kind of logic gate and photonic device including semiconducting nanomaterials.

PART III Viral Sensor Development

Chapter 10

Comparison of Electrical Properties of Viruses Studied by AC Capacitance Scanning Probe Microscop[232]

10.1 Introduction

Electrical properties of biological cells have attracted broad interest from fundamental to applied sciences. For example, dielectric constants of cells could be influenced by locations and distributions of peptides, DNAs, and RNAs due to their individual dielectric response to AC frequency. These characteristic electronic structures of cells have been applied for their assay, separation, imaging, and quantification.[233-240] Recently, AC capacitance and impedance measurements have attracted interest for the applications in biomolecular systems since they do not require extra complex sample preparation procedures such as staining and manipulation of cells.[241] Because external AC fields can also trap a single cell by dielectrophoresis, the detection of cells with an extreme low detection limit could be achieved by monitoring impedance or capacitance changes before and after the cell binding event on electrodes.[242, 243]Therefore, it is advantageous to apply AC capacitance measurements for biological cell detection since AC fields probe the polarization responses of low dielectric materials that possess relatively high resistance, and it is quite logical to probe electric properties of biological cells by capacitance since they are not highly conductive.

While the dielectric properties of cells have been investigated extensively, the dielectric properties of viruses have not been characterized yet even though pathogen identification is of continued importance in the area of medical diagnostics and biological warfare defense. The conventional detection of viruses at the nanoscale is more difficult compared to the detection of cells at microscale in their low concentration due to their sizes. However, AC capacitance detection with atomic force microscope (AFM) could have an advantage for smaller virus detection. When a Pt-coated tip of AFM is applied as a nanometer-sized electrode and a virus particle is located between the AFM tip and bottom electrodes, the impedance and the capacitance of viruses can be measured as AC fields are applied between electrodes. AC capacitance scanning probe microscopy (AC-SPM) was recently applied for characterization of various semiconductors and polymers with the spacial resolution in nanometers.[244-246]Recently, a nanoscale electrochemical probe was also demonstrated to probe electron transfers and ion flux mechanisms by penetrating cell membranes,[247] however biological samples at the nanoscale have not explored by this technique extensively. Many viruses have a structure consisting of an envelope as a shell, DNAs/RNAs in a core, and a capsid layer between the core and the envelope (Figure 10.1). Each virus has distinct capsid proteins and glycoproteins, which are distributed at specific positions throughout the capsid and the envelope. If the dielectric properties of those characteristic proteins affect the overall dielectric constants of viruses significantly, each virus may possess distinct capacitance. Under this hypothesis, we examined seven different viruses using AC-SPM. In this report, capacitances were measured at high AC frequency to avoid complex ionic effects that could influence virus capacitance measurements due to the charge-screening at

electrode-fluid interfaces when capacitances are measured in solution.[241] AC-SPM probed that those viruses have distinct capacitances respectively and modification of the envelope and the capsid of the same virus strain altered their capacitances. Since proteins in the envelope and the capsid were observed to have a significant contribution to the overall capacitances of viruses, this technique has the potential to be developed as virus detection and identification platforms through the analysis of their distinct capacitance spectra.

10.2 EXPERIMENTAL

10.2.1 Materials

Polystyrene nanoparticles (Polysciences, Warrington, PA, USA) and polymethylmethacrylate nanoparticles (Bangs Labs, Fishers, IN) in the diameter of 100 nm were used as a standard for viral capacitance measurements. All purchased particles were diluted to 107 particles/mL, based on the manufacturer's specifications of initial particle concentration in particles/mL. Serial dilutions to the final concentration of 107 particles/mL were performed, however ultimately the precise concentration of particles in the final solution was not known. In the preparation of viral samples, the precise concentration was not required to be known when one was interested in measuring capacitances of the discretely deposited particles on a substrate since there were broad ranges of concentration for which deposition of nanoparticles on surfaces created suitable samples for AFM analysis of single nanoparticle. Then, 10μL of solution was dropped on gold substrates (Asylum

Research, Santa Barbara, CA, USA), working as another electrode. For each polymer nanoparticle in figures, at least fifty particles locating different spots were chosen to measure their capacitances. During the study different conductive tips were used on different days and different sample preps. The collected capacitance spectra were averaged and plotted against the AC frequency with error bars. Adenovirus type 5 (AV5) was used as received from American Type Cell Culture (VR-1516). Titered stocks of simian virus 40 (SV40) and vaccinia (MVA) were obtained from Drs. Zhiping Ye, and Michael Merchlinsky (all at FDA/CBER), respectively. HSV1, HSV2, and HSV1 GFP mutants were graciously donated from Dr. Andrea Bertke (FDA/CBER). CPMV virus was donated from Prof. John Johnson and used as received. Most of viruses examined in this report were spherical while MVA was the only virus whose shape was oval, and these viruses had the height of 20 ± 3 nm due to collapsing on the substrate based on their AFM images (Figure 10.2). The size of each virus was 75 ± 10 nm for AV5, 55 ± 3 nm for SV40, 270 ± 20 nm x 180 ± 30 nm for MVA, 170 ± 20 nm for HSV, and 25 ± 3 nm for CPMV, respectively. To create a series of spiked samples for analysis, 10-fold serial dilutions with distilled water were performed from virus stocks with known concentrations. The envelopes of the HSV2 virons were removed by a Freon extraction. Freon was used as received from Fisher, and added to a virus stock solution in a 1:1 volume: volume ratio. The mixture was vortexed for 30 seconds, and then centrifuged at 14k rpm for 30 seconds. Then the aqueous layer containing the virus with no envelopes was collected.

10.2.2 Impedance/ Capacitance measurements of polymer and virus Particles

To develop a suitable interface between the AFM and the impedance analyzer that would not compromise extreme sensitivity requirements, a stand-alone MFP-3D AFM (Asylum Research, Santa Barbara, CA, USA) was outfitted with custom modifications. Platinum coated tips with a radius of curvature of less than 40nm and spring constant near 40 N/m were used for topological AFM imaging and electrical measurements (Mikromasch NSC15-Ti/Pt, Wilsonville, OR, USA; Nanosensors PPP-NCHPt, NanoAndMoreUSA, Lady's Island, SC, USA). Non-contact mode images were collected to find particles of interest while minimizing tip wear and extending lifetime of the Pt coating on the AFM tips. The tip end was 6 positioned precisely at the center of virus and nanoparticle using computer-controlled closed-loop scanner. A constant force of 10 - 500 nN was applied throughout all capacitance measurements. Humidity was controlled for all AC-SPM experiments by monitoring the humidity inside the acoustic isolation hood chamber. To control humidity levels between 10% and 90%, an ultrasonic humidifier was fitted with a connection to plumb a pipe into the acoustic AFM hood such that water vapor could be flowed into the acoustic hood chamber and increase the humidity. The samples were left in acoustic isolation hood chamber at constant temperature and humidity overnight to reach equilibrium. A Solartron 1260 Frequency Response Analyzer with a Solartron 1296 Dielectric Interface (AMETEK, Paoli, PA, USA) was used for the collection of impedance and capacitance spectra. The capacitance values were obtained after the data fitting of the measured impedance data whose circuit model is given in Figure 10.3. This circuit

model was determined from control experiments of the model nanoparticles with the AC-SPM instrument. Briefly, the fitting to the equation in series with virus capacitance, cable inductance, and other frequency-dependent capacitance contributed from conductive AFM cantilever, air, leakage current, and loss parameter, determined constants in the frequencydependent capacitance part of the instrument, CPE (constant-phase element), and the completed equation was applied to obtain the virus capacitances from their impedance spectra. An applied AC bias of 10mV was used to stay below the Johnson noise at room temperature of 26mV, thereby minimizing electrical perturbations to the materials in the system. The impedance measurement was integrated over 10 seconds for each frequency below 100Hz, in an attempt to average out low frequency noise sources from building vibrations and AC power lines. The impedance measurement was integrated for 1 second at each frequency at and above 100Hz.

10.3 RESULTS AND DISCUSSION

After a non-contact mode image was collected to find isolated virus particles on Au substrates (Figure 10.2), the AFM tip was moved to the center of a virus particle precisely through the closed-loop scanner. A constant tip force of 100 nN was applied to each virus in order to maintain the sufficient and consistent contact between AFM tip and virus. Before and after carrying out capacitance measurements, the system conductance was checked by measuring impedances of bare Au plates. We first analyzed the dielectric properties of polymer nanoparticles as a function of AC frequency to study a circuit model of our system (Figure 10.3). Capacitances of

polystyrene (PS) and polymethylmethacrylate (PMMA) particles in the diameter of 100 nm were also compared at 90 % of humidity as controls, and the capacitance of PMMA appeared higher than the PS capacitance as shown in Figure 10.4-(a), which is consistent with the order of their dielectric constants, 2.6 and 3.12, respectively.[248] Figure 10.4-(b) shows capacitances of five types of viruses; adenovirus type 5 (AV 5), herpes simplex virus type 1 (HSV1), simian virus 40 (SV40), vaccinia (MVA), and cowpea mosaic virus (CPMV). Their impedance signals were averaged 1-10 seconds for each AC frequency at 10 mV of AC bias. For each type of virus, fifty different particles were measured and collected capacitance spectra were averaged with error bars and normalized by the size of each virus, as shown in Figure 10.4-(b). In this figure, SV40 showed the highest capacitance while AV5 had the lowest. This plot indicates that those viruses could be clearly distinguished by measuring their capacitance spectra. It should be noted that there was no change in capacitance of the viruses regardless of the tip forces within the range of 50 nN ~ 500 nN (Figure 10.4-(c)). We were aware that the water condensation between AFM tip and virus could affect our capacitance measurements since the pervious dielectric study of B-normal white blood cells showed that the dielectric permittivity of water was comparable to the ones for nuclear envelope, nucleoplasm, and cytoplasm of the human cells.[249] To examine the influence of the water condensation between the tip and virus, the capacitance of the virus was measured at humidity levels between 10% and 90%, as shown in Figure 10.4-(d). In this figure, there was no change in the virus capacitance regardless of the degree of humidity. This outcome indicates that the water condensation had little effect on virus capacitance measurements. We would also like

to note that the water bridge contributes less to the overall capacitance measurement in the higher frequency range between 102 and 104 Hz. The influence of solvents surrounding the sample to the capacitance value is considerable at the lower AC frequency due to the ionic motions in the surrounding media. In all measured capacitance spectra the noise caused by the ionic motions was significantly reduced above 102 Hz. Thus, by monitoring the 8 virus capacitance in the higher frequency range where the ionic motion was reduced, the effect of the water condensation could be minimized in the capacitance measurement of viruses, as shown in Figure 10.4. This observation supports the validity of virus capacitance data measured in the range of 102~104 Hz; In this range the signal noise was small enough not to influence on the capacitance of viruses, which made the AC-SPM capacitance reliable as characteristic markers for the virus diagnosis. Viruses can be modeled as spheres consisting of electrolytic media surrounded by isolating shells. In the frame of this simplified model, envelopes and capsids of viruses behave as insulating layers (Figure 10.1), and the polarization on those layers significantly influences overall viral capacitance as a function of AC frequency.[250] At low frequencies, the envelopes and the capsids offer significant barriers to current flow and the virus can be treated as an isolating particle. Herein, changes in the capacitance are only related to the size of the particle. At intermediate frequencies, the polarization of envelopes and capsids decreases and the dielectric properties of these layers govern the capacitance of viruses. At high frequencies, the envelopes and the capsids are minimally polarized and the capacitance measurements provide information about the viral core (Figure 10.1). Based on this model, we hypothesize that the origin of the capacitance

difference among viruses in our measurements arises from differences between the dielectric properties of characteristic glycoproteins in their envelopes and capsid proteins in their capsids since we measured viral capacitances in the intermediate frequency range. Unfortunately, exact dielectric constants and distributions of the specific proteins in these viruses are not well characterized, and therefore overall dielectric constants of those viruses cannot be directly compared with our observation in Figure 10.4-(b) to confirm our hypothesis. However, the dielectric variations of viruses could be inferred from the differences of capacitance values between wild-type and modified viruses; glycoproteins can be modified by mutation or capsid proteins can be removed chemically. Here we designed two control experiments to probe whether capacitance measurements are sensitive to proteins in the capsid and the envelope, respectively. First, HSV1 was mutated to add green fluorescence proteins (GFP) in their capsid and compared it with the wild type of HSV1. As shown in Figure 10.5-(a), GFP-mutated HSV1 has a higher capacitance as compared to the wild type HSV1. The GFP, whose isoelelctric point is 5.5, charges negatively in neutral pH and physiological pH buffers,[251] and this dielectric difference in the capsid shifts the capacitance of GFP-mutated HSV1 higher than the capacitance of wild type HSV1. As the second control experiment to probe the effect of glycoproteins in the envelopes on virus capacitances, we extracted envelopes of HSV2 chemically using the Freon extraction method and compared capacitances between the envelope-extracted HSV2 and the wild type HSV2. As the envelope of HSV2 was removed, the capacitance decreased, as shown in Figure 10.5-(b). Since viruses of the same viral strain have the same dimension and inner content, the observed changes in

capacitance are related to the dielectric properties of the viral envelopes and capsids. Thus, these results indicate that proteins in the envelope and the capsids contribute significantly to the overall dielectric constant of HSV at the intermediate frequencies. Moreover, it indicates that our capacitance measurements were performed at the proper frequency range, thus validating the proposed methodology for detecting viruses via their characteristic envelope/capsid compositions. It should be noted that the previous study on dielectric properties for various populations of white blood cells also supports our hypothesis about the origin of the characteristic capacitance responses for different viruses.[249] In this work, dielectric permittivity, capacitance, and conductivity of the human cells were broken down into each component such as membrane (1st shell), cytoplasm, nuclear envelope (2nd shell), and nucleoplasm with the double-shell dielectric model. Although this work studied dielectric permittivity, capacitance, and conductivity of the human cells, the viral structure also consists of two shells, envelope and capsid, and their outcome was consistent with our viral results in capacitance values. However, even more significant consistency is that conductivities and capacitances for two shells of those cells, membranes and nuclear envelopes, were highly characteristic to the types of cells. Since we also found in the case of viruses that proteins in two viral shells, envelopes and capsids, had significant effect on the overall capacitance of viruses as shown in Figure 10.5, the offsets of capacitance values in different viral systems in Figure 10.4-(b) also likely appeared by the characteristic capacitance differences in envelopes and capsids among viruses.

10.4 CONCLUSION

AC capacitance scanning probe microscopy probed that five viruses, AV5, CPMV, MVA, SV40, and HSV1 possessed distinguishable and characteristic capacitances. A mutation on the capsid in HSV1 virus with green fluorescence proteins (GFP) increased capacitance from 9x10-6 F/cm2 to 1x10-5 F/cm2 at 104 Hz. HSV2 virus decreased capacitance when its envelope and glycoproteins were chemically extracted. These control experiments indicate that dielectric properties of capsid proteins and glycoproteins significantly influence the observed overall capacitances of viruses. Because those capsid proteins and glycoproteins are characteristic to the viral type, this AC-SPM technique could be applied to detect and identify viruses at the single viron level using their distinct capacitance spectra as fingerprints without labeling.

Figure 10.1. Representative illustration of the typical structure of viruses examined in this report. It shows that two shells, envelopes and capsids, surround the core containing nucleic acids.

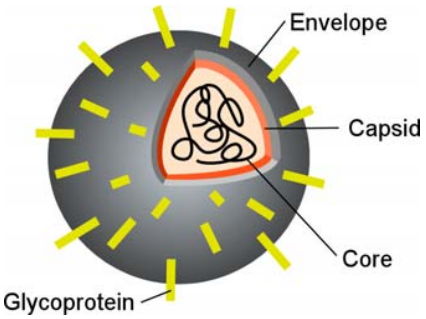

Figure 10.2 Representative AFM images of (a) HSV1 and (b) MVA. Most of viruses examined in this report are spherical as shown in (a) while MVA is the only virus whose shape is oval as shown in (b). (by Nurxat)

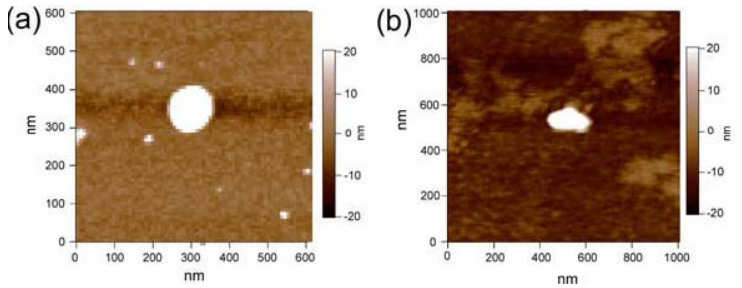

Figure 10.3 Illustration of the probe configuration and its circuit model of the AC capacitance SPM. C_{virus} is capacitance of virus, CPE is a constant-phase element, representing frequency-dependent capacitance and resistance of AFM tip and air, and R_{inst} is resistance of the instrument.

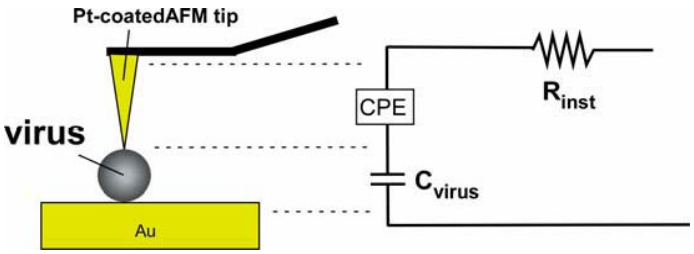

Figure 10.4 Capacitance spectra of (a) polystyrene (□) and PMMA (▲) nanoparticles (b) Capacitance spectra of AV5, CPMV, MVA, SV40, and HSV1 (c) HSV1 with the tip forces, 50 nN (►), 200 nN (□), and 500 nN (○) (d) HSV1 at humidity level 10 % (△), 50 % (○), and 70 % (▼). (by Nurxat & Rob)

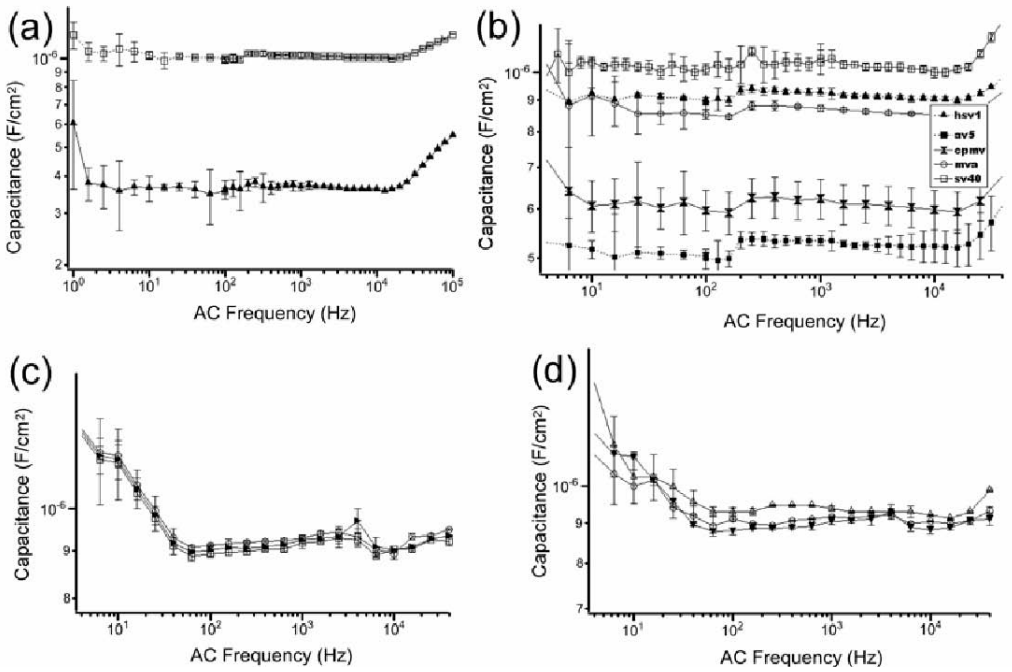

Figure 10.5 Capacitance spectra of (a) HSV1 (▼) and mutated HSV1 adding green fluorescence proteins in capsid (▽) (b) HSV2 (○) and envelope-extracted HSV2 (●). (by Rob, Sang & Anne)

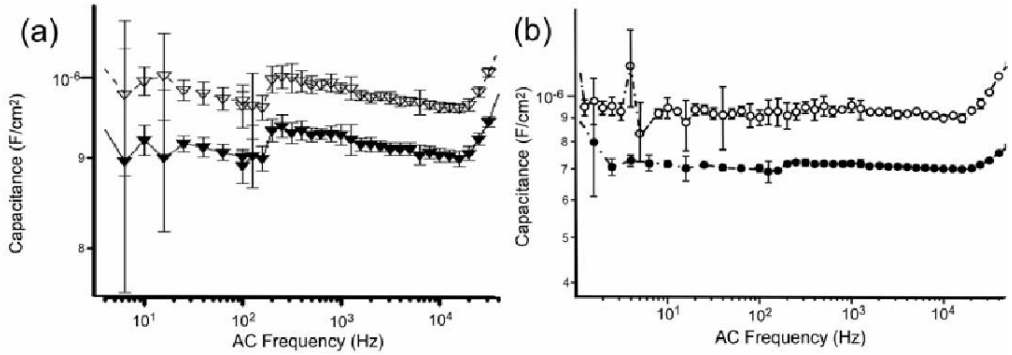

PART IV

Conclusions and Perspectives

In recent years, nanotechnology has been applied in many fields. The synthesis of new materials and the fabrication of nanodevice is the main trend in nanotechnology. This dissertation reports our discoveries on organic nanoswitches with fast response time, room temperature synthesis of Ferrolectric Barium titanate nanocrystals which cannot be formed at room temperature, and growth of silica nanoparticles in controlled shapes. Also, feasible bottom-up approachs were applied to build up the geometries of electronic circuit and photonic device. Furthermore, the antibody coated nanotubes as building blocks for electronic circuit were aligned antigen patterned region with antibody-antigen interaction. For insitu fabrication of nanodevice, the biomineralizing peptides were patterned according to the required geometry with scanning probe microscopy and directly mineralize certain metal ions to grow metal nanoparticles. These findings are based on the exploitation of surface physicochemical principles. An interfacial polymerization-crystallization system was used to prepare the first organic polymer single crystalline nanoneedles. Self-assembled bolaamphiphilic nano-reactors with unique chemical properties were applied as templates to fabricate at room temperature ferroelectric barium titanate nanocrystals (6 to 12 nm). The versatility and significance of systems involving surface of two simple liquids for the preparation of important elements for nanoelectronics was demonstrated. At present, our preliminary results showed that the growth of nano-particle arrays was consistent with the width of the trench.

A self-assembled bolaamphiphilic nanoreactor, which was proposed to fabricate ferroelectric barium titanate nanocrystals, from 6 to 12 nm, at room temperature, may have a broad impact in the growth of various important crystals that do not grow at room temperature and ambient pressure. Recent examples include a similar approach for the synthesis of gallium oxide nanostructures.[1] The advancement of this novel approach will continue to provide more important nanoelements with different functions. Also the insitu fabrication, which was demonstrated to grow nanogold arrays on the gold substrate, may be applied to grow semiconducting nanoparticles arrays with controlled distance and shape on the silicon chip.

PART V List of My Publication during Ph.D. Study

1) **Nurxat Nuraje**, Kai Su, Samia Mohammed, Hiroshi Matsui "Synthesis of semiconductor and metallic nanocrystals on the solid/Liquid interface using Biomineralization process" in preparation

2) Kai Su, **Nurxat Nuraje**, Hiroshi Matsuib, and Nan-Loh Yanga, "One–pot synthesis of strontium titanante/polyaniline nano-composites and their electrorheological effect" ***Chemistry of Materials(submitted)***

3)Kai Su, **Nurxat Nuraje**, and Nan-Loh Yang " An Open-Bench Method for the Preparation of BaTiO3,SrTiO3 and BaxSr1-xTiO3 nanocrystals at 80°C"***Langmuir23, 11369(2007)***

4) Robert I. MacCuspie, **Nurxat Nuraje**, Sang-Yup Lee, and Hiroshi Matsui " Comparison of Electrical properties of Various Viruses studied by AC Capacitance Scanning Probe Microscopy" ***Journal of American Chemical Society130, 887(2008)***

5) Linglu Yang, **Nurxat Nuraje**, Hanying Bai, and Hiroshi Matsui "Crossbar Assembly of Antobody-functionalized Peptide nanotubes via Biomimetic Molecular Recognition" ***Journal of Peptide science, ASAP***

6) **Nurxat Nuraje**, Su Kai, and Hiroshi Matsui "Catalytic growth of silica nanocrystals in controlled shapes at planar liquid/liquid interfaces" ***New journal of chemistry 31,1895(2007)***

7) **Nurxat Nuraje**, Su Kai, Nan-Loh Yang and Hiroshi Matsui "Growth of single crystalline nanoneedles of conducting polymers with fast conductance switching property from interfacial epitaxial polymerization" ***ACS nano, ASAP***

8) **Nurxat Nuraje**, Kai Su, Lingzhi Zhang, I-Wei Chu, Ralf M. Peetz, Hiroshi Matsui, and Nan-Loh Yang "Fast conductance switching in single-crystal organic nanoneedles prepared from an interfacial polymerization-crystallization of 3,4-ethylenedioxythiophene" ***Advanced Materials 19,669(2007)***

9) **Nurxat Nuraje**, Kai Su, Jacopo Samson, Ed Manning and Hiroshi Matsui "Room temperature synthesis of ferroelectric barium titanate nanoparticles using peptide nanorings as templates" ***Advanced Materials 18, 807 (2006)***

10) **Nurxat Nuraje**, Kai Su, Jacopo Samson, and Hiroshi Matsui "Self-assembly of Au Nanoparticle-containing Peptide Nanorings on Surfaces" ***Supramolecular Chemistry 18, 429 (2006)***

*** Top 10 most accessed articles of the journal in 2006**

11) I. A. Banerjee, L.Yu, R. MacCuspie, **N. Nuraje**, H. Matsui. "Protein Nanotube Device Fabrication: Smart Immbobilization and Metallization" ***Polymer Preprints 46(1), 80-81(2000)***

12) Xueyun Gao,Ramin Djalali, **Nurxat Nuraje**, and H.Matsui "Peptide Nanotubes: Simple Separation Using Size-Exclusion Columns and Use as Templates for Fabricating One-Dimensional Single Chains of Au Nanoparticles" ***Advanced Materials 17, 1753 (2005)***

13) L. Yu, I. A. Banerjee, **Nurxat Nuraje**, H. Matsui "Fabrication and application of enzyme-incorporated peptide nanotubes "**.** ***Bioconjugate Chemistry 16, 1484(2005)***

14) **Nurxat Nuraje**, Ipsita A. Banerjee, Robert I. MacCuspie, Lingtao Yu, and Hiroshi Matsui
"Biological Bottom-Up Assembly of Antibody Nanotubes on Patterned Antigen Arrays"
Journal of American Chemical Society *126,* 8088(2004)
*** the most accessed articles of Journal of American Chemical Society in the quarter of the july-september , 2007.**

PART V Bibliography

1. Nuraje, N.; Su, K.; Haboosheh, A.; Samson, J.; Manning, E. P.; Yang, N. L.; Matsui, H., Room temperature synthesis of ferroelectric barium titanate nanoparticles using peptide nanorings as templates. *Advanced Materials* **2006,** 18, (6), 807-+.
2. O'Brien, S.; Brus, L.; Murray, C. B., Synthesis of monodisperse nanoparticles of barium titanate: Toward a generalized strategy of oxide nanoparticle synthesis. *Journal of the American Chemical Society* **2001,** 123, (48), 12085-12086.
3. Urban, J. J.; Yun, W. S.; Gu, Q.; Park, H., Synthesis of single-crystalline perovskite nanorods composed of barium titanate and strontium titanate. *Journal of the American Chemical Society* **2002,** 124, (7), 1186-1187.
4. Yun, W. S.; Urban, J. J.; Gu, Q.; Park, H., Ferroelectric properties of individual barium titanate nanowires investigated by scanned probe Microscopy. *Nano Letters* **2002,** 2, (5), 447-450.
5. Ahn, C. H.; Rabe, K. M.; Triscone, J. M., Ferroelectricity at the nanoscale: Local polarization in oxide thin films and heterostructures. *Science* **2004,** 303, (5657), 488-491.
6. Fong, D. D.; Stephenson, G. B.; Streiffer, S. K.; Eastman, J. A.; Auciello, O.; Fuoss, P. H.; Thompson, C., Ferroelectricity in ultrathin perovskite films. *Science* **2004,** 304, (5677), 1650-1653.
7. Choi, K. J.; Biegalski, M.; Li, Y. L.; Sharan, A.; Schubert, J.; Uecker, R.; Reiche, P.; Chen, Y. B.; Pan, X. Q.; Gopalan, V.; Chen, L. Q.; Schlom, D. G.; Eom, C. B., Enhancement of ferroelectricity in strained BaTiO3 thin films. *Science* **2004,** 306, (5698), 1005-1009.
8. Shaw, T. M.; Trolier-McKinstry, S.; McIntyre, P. C., The properties of ferroelectric films at small dimensions. *Annual Review of Materials Science* **2000,** 30, 263-298.
9. Urban, J. J.; Spanier, J. E.; Lian, O. Y.; Yun, W. S.; Park, H., Single-crystalline barium titanate nanowires. *Advanced Materials* **2003,** 15, (5), 423-426.
10. Fu, H.; Bellaiche, L., Ferroelectricity in Barium Titanate Quantum Dots and Wires. *Physical Review Letters* **2003,** 91, (25), 257601.
11. Naumov, II; Bellaiche, L.; Fu, H. X., Unusual phase transitions in ferroelectric nanodisks and nanorods. *Nature* **2004,** 432, (7018), 737-740.
12. Clark, I. J.; Takeuchi, T.; Ohtori, N.; Sinclair, D. C., Hydrothermal synthesis and characterisation of BaTiO3 fine powders: precursors, polymorphism and properties. *Journal of Materials Chemistry* **1999,** 9, (1), 83-91.
13. Niederberger, M.; Garnweitner, G.; Pinna, N.; Antonietti, M., Nonaqueous and Halide-Free Route to Crystalline $BaTiO_3$, $SrTiO_3$, and $(Ba,Sr)TiO_3$ Nanoparticles via a Mechanism Involving C-C Bond Formation. *Journal of the American Chemical Society* **2004,** 126, (29), 9120-9126.
14. Mao, Y. B.; Banerjee, S.; Wong, S. S., Large-scale synthesis of single-crystal line perovskite nanostructures. *Journal of the American Chemical Society* **2003,** 125, (51), 15718-15719.

15. Luo, Y.; Szafraniak, I.; Zakharov, N. D.; Nagarajan, V.; Steinhart, M.; Wehrspohn, R. B.; Wendorff, J. H.; Ramesh, R.; Alexe, M., Nanoshell tubes of ferroelectric lead zirconate titanate and barium titanate. *Applied Physics Letters* **2003,** 83, (3), 440-442.
16. Cha, J. N.; Stucky, G. D.; Morse, D. E.; Deming, T. J., Biomimetic synthesis of ordered silica structures mediated by block copolypeptides. *Nature* **2000,** 403, (6767), 289-292.
17. Naik, R. R.; Stringer, S. J.; Agarwal, G.; Jones, S. E.; Stone, M. O., Biomimetic synthesis and patterning of silver nanoparticles. *Nature Materials* **2002,** 1, (3), 169-172.
18. Sarikaya, M.; Tamerler, C.; Jen, A. K. Y.; Schulten, K.; Baneyx, F., Molecular biomimetics: nanotechnology through biology. *Nature Materials* **2003,** 2, (9), 577-585.
19. Whitling, J. M.; Spreitzer, G.; Wright, D. W., A combinatorial and informatics approach to CdS nanoclusters. *Advanced Materials* **2000,** 12, (18), 1377-1380.
20. Reches, M.; Gazit, E., Casting metal nanowires within discrete self-assembled peptide nanotubes. *Science* **2003,** 300, (5619), 625-627.
21. Bansal, V.; Sanyal, A.; Rautaray, D.; Ahmad, A.; Sastry, M., Bioleaching of sand by the fungus Fusarium oxysporum as a means of producing extracellular silica nanoparticles. *Advanced Materials* **2005,** 17, (7), 889-+.
22. Walsh, D.; Arcelli, L.; Ikoma, T.; Tanaka, J.; Mann, S., Dextran templating for the synthesis of metallic and metal oxide sponges. *Nature Materials* **2003,** 2, (6), 386-U5.
23. Douglas, T.; Young, M., Virus particles as templates for materials synthesis. *Advanced Materials* **1999,** 11, (8), 679-+.
24. Loste, E.; Park, R. J.; Warren, J.; Meldrum, F. C., Precipitation of calcium carbonate in confinement. *Advanced Functional Materials* **2004,** 14, (12), 1211-1220.
25. Aizenberg, J.; Muller, D. A.; Grazul, J. L.; Hamann, D. R., Direct fabrication of large micropatterned single crystals. *Science* **2003,** 299, (5610), 1205-1208.
26. Yang, S.; Chen, G.; Megens, M.; Ullal, C. K.; Han, Y. J.; Rapaport, R.; Thomas, E. L.; Aizenberg, J., Functional biomimetic microlens arrays with integrated pores. *Advanced Materials* **2005,** 17, (4), 435-+.
27. Banerjee, I. A.; Yu, L. T.; Matsui, H., Cu nanocrystal growth on peptide nanotubes by biomineralization: Size control of Cu nanocrystals by tuning peptide conformation. *Proceedings of the National Academy of Sciences of the United States of America* **2003,** 100, (25), 14678-14682.
28. Matsui, H.; Gologan, B., Crystalline glycylglycine bolaamphiphile tubules and their pH-sensitive structural transformation. *Journal of Physical Chemistry B* **2000,** 104, (15), 3383-3386.
29. Kogiso, M.; Ohnishi, S.; Yase, K.; Masuda, M.; Shimizu, T., Dicarboxylic Oligopeptide Bolaamphiphiles: Proton-Triggered Self-Assembly of Microtubes with Loose Solid Surfaces. *Langmuir* **1998,** 14, (18), 4978-4986.
30. Djalali, R.; Samson, J.; Matsui, H., Doughnut-shaped peptide nano-assemblies and their applications as nanoreactors. *Journal of the American Chemical Society* **2004,** 126, (25), 7935-7939.

31. Dutta, P. K.; Gallagher, P. K.; Twu, J., Raman-Spectroscopic Study of the Formation of Barium-Titanate from an Oxalate Precursor. *Chemistry of Materials* **1993,** 5, (12), 1739-1743.
32. Lee, T.; Yao, N.; Imai, H.; Aksay, I. A., Barium titanate nanoparticles in block copolymer. *Langmuir* **2001,** 17, (24), 7656-7663.
33. Takeuchi, T.; Tabuchi, M.; Ado, K.; Honjo, K.; Nakamura, O.; Kageyama, H.; Suyama, Y.; Ohtori, N.; Nagasawa, M., Grain size dependence of dielectric properties of ultrafine BaTiO3 prepared by a sol-crystal method. *Journal of Materials Science* **1997,** 32, (15), 4053-4060.
34. Heim, T.; Lmimouni, K.; Vuillaume, D., Ambipolar charge injection and transport in a single pentacene monolayer island. *Nano Letters* **2004,** 4, (11), 2145-2150.
35. Aizenberg, J., Crystallization in Patterns: A Bio-Inspired Approach. *Advanced Materials* **2004,** 16, (15), 1295-1302.
36. Su, K.; Nuraje, N.; Yang, N. L., Open-Bench Method for the Preparation of BaTiO3, SrTiO3, and BaxSr1-xTiO3 Nanocrystals at 80^{o}C. *Langmuir* **2007,** 23, (23), 11369-11372.
37. Chandler, C. D.; Roger, C.; Hampden-Smith, M. J., Chemical aspects of solution routes to perovskite-phase mixed-metal oxides from metal-organic precursors. *Chem. Rev.* **1993,** 93, (3), 1205-1241.
38. Pena, M. A.; Fierro, J. L. G., Chemical Structures and Performance of Perovskite Oxides. *Chem. Rev.* **2001,** 101, (7), 1981-2018.
39. Hill, N. A., Why Are There so Few Magnetic Ferroelectrics? *Journal of Physical Chemistry B* **2000,** 104, (29), 6694-6709.
40. Huang, L.; Chen, Z.; Wilson, J. D.; Banerjee, S.; Robinson, R. D.; Herman, I. P.; Laibowitz, R.; O'Brien, S., Barium titanate nanocrystals and nanocrystal thin films: Synthesis, ferroelectricity, and dielectric properties. *Journal of Applied Physics* **2006,** 100, (3), 034316-10.
41. Niederberger, M.; Pinna, N.; Polleux, J.; Antonietti, M., A General Soft-Chemistry Route to Perovskites and Related Materials: Synthesis of $BaTiO_3$, $BaZrO_3$, and $LiNbO_3$ Nanoparticles. *Angewandte Chemie International Edition* **2004,** 43, (17), 2270-2273.
42. Liu, H.; Hu, C.; Wang, Z. L., Composite-Hydroxide-Mediated Approach for the Synthesis of Nanostructures of Complex Functional-Oxides. *Nano Letters* **2006,** 6, (7), 1535-1540.
43. Bansal, V.; Poddar, P.; Ahmad, A.; Sastry, M., Room-Temperature Biosynthesis of Ferroelectric Barium Titanate Nanoparticles. *Journal of the American Chemical Society* **2006,** 128, (36), 11958-11963.
44. Brutchey, R. L.; Morse, D. E., Template-Free, Low-Temperature Synthesis of Crystalline Barium Titanate Nanoparticles under Bio-Inspired Conditions. *Angewandte Chemie International Edition* **2006,** 45, (39), 6564-6566.
45. Wada, S.; Tsurumi, T.; Chikamori, H.; Noma, T.; Suzuki, T., Preparation of nm-sized BaTiO3 crystallites by a LTDS method using a highly concentrated aqueous solution. *Journal of Crystal Growth* **2001,** 229, (1-4), 433-439.

46. Xu, H.; Lian, G., Tetragonal Nanocrystalline Barium Titanate Powder: Preparation, Characterization, and Dielectric Properties. *Journal of the American Ceramic Society* **2003,** 86, (1), 203.
47. Arya, P. R.; Jha, P.; Ganguli, A. K., Synthesis, characterization and dielectric properties of nanometer-sized barium strontium titanates prepared by the polymeric citrate precursor method. *Journal of Materials Chemistry* **2003,** 13, (2), 415-423.
48. Dutta, P. K.; Gregg, J. R., Hydrothermal synthesis of tetragonal barium titanate (BaTiO3). *Chem. Mater.* **1992,** 4, (4), 843-846.
49. Dutta, P. K.; Asiaie, R.; Akbar, S. A.; Zhu, W., Hydrothermal Synthesis and Dielectric Properties of Tetragonal BaTiO3. *Chem. Mater.* **1994,** 6, (9), 1542-1548.
50. Um, M. H.; Kumazawa, H., Hydrothermal synthesis of ferroelectric barium and strontium titanate extremely fine particles. *Journal of Materials Science* **2000,** 35, (5), 1295-1300.
51. Mao, Y. B.; Banerjee, S.; Wong, S. S., Hydrothermal synthesis of perovskite nanotubes. *Chemical Communications* **2003**, (3), 408-409.
52. Frey, M. H.; Payne, D. A., Synthesis and processing of barium titanate ceramics from alkoxide solutions and monolithic gels. *Chem. Mater.* **1995,** 7, (1), 123-129.
53. Junquera, J.; Ghosez, P., Critical thickness for ferroelectricity in perovskite ultrathin films. *Nature* **2003,** 422, (6931), 506-509.
54. Dawber, M.; Chandra, P.; Littlewood, P. B.; Scott, J. F., Depolarization corrections to the coercive field in thin-film ferroelectrics. *Journal of Physics: Condensed Matter* **2003,** 15, (24), L393-L398.
55. Nuraje, N.; Su, K.; Haboosheh, A.; Samson, J.; Manning, E. P.; Yang, N. l.; Matsui, H., Room Temperature Synthesis of Ferroelectric Barium Titanate Nanoparticles Using Peptide Nanorings as Templates. *Advanced Materials* **2006,** 18, (6), 807-811.
56. Petkov, V.; Gateshki, M.; Niederberger, M.; Ren, Y., Atomic-Scale Structure of Nanocrystalline $Ba_xSr_{1-x}TiO_3$ (x= 1, 0.5, 0) by X-ray Diffraction and the Atomic Pair Distribution Function Technique. *Chemistry of Materials* **2006,** 18, (3), 814-821.
57. Lee, J. K., L.; Kim, J.; Kim, Y.; Jung, D., *In Fundamental Physics of Ferroelectrics 2002*. American Institute of Physics: Washington, DC, 2002; p 178.
58. Pileni, M.-P., The role of soft colloidal templates in controlling the size and shape of inorganic nanocrystals. *Nat Mater* **2003,** 2, (3), 145-150.
59. Su, K. Y., Nanloh Synthesis of strontium titanate/polyaniline nanocomposites and the study of their electrorheological effect. *Polymer Preprints (American Chemical Society, Division of Polymer Chemistry)* **2004,** 45, (2), 533-534
60. Davis, J. L.; Rubin, L. G., Some Dielectric Properties of Barium-Strontium Titanate Ceramics at 3000 Megacycles. *Journal of Applied Physics* **1953,** 24, (9), 1194-1197.
61. Kisaka, S. I., Seiji; Sasaki, Hiromu Dielectric properties of mixed crystals of barium-strontium titanate. *Journal of the Physical Society of Japan* **1959,** 14, 1680-1685.
62. Hilton, A. D.; Ricketts, B. W., Dielectric properties of ceramics. *Journal of Physics D: Applied Physics* **1996,** 29, (5), 1321-1325.

63. Tanaka, H.; Tabata, H.; Ota, K. i.; Kawai, T., Molecular-dynamics prediction of structural anomalies in ferroelectric and dielectric $BaTiO_3$-$SrTiO_3$-$CaTiO_3$ solid solutions. *Physical Review B* **1996,** 53, (21), 14112.
64. Yashima, M.; Hoshina, T.; Ishimura, D.; Kobayashi, S.; Nakamura, W.; Tsurumi, T.; Wada, S., Size effect on the crystal structure of barium titanate nanoparticles. *Journal of Applied Physics* **2005,** 98, (1), 014313-8.
65. Nuraje, N.; Su, K.; Matsui, H., Catalytic growth of silica nanoparticles in controlled shapes at planar liquid/liquid interfaces. *New Journal of Chemistry* **2007,** 31, (11), 1895-1898.
66. Puntes, V. F.; Krishnan, K. M.; Alivisatos, A. P., Colloidal nanocrystal shape and size control: the case of cobalt. *Science* **2001,** 291, (5511), 2115-2117.
67. Jun, Y.-w.; Choi, J.-s.; Cheon, J., Shape Control of Semiconductor and Metal Oxide Nanocrystals through Nonhydrolytic Colloidal Routes. *Angewandte Chemie International Edition* **2006,** 45, (21), 3414-3439.
68. Xia, Y.; Yang, P.; Sun, Y.; Wu, Y.; Mayers, B.; Gates, B.; Yin, Y.; Kim, F.; Yan, H., One-Dimensional Nanostructures: Synthesis, Characterization, and Applications. *Advanced Materials* **2003,** 15, (5), 353-389.
69. Tian, N.; Zhou, Z.-Y.; Sun, S.-G.; Ding, Y.; Wang, Z. L., Synthesis of Tetrahexahedral Platinum Nanocrystals with High-Index Facets and High Electro-Oxidation Activity. *Science* **2007,** 316, (5825), 732-735.
70. Mullin, J. W., *Crystalization*. Butterworth-Heinmann: Woburn, MA, 1997.
71. Belcher, A. M.; Wu, X. H.; Christensen, R. J.; Hansma, P. K.; Stucky, G. D.; Morse, D. E., Control of crystal phase switching and orientation by soluble mollusc-shell proteins. *Nature* **1996,** 381, (6577), 56-58.
72. Tang, J.; Cui, X.; Liu, Y.; Yang, X., Morphology-Controlled Synthesis of Monodisperse ZnO Troughs at the Air-Water Interface under Mild Conditions. *Journal of Physical Chemistry B* **2005,** 109, (47), 22244-22249.
73. Gou, L.; Murphy, C. J., Solution-Phase Synthesis of Cu_2O Nanocubes. *Nano Letters* **2003,** 3, (2), 231-234.
74. Jin, R.; Cao, Y.; Mirkin, C. A.; Kelly, K. L.; Schatz, G. C.; Zheng, J. G., Photoinduced Conversion of Silver Nanospheres to Nanoprisms. *Science* **2001,** 294, (5548), 1901-1903.
75. Brown, S.; Sarikaya, M.; Johnson, E., A genetic analysis of crystal growth. *Journal of Molecular Biology* **2000,** 299, (3), 725-735.
76. Mann, S.; Archibald, D. D.; Didymus, J. M.; Douglas, T.; Heywood, B. R.; Meldrum, F. C.; Reeves, N. J., Crystallization at inorganic-organic interfaces: biominerals and biomimetic synthesis *Science* **1993,** 261, 1286–1292
77. Han, Y.-J.; Wysocki, L. M.; Thanawala, M. S.; Siegrist, T.; Aizenberg, J., Template-Dependent Morphogenesis of Oriented Calcite Crystals in the Presence of Magnesium Ions. *Angewandte Chemie International Edition* **2005,** 44, (16), 2386-2390.
78. Cölfen, H.; Antonietti, M., Mesocrystals: Inorganic Superstructures Made by Highly Parallel Crystallization and Controlled Alignment. *Angewandte Chemie International Edition* **2005,** 44, (35), 5576-5591.
79. Umetsu, M.; Mizuta, M.; Tsumoto, K.; Ohara, S.; Takami, S.; Watanabe, H.; Kumagai, I.; Adschiri, T., Bioassisted Room-Temperature Immobilization and

Mineralization of Zinc Oxide - The Structural Ordering of ZnO Nanoparticles into a Flower-Type Morphology. *Advanced Materials* **2005,** 17, (21), 2571-2575.
80. Russell, J. T.; Lin, Y.; Böker, A.; Su, L.; Carl, P.; Zettl, H.; He, J.; Sill, K.; RavisubhashTangirala; Emrick, T.; Littrell, K.; Thiyagarajan, P.; Cookson, D.; Fery, A.; Wang, Q.; Russell, T. P., Self-Assembly and Cross-Linking of Bionanoparticles at Liquid-Liquid Interfaces. *Angewandte Chemie International Edition* **2005,** 44, (16), 2420-2426.
81. Velev, O. D.; Furusawa, K.; Nagayama, K., Assembly of Latex Particles by Using Emulsion Droplets as Templates. 1. Microstructured Hollow Spheres. *Langmuir* **1996,** 12, (10), 2374-2384.
82. Binks, B. P.; Clint, J. H., Solid Wettability from Surface Energy Components: Relevance to Pickering Emulsions. *Langmuir* **2002,** 18, (4), 1270-1273.
83. Dinsmore, A. D.; Hsu, M. F.; Nikolaides, M. G.; Marquez, M.; Bausch, A. R.; Weitz, D. A., Colloidosomes: Selectively Permeable Capsules Composed of Colloidal Particles. *Science* **2002,** 298, (5595), 1006-1009.
84. Song, X.; Sun, S.; Zhang, W.; Yu, H.; Fan, W., Synthesis of $Cu(OH)_2$ Nanowires at Aqueous-Organic Interfaces. *Journal of Physical Chemistry B* **2004,** 108, (17), 5200-5205.
85. Nuraje, N.; Su, K.; Zhang, L. Z.; Chu, I. W.; Peetz, R. M.; Matsui, H.; Yang, N. L., Fast conductance switching in single-crystal organic nanoneedles prepared from an interfacial polymerization-crystallization of 3,4-ethylenedioxythiophene. *Advanced Materials* **2007,** 19, (5), 669-+.
86. Benjamin, I., Chemical Reactions and Solvation at Liquid Interfaces: A Microscopic Perspective. *Chemical Reviews* **1996,** 96, (4), 1449-1476.
87. Nakashima, T.; Kimizuka, N., Interfacial Synthesis of Hollow TiO_2 Microspheres in Ionic Liquids. *Journal of the American Chemical Society* **2003,** 125, (21), 6386-6387.
88. Johans, C.; Liljeroth, P.; Kontturi, K., Electrodeposition at polarisable liquid|liquid interfaces: The role of interfacial tension on nucleation kinetics. *Physical Chemistry Chemical Physics* **2002,** 4, (6), 1067-1071.
89. Yang, H.; Coombs, N.; Ozin, G. A., Morphogenesis of shapes and surface patterns in mesoporous silica. *Nature* **1997,** 386, (6626), 692-695.
90. Nakanishi, T.; Schmitt, W.; Michinobu, T.; Kurth, D. G.; Ariga, K., Hierarchical supramolecular fullerene architectures with controlled dimensionality. *Chemical Communications* **2005**, (48), 5982-5984.
91. Brinker, C. J.; Scherer, G., *Sol-Gel Science*. Academic Press: Boston, MA, 1990.
92. Filankembo, A.; Giorgio, S.; Lisiecki, I.; Pileni, M. P., Is the Anion the Major Parameter in the Shape Control of Nanocrystals? *Journal of Physical Chemistry B* **2003,** 107, (30), 7492-7500.
93. Chemseddine, A.; Jungblut, H.; Boulmaaz, S., Investigation of the Nanocluster Self-Assembly Process by Scanning Tunneling Microscopy and Optical Spectroscopy. *J. Physical Chemistry* **1996,** 100, (30), 12546-12551.
94. Sugimoto, T.; Zhou, X.; Muramatsu, A., Synthesis of uniform anatase TiO_2 nanoparticles by gel-sol method: 4. Shape control. *Journal of Colloid and Interface Science* **2003,** 259, (1), 53-61.

95. Gross, M.; Muller, D. C.; Nothofer, H. G.; Scherf, U.; Neher, D.; Brauchle, C.; Meerholz, K., Improving the performance of doped pi-conjugated polymers for use in organic light-emitting diodes. *Nature* **2000,** 405, (6787), 661-665.
96. Tretiak, S.; Saxena, A.; Martin, R. L.; Bishop, A. R., Photoexcited breathers in conjugated polyenes: An excited-state molecular dynamics study. *Proceedings of the National Academy of Sciences of the United States of America* **2003,** 100, (5), 2185-2190.
97. Chen, L. H.; McBranch, D. W.; Wang, H. L.; Helgeson, R.; Wudl, F.; Whitten, D. G., Highly sensitive biological and chemical sensors based on reversible fluorescence quenching in a conjugated polymer. *Proceedings of the National Academy of Sciences of the United States of America* **1999,** 96, (22), 12287-12292.
98. Hide, F.; DiazGarcia, M. A.; Schwartz, B. J.; Andersson, M. R.; Pei, Q. B.; Heeger, A. J., Semiconducting polymers: A new class of solid-state laser materials. *Science* **1996,** 273, (5283), 1833-1836.
99. Dimitrakopoulos, C. D.; Mascaro, D. J., Organic thin-film transistors: A review of recent advances. *Ibm Journal of Research and Development* **2001,** 45, (1), 11-27.
100. Collier, C. P.; Wong, E. W.; Belohradsky, M.; Raymo, F. M.; Stoddart, J. F.; Kuekes, P. J.; Williams, R. S.; Heath, J. R., Electronically configurable molecular-based logic gates. *Science* **1999,** 285, (5426), 391-394.
101. He, H. X.; Zhu, J. S.; Tao, N. J.; Nagahara, L. A.; Amlani, I.; Tsui, R., A conducting polymer nanojunction switch. *Journal of the American Chemical Society* **2001,** 123, (31), 7730-7731.
102. Ramachandran, G. K.; Hopson, T. J.; Rawlett, A. M.; Nagahara, L. A.; Primak, A.; Lindsay, S. M., A bond-fluctuation mechanism for stochastic switching in wired molecules. *Science* **2003,** 300, (5624), 1413-1416.
103. Terabe, K.; Hasegawa, T.; Nakayama, T.; Aono, M., Quantized conductance atomic switch. *Nature* **2005,** 433, (7021), 47-50.
104. Sakaguchi, H.; Matsumura, H.; Gong, H., Electrochemical epitaxial polymerization of single-molecular wires. *Nature Materials* **2004,** 3, (8), 551-557.
105. Ong, B. S.; Wu, Y. L.; Liu, P.; Gardner, S., Structurally ordered polythiophene nanoparticles for high-performance organic thin-film transistors. *Advanced Materials* **2005,** 17, (9), 1141-+.
106. Winther-Jensen, B.; Chen, J.; West, K.; Wallace, G., Vapor phase polymerization of pyrrole and thiophene using iron(III) sulfonates as oxidizing agents. *Macromolecules* **2004,** 37, (16), 5930-5935.
107. Krebs, F. C.; Biancardo, M.; Winther-Jensen, B.; Spanggard, H.; Alstrup, J., Strategies for incorporation of polymer photovoltaics into garments and textiles. *Solar Energy Materials and Solar Cells* **2006,** 90, (7-8), 1058-1067.
108. Krebs, F. C.; Jorgensen, M., High carrier mobility in a series of new semiconducting PPV-type polymers. *Macromolecules* **2003,** 36, (12), 4374-4384.
109. Wegner, G.; Monkenbusch, M.; Wieners, G.; Weizenhofer, R.; Lieser, G.; Wernet, W., New Routes to Conducting Polymers and New Insights into Structure-Properties Relations. *Molecular Crystals and Liquid Crystals* **1985,** 118, (1-4), 85-94.
110. Sirringhaus, H.; Brown, P. J.; Friend, R. H.; Nielsen, M. M.; Bechgaard, K.; Langeveld-Voss, B. M. W.; Spiering, A. J. H.; Janssen, R. A. J.; Meijer, E. W.;

Herwig, P.; de Leeuw, D. M., Two-dimensional charge transport in self-organized, high-mobility conjugated polymers. *Nature* **1999,** 401, (6754), 685-688.
111. Meng, H.; Perepichka, D. F.; Bendikov, M.; Wudl, F.; Pan, G. Z.; Yu, W. J.; Dong, W. J.; Brown, S., Solid-state synthesis of a conducting polythiophene via an unprecedented heterocyclic coupling reaction. *Journal of the American Chemical Society* **2003,** 125, (49), 15151-15162.
112. Heeger, A. J., Semiconducting and metallic polymers: The fourth generation of polymeric materials (Nobel lecture). *Angewandte Chemie-International Edition* **2001,** 40, (14), 2591-2611.
113. Leclerc, M.; Diaz, F. M.; Wegner, G., Structural-Analysis of Poly(3-Alkylthiophene)S. *Makromolekulare Chemie-Macromolecular Chemistry and Physics* **1989,** 190, (12), 3105-3116.
114. Andreani, F.; Bizzari, P. C.; Dellacasa, C.; Salatelli, E., 1st Approach to Ester-Functionalized Poly(3-Alkylthienylene)S. *Polymer Bulletin* **1991,** 27, (2), 117-121.
115. Abdou, M. S. A.; Lu, X. T.; Xie, Z. W.; Orfino, F.; Deen, M. J.; Holdcroft, S., Nature of Impurities in Pi-Conjugated Polymers Prepared by Ferric-Chloride and Their Effect on the Electrical-Properties of Metal-Insulator-Semiconductor Structures. *Chemistry of Materials* **1995,** 7, (4), 631-641.
116. McCullough, R. D., The chemistry of conducting polythiophenes. *Advanced Materials* **1998,** 10, (2), 93-+.
117. Huang, J. X.; Kaner, R. B., A general chemical route to polyaniline nanofibers. *Journal of the American Chemical Society* **2004,** 126, (3), 851-855.
118. Joo, J.; Long, S. M.; Pouget, J. P.; Oh, E. J.; MacDiarmid, A. G.; Epstein, A. J., Charge transport of the mesoscopic metallic state in partially crystalline polyanilines. *Physical Review B* **1998,** 57, (16), 9567-9580.
119. Mo, Z.; Lee, K. B.; Moon, Y. B.; Kobayashi, M.; Heeger, A. J.; Wudl, F., X-Ray-Scattering from Polythiophene - Crystallinity and Crystallographic Structure. *Macromolecules* **1985,** 18, (10), 1972-1977.
120. Granstrom, M.; Inganas, O., Electrically Conductive Polymer Fibers with Mesoscopic Diameters .1. Studies of Structure and Electrical-Properties. *Polymer* **1995,** 36, (15), 2867-2872.
121. Groenendaal, L.; Jonas, F.; Freitag, D.; Pielartzik, H.; Reynolds, J. R., Poly(3,4-ethylenedioxythiophene) and Its Derivatives: Past, Present, and Future. *Advanced Materials* **2000,** 12, (7), 481-494.
122. Aasmundtveit, K. E.; Samuelsen, E. J.; Inganas, O.; Pettersson, L. A. A.; Johansson, T.; Ferrer, S., Structural aspects of electrochemical doping and dedoping of poly(3,4-ethylenedioxythiophene). *Synthetic Metals* **2000,** 113, (1-2), 93-97.
123. Niu, L.; Kvarnstrom, C.; Froberg, K.; Ivaska, A., Electrochemically controlled surface morphology and crystallinity in poly(3,4-ethylenedioxythiophene) films. *Synthetic Metals* **2001,** 122, (2), 425-429.
124. Ozaki, M.; Kratohvil, S.; Matijevic, E., Formation of Monodispersed Spindle-Type Hematite Particles. *Journal of Colloid and Interface Science* **1984,** 102, (1), 146-151.
125. Shafi, K.; Ulman, A.; Yan, X. Z.; Yang, N. L.; Estournes, C.; White, H.; Rafailovich, M., Sonochemical synthesis of functionalized amorphous iron oxide nanoparticles. *Langmuir* **2001,** 17, (16), 5093-5097.

126. Donhauser, Z. J.; Mantooth, B. A.; Kelly, K. F.; Bumm, L. A.; Monnell, J. D.; Stapleton, J. J.; Price, D. W.; Rawlett, A. M.; Allara, D. L.; Tour, J. M.; Weiss, P. S., Conductance switching in single molecules through conformational changes. *Science* **2001,** 292, (5525), 2303-2307.
127. Ulanski, J.; Glatzhofer, D. T.; Wegner, G., Comment on the Application of the Voltage Shorted Compaction (Vsc) Technique to Conducting Polymers. *Makromolekulare Chemie-Rapid Communications* **1986,** 7, (6), 361-363.
128. Nuraje, N.; Su, K.; Yang, N.-l.; Matsui, H., Liquid/liquid interfacial polymerization to grow single crystalline nanoneedles of various conducting polymers. *ACS nano* **2008,** ASAP.
129. Huang, J.; Kaner, R. B., A General Chemical Route to Polyaniline Nanofibers. *Journal of the American Chemical Society* **2004,** 126, (3), 851-855.
130. Huang, J.; Kaner, R. B., Nanofiber Formation in the Chemical Polymerization of Aniline: A Mechanistic Study. *Angewandte Chemie International Edition* **2004,** 43, (43), 5817-5821.
131. Xia, Y.; Wiesinger, J. M.; MacDiarmid, A. G.; Epstein, A. J., Camphorsulfonic Acid Fully Doped Polyaniline Emeraldine Salt: Conformations in Different Solvents Studied by an Ultraviolet/Visible/Near-Infrared Spectroscopic Method. *Chem. Mater.* **1995,** 7, (3), 443-445.
132. Nuraje, N.; Banerjee, I. A.; MacCuspie, R. I.; Yu, L. T.; Matsui, H., Biological bottom-up assembly of antibody nanotubes on patterned antigen arrays. *Journal of the American Chemical Society* **2004,** 126, (26), 8088-8089.
133. Zhong, Z. H.; Wang, D. L.; Cui, Y.; Bockrath, M. W.; Lieber, C. M., Nanowire crossbar arrays as address decoders for integrated nanosystems. *Science* **2003,** 302, (5649), 1377-1379.
134. Chen, R. J.; Bangsaruntip, S.; Drouvalakis, K. A.; Kam, N. W. S.; Shim, M.; Li, Y. M.; Kim, W.; Utz, P. J.; Dai, H. J., Noncovalent functionalization of carbon nanotubes for highly specific electronic biosensors. *Proceedings of the National Academy of Sciences of the United States of America* **2003,** 100, (9), 4984-4989.
135. Fennimore, A. M.; Yuzvinsky, T. D.; Han, W. Q.; Fuhrer, M. S.; Cumings, J.; Zettl, A., Rotational actuators based on carbon nanotubes. *Nature* **2003,** 424, (6947), 408-410.
136. Sumerel, J. L.; Yang, W. J.; Kisailus, D.; Weaver, J. C.; Choi, J. H.; Morse, D. E., Biocatalytically templated synthesis of titanium dioxide. *Chemistry of Materials* **2003,** 15, (25), 4804-4809.
137. Wang, Q.; Lin, T. W.; Tang, L.; Johnson, J. E.; Finn, M. G., Icosahedral virus particles as addressable nanoscale building blocks. *Angewandte Chemie-International Edition* **2002,** 41, (3), 459-462.
138. Mao, C. B.; Solis, D. J.; Reiss, B. D.; Kottmann, S. T.; Sweeney, R. Y.; Hayhurst, A.; Georgiou, G.; Iverson, B.; Belcher, A. M., Virus-based toolkit for the directed synthesis of magnetic and semiconducting nanowires. *Science* **2004,** 303, (5655), 213-217.
139. Slocik, J. M.; Moore, J. T.; Wright, D. W., Monoclonal antibody recognition of histidine-rich peptide encapsulated nanoclusters. *Nano Letters* **2002,** 2, (3), 169-173.

140. Douglas, T.; Strable, E.; Willits, D.; Aitouchen, A.; Libera, M.; Young, M., Protein engineering of a viral cage for constrained nanomaterials synthesis. *Advanced Materials* **2002,** 14, (6), 415-+.
141. Sano, K. I.; Shiba, K., A hexapeptide motif that electrostatically binds to the surface of titanium. *Journal of the American Chemical Society* **2003,** 125, (47), 14234-14235.
142. Li, Z.; Chung, S. W.; Nam, J. M.; Ginger, D. S.; Mirkin, C. A., Living templates for the merarchical assembly of gold nanoparticles. *Angewandte Chemie-International Edition* **2003,** 42, (20), 2306-2309.
143. Melosh, N. A.; Boukai, A.; Diana, F.; Gerardot, B.; Badolato, A.; Petroff, P. M.; Heath, J. R., Ultrahigh-density nanowire lattices and circuits. *Science* **2003,** 300, (5616), 112-115.
144. Javey, A.; Guo, J.; Wang, Q.; Lundstrom, M.; Dai, H. J., Ballistic carbon nanotube field-effect transistors. *Nature* **2003,** 424, (6949), 654-657.
145. Rao, S. G.; Huang, L.; Setyawan, W.; Hong, S. H., Large-scale assembly of carbon nanotubes. *Nature* **2003,** 425, (6953), 36-37.
146. Liu, G. Y.; Xu, S.; Qian, Y. L., Nanofabrication of self-assembled monolayers using scanning probe lithography. *Accounts of Chemical Research* **2000,** 33, (7), 457-466.
147. Douberly, G. E.; Pan, S.; Walters, D.; Matsui, H., Fabrication of Protein Tubules: Immobilization of Proteins on Peptide Tubules. *Journal of Physical Chemistry B* **2001,** 105, (32), 7612-7618.
148. Djalali, R.; Chen, Y. F.; Matsui, H., Au nanocrystal growth on nanotubes controlled by conformations and charges of sequenced peptide templates. *Journal of the American Chemical Society* **2003,** 125, (19), 5873-5879.
149. Yu, L. T.; Banerjee, I. A.; Matsui, H., Direct growth of shape-controlled nanocrystals on nanotubes via biological recognition. *Journal of the American Chemical Society* **2003,** 125, (48), 14837-14840.
150. Djalali, R.; Chen, Y.; Matsui, H., Au nanowire fabrication from sequenced histidine-rich peptide. *Journal of the American Chemical Society* **2002,** 124, (46), 13660-13661.
151. Lee, K. B.; Lim, J. H.; Mirkin, C. A., Protein nanostructures formed via direct-write dip-pen nanolithography. *Journal of the American Chemical Society* **2003,** 125, (19), 5588-5589.
152. Liu, G. Y.; Amro, N. A., Positioning protein molecules on surfaces: A nanoengineering approach to supramolecular chemistry. *Proceedings of the National Academy of Sciences of the United States of America* **2002,** 99, (8), 5165-5170.
153. Yang, L.; Nuraje, N.; Bai, H.; Matsui, H., Crossbar assembly of antibody-functionalized peptide nanotubes via biomimetic molecular recognition. *Journal of Peptide Science* **2007,** 9999, (9999), n/a.
154. Smith, P. A.; Nordquist, C. D.; Jackson, T. N.; Mayer, T. S.; Martin, B. R.; Mbindyo, J.; Mallouk, T. E., Electric-field assisted assembly and alignment of metallic nanowires. *Applied Physics Letters* **2000,** 77, (9), 1399-1401.
155. Lumsdon, S. O.; Kaler, E. W.; Velev, O. D., Two-Dimensional Crystallization of Microspheres by a Coplanar AC Electric Field. *Langmuir* **2004,** 20, (6), 2108-2116.

156. Hamers, R. J.; Beck, J. D.; Eriksson, M. A.; Li, B.; Marcus, M. S.; Shang, L.; Simmons, J.; Streifer, J. A., Electrically directed assembly and detection of nanowire bridges in aqueous media. *Nanotechnology* **2006,** 17, (11), S280-S286.
157. Ryan, K. M.; Mastroianni, A.; Stancil, K. A.; Liu, H.; Alivisatos, A. P., Electric-Field-Assisted Assembly of Perpendicularly Oriented Nanorod Superlattices. *Nano Letters* **2006,** 6, (7), 1479-1482.
158. Huang, Y.; Duan, X.; Cui, Y.; Lauhon, L. J.; Kim, K.-H.; Lieber, C. M., Logic Gates and Computation from Assembled Nanowire Building Blocks. *Science* **2001,** 294, (5545), 1313-1317.
159. Rao, S. G.; Huang, L.; Setyawan, W.; Hong, S., Nanotube electronics: Large-scale assembly of carbon nanotubes. *Nature* **2003,** 425, (6953), 36-37.
160. Liu, S.; Tok, J. B. H.; Locklin, J.; Bao, Z., Assembly and Alignment of Metallic Nanorods on Surfaces with Patterned Wettability. *Small* **2006,** 2, (12), 1448-1453.
161. Huang, X. M. H.; Caldwell, R.; Huang, L.; Jun, S. C.; Huang, M.; Sfeir, M. Y.; O'Brien, S. P.; Hone, J., Controlled Placement of Individual Carbon Nanotubes. *Nano Letters* **2005,** 5, (7), 1515-1518.
162. Yu, G.; Cao, A.; Lieber, C. M., Large-area blown bubble films of aligned nanowires and carbon nanotubes. *Nature Nanotechnology* **2007,** 2, (6), 372-377.
163. Reches, M.; Gazit, E., Controlled patterning of aligned self-assembled peptide nanotubes. *Nature Nanotechnology* **2006,** 1, (3), 195-200.
164. Huang, Y.; Duan, X.; Wei, Q.; Lieber, C. M., Directed Assembly of One-Dimensional Nanostructures into Functional Networks. *Science* **2001,** 291, (5504), 630-633.
165. Lin, C.; Katilius, E.; Liu, Y.; Zhang, J.; Yan, H., Self-Assembled Signaling Aptamer DNA Arrays for Protein Detection. *Angewandte Chemie International Edition* **2006,** 45, (32), 5296-5301.
166. Mao, C.; LaBean, T. H.; Reif, J. H.; Seeman, N. C., Logical computation using algorithmic self-assembly of DNA triple-crossover molecules. *Nature* **2000,** 407, (6803), 493-496.
167. Braun, E.; Eichen, Y.; Sivan, U.; Ben-Yoseph, G., DNA-templated assembly and electrode attachment of a conducting silver wire. *Nature* **1998,** 391, (6669), 775-778.
168. Mbindyo, J. K. N.; Reiss, B. D.; Martin, B. R.; Keating, C. D.; Natan, M. J.; Mallouk, T. E., DNA-Directed Assembly of Gold Nanowires on Complementary Surfaces. *Advanced Materials* **2001,** 13, (4), 249-254.
169. Bentzen, E. L.; House, F.; Utley, T. J.; Crowe, J. E.; Wright, D. W., Progression of Respiratory Syncytial Virus Infection Monitored by Fluorescent Quantum Dot Probes. *Nano Letters* **2005,** 5, (4), 591-595.
170. Alivisatos, A. P.; Weiwei, G.; Larabell, C., QUANTUM DOTS AS CELLULAR PROBES. *Annual Review of Biomedical Engineering* **2005,** 7, (1), 55-C-3.
171. Zhao, Z.; Matsui, H., Accurate Immobilization of Antibody-Functionalized Peptide Nanotubes on Protein-Patterned Arrays by Optimizing their Ligand-Receptor Interactions. *Small* **2007,** 3, (8), 1390-1393.

172. Zhao, Z. Y.; Banerjee, P. A.; Matsui, H., Simultaneous targeted immobilization of anti-human IgG-coated nanotubes and anti-mouse IgG-coated nanotubes on the complementary antigen-patterned surfaces via biological molecular recognition. *Journal of the American Chemical Society* **2005,** 127, (25), 8930-8931.
173. Gao, X. Y.; Matsui, H., Peptide-based nanotubes and their applications in bionanotechnology. *Advanced Materials* **2005,** 17, (17), 2037-2050.
174. Gao, X.; Djalali, R.; Haboosheh, A.; Samson, J.; Nuraje, N.; Matsui, H., Peptide Nanotubes: Simple Separation Using Size-Exclusion Columns and Use as Templates for Fabricating One-Dimensional Single Chains of Au Nanoparticles. *Advanced Materials* **2005,** 17, (14), 1753-1757.
175. Chapman, R. G.; Ostuni, E.; Takayama, S.; Holmlin, R. E.; Yan, L.; Whitesides, G. M., Surveying for surfaces that resist the adsorption of proteins. *J. Am. Chem. Soc.* **2000,** 122, 8303-8304.
176. Ostuni, E.; Chapman, R. G.; Holmlin, R. E.; Takayama, S.; Whitesides, G. M., A survey of structure-property relationships of surfaces that resist the adsorption of protein. *Langmuir* **2001,** 17, 5605-5620.
177. Tlili, A.; Abdelghani, A.; Ameur, S.; Jaffrezic-Renault, N., Impedance spectroscopy and affinity measurement of specific antibody-antigen interaction. *Materials Science and Engineering: C* **2006,** 26, (2-3), 546-550.
178. Im, J.; Huang, L.; Kang, J.; Lee, M.; Lee, D. J.; Rao, S. G.; Lee, N.-K.; Hong, S., ``Sliding kinetics'' of single-walled carbon nanotubes on self-assembled monolayer patterns: Beyond random adsorption. *The Journal of Chemical Physics* **2006,** 124, (22), 224707-6.
179. Sato, T.; Ahmed, H.; Brown, D.; Johnson, B. F. G., Single electron transistor using a molecularly linked gold colloidal particle chain. *Journal of Applied Physics* **1997,** 82, (2), 696-701.
180. Berven, C. A.; Wybourne, M. N., Effect of self-capacitance on the tunneling thresholds in linear arrays of nanoparticles. *Applied Physics Letters* **2001,** 78, (24), 3893-3895.
181. Persson, S. H. M.; Olofsson, L.; Gunnarsson, L., A self-assembled single-electron tunneling transistor. *Applied Physics Letters* **1999,** 74, (17), 2546-2548.
182. Klein, D. L.; McEuen, P. L.; Katari, J. E. B.; Roth, R.; Alivisatos, A. P., An approach to electrical studies of single nanocrystals. *Applied Physics Letters* **1996,** 68, (18), 2574-2576.
183. Alivisatos, A. P., Semiconductor Clusters, Nanocrystals, and Quantum Dots. *Science* **1996,** 271, (5251), 933-937.
184. Redl, F. X.; Cho, K. S.; Murray, C. B.; O'Brien, S., Three-dimensional binary superlattices of magnetic nanocrystals and semiconductor quantum dots. *Nature* **2003,** 423, (6943), 968-971.
185. Beverly, K. C.; Sample, J. L.; Sampaio, J. F.; Remacle, F.; Heath, J. R.; Levine, R. D., Quantum dot artificial solids: Understanding the static and dynamic role of size and packing disorder. *Proceedings of the National Academy of Sciences* **2002,** 99, (90002), 6456-6459.
186. Remacle, F.; Beverly, K. C.; Heath, J. R.; Levine, R. D., Conductivity of 2-D Ag Quantum Dot Arrays: Computational Study of the Role of Size and Packing

Disorder at Low Temperatures. *Journal of Physical Chemistry B* **2002,** 106, (16), 4116-4126.
187. Sample, J. L.; Beverly, K. C.; Chaudhari, P. R.; Remacle, F.; Heath, J. R.; Levine, R. D., Imaging Transport Disorder in Conducting Arrays of Metallic Quantum Dots: An Experimental and Computational Study. *Advanced Materials* **2002,** 14, (2), 124-128.
188. Feldheim, D. L.; Keating, C. D., Self-assembly of single electron transistors and related devices. *chemical society reviews* **1998,** 27, 1-12.
189. Park, H.; Lim, A. K. L.; Alivisatos, A. P.; Park, J.; McEuen, P. L., Fabrication of metallic electrodes with nanometer separation by electromigration. *Applied Physics Letters* **1999,** 75, (2), 301-303.
190. Junno, T.; Magnusson, M. H.; Carlsson, S. B.; Deppert, K.; Malm, J. O.; Montelius, L.; Samuelson, L., Single-electron devices via controlled assembly of designed nanoparticles. *Microelectronic Engineering* **1999,** 47, (1-4), 179-183.
191. Kim, T. W.; Choo, D. C.; Shim, J. H.; Kang, S. O., Single-electron transistors operating at room temperature, fabricated utilizing nanocrystals created by focused-ion beam. *Applied Physics Letters* **2002,** 80, (12), 2168-2170.
192. Bolotin, K. I.; Kuemmeth, F.; Pasupathy, A. N.; Ralph, D. C., Metal-nanoparticle single-electron transistors fabricated using electromigration. *Applied Physics Letters* **2004,** 84, (16), 3154-3156.
193. Maier, S. A.; Kik, P. G.; Atwater, H. A.; Meltzer, S.; Harel, E.; Koel, B. E.; Requicha, A. A. G., Local detection of electromagnetic energy transport below the diffraction limit in metal nanoparticle plasmon waveguides. *Nature Materials* **2003,** 2, (4), 229-232.
194. Citrin, D. S., Coherent Excitation Transport in Metal-Nanoparticle Chains. *Nano Letters* **2004,** 4, (9), 1561-1565.
195. Maier, S. A.; Kik, P. G.; Atwater, H. A., Observation of coupled plasmon-polariton modes in Au nanoparticle chain waveguides of different lengths: Estimation of waveguide loss. *Applied Physics Letters* **2002,** 81, (9), 1714-1716.
196. Maier, S. A.; Kik, P. G.; Atwater, H. A., Optical pulse propagation in metal nanoparticle chain waveguides. *Physical Review B* **2003,** 67, (20).
197. Li, M.; Schnablegger, H.; Mann, S., Coupled synthesis and self-assembly of nanoparticles to give structures with controlled organization. *Nature* **1999,** 402, (6760), 393-395.
198. Patolsky, F.; Weizmann, Y.; Lioubashevski, O.; Willner, I., Au-Nanoparticle Nanowires Based on DNA and Polylysine Templates. *Angewandte Chemie International Edition* **2002,** 41, (13), 2323-2327.
199. Ma, Y.; Zhang, J.; Zhang, G.; He, H., Polyaniline Nanowires on Si Surfaces Fabricated with DNA Templates. *Journal of the American Chemical Society* **2004,** 126, (22), 7097-7101.
200. Nakao, H.; Shiigi, H.; Yamamoto, Y.; Tokonami, S.; Nagaoka, T.; Sugiyama, S.; Ohtani, T., Highly ordered assemblies of Au nanoparticles organized on DNA. *Nano Letters* **2003,** 3, (10), 1391-1394.
201. Tang, Z.; Kotov, N. A.; Giersig, M., Spontaneous Organization of Single CdTe Nanoparticles into Luminescent Nanowires. *Science* **2002,** 297, (5579), 237-240.

202. Matsui, H.; Pan, S.; Gologan, B.; Jonas, S. H., Bolaamphiphile Nanotube-Templated Metallized Wires. *Journal of Physical Chemistry B* **2000,** 104, (41), 9576-9579.
203. Nuraje, N.; Su, K.; Samson, J.; Haboosheh, A.; Maccuspie, R. I.; Matsui, H., Self-assembly of Au nanoparticle-containing peptide nano-rings on surfaces. *Supramolecular Chemistry* **2006,** 18, (5), 429-434.
204. Murray, C. B.; Kagan, C. R.; Bawendi, M. G., Synthesis and characterization of monodisperse nanocrystals and close-packed nanocrystal assemblies. *Annual Review of Materials Science* **2000,** 30, 545-610.
205. Yablonovitch, E., INHIBITED SPONTANEOUS EMISSION IN SOLID-STATE PHYSICS AND ELECTRONICS. *Physical Review Letters* **1987,** 58, (20), 2059-2062.
206. Joannopoulos, J. D.; Villeneuve, P. R.; Fan, S. H., Photonic crystals: Putting a new twist on light (vol 386, pg 143, 1997). *Nature* **1997,** 387, (6635), 830-830.
207. Vlasov, Y. A.; Bo, X. Z.; Sturm, J. C.; Norris, D. J., On-chip natural assembly of silicon photonic bandgap crystals. *Nature* **2001,** 414, (6861), 289-293.
208. Murray, C. B.; Kagan, C. R.; Bawendi, M. G., Self-Organization of CdSe Nanocrystallites into Three-Dimensional Quantum Dot Superlattices. *Science* **1995,** 270, (5240), 1335-1338.
209. Colvin, V. L., From opals to optics: Colloidal photonic crystals. *Mrs Bulletin* **2001,** 26, (8), 637-641.
210. Blanco, A.; Chomski, E.; Grabtchak, S.; Ibisate, M.; John, S.; Leonard, S. W.; Lopez, C.; Meseguer, F.; Miguez, H.; Mondia, J. P.; Ozin, G. A.; Toader, O.; van Driel, H. M., Large-scale synthesis of a silicon photonic crystal with a complete three-dimensional bandgap near 1.5 micrometres. *Nature* **2000,** 405, (6785), 437-440.
211. Lin, S. Y.; Fleming, J. G.; Hetherington, D. L.; Smith, B. K.; Biswas, R.; Ho, K. M.; Sigalas, M. M.; Zubrzycki, W.; Kurtz, S. R.; Bur, J., A three-dimensional photonic crystal operating at infrared wavelengths. *Nature* **1998,** 394, (6690), 251-253.
212. Liu, X. G.; Fu, L.; Hong, S. H.; Dravid, V. P.; Mirkin, C. A., Arrays of magnetic nanoparticles patterned via "dip-pen" nanolithography. *Advanced Materials* **2002,** 14, (3), 231-+.
213. Lee, W.; Chan, A.; Bevan, M. A.; Lewis, J. A.; Braun, P. V., Nanoparticle-mediated epitaxial assembly of colloidal crystals on patterned substrates. *Langmuir* **2004,** 20, (13), 5262-5270.
214. Huang, J. X.; Kim, F.; Tao, A. R.; Connor, S.; Yang, P. D., Spontaneous formation of nanoparticle stripe patterns through dewetting. *Nature Materials* **2005,** 4, (12), 896-900.
215. Kisailus, D.; Choi, J. H.; Weaver, J. C.; Yang, W. J.; Morse, D. E., Enzymatic synthesis and nanostructural control of gallium oxide at low temperature. *Advanced Materials* **2005,** 17, (3), 314-+.
216. Brott, L. L.; Naik, R. R.; Pikas, D. J.; Kirkpatrick, S. M.; Tomlin, D. W.; Whitlock, P. W.; Clarson, S. J.; Stone, M. O., Ultrafast holographic nanopatterning of biocatalytically formed silica. *Nature* **2001,** 413, (6853), 291-293.

217. Lee, S. Y.; Royston, E.; Culver, J. N.; Harris, M. T., Improved metal cluster deposition on a genetically engineered tobacco mosaic virus template. *Nanotechnology* **2005,** 16, (7), S435-S441.
218. Chatterji, A.; Ochoa, W. F.; Ueno, T.; Lin, T. W.; Johnson, J. E., A virus-based nanoblock with tunable electrostatic properties. *Nano Letters* **2005,** 5, (4), 597-602.
219. Sano, K. I.; Sasaki, H.; Shiba, K., Specificity and biomineralization activities of Ti-binding peptide-1 (TBP-1). *Langmuir* **2005,** 21, (7), 3090-3095.
220. Lee, S. W.; Mao, C. B.; Flynn, C. E.; Belcher, A. M., Ordering of quantum dots using genetically engineered viruses. *Science* **2002,** 296, (5569), 892-895.
221. Deng, Z. X.; Mao, C. D., DNA-templated fabrication of 1D parallel and 2D crossed metallic nanowire arrays. *Nano Letters* **2003,** 3, (11), 1545-1548.
222. Park, S. H.; Barish, R.; Li, H. Y.; Reif, J. H.; Finkelstein, G.; Yan, H.; LaBean, T. H., Three-helix bundle DNA tiles self-assemble into 2D lattice or 1D templates for silver nanowires. *Nano Letters* **2005,** 5, (4), 693-696.
223. Banerjee, I. A.; Yu, L. T.; Matsui, H., Room-temperature wurtzite ZnS nanocrystal growth on Zn finger-like peptide nanotubes by controlling their unfolding peptide structures. *Journal of the American Chemical Society* **2005,** 127, (46), 16002-16003.
224. Coffman, E. A.; Melechko, A. V.; Allison, D. P.; Simpson, M. L.; Doktycz, M. J., Surface patterning of silica nanostructures using bio-inspired templates and directed synthesis. *Langmuir* **2004,** 20, (20), 8431-8436.
225. Frey, B. L.; Corn, R. M., Covalent attachment and derivatization of poly(L-lysine) monolayers on gold surfaces as characterized by polarization-modulation FT-IR spectroscopy. *Analytical Chemistry* **1996,** 68, (18), 3187-3193.
226. Lieber, C. M., Nanoscale science and technology: building a big future from small things. *MRS Bulletin* **2003,** 28, (7), 486-491.
227. Chen, R. J.; Bangsaruntip, S.; Drouvalakis, K. A.; Wong Shi Kam, N.; Shim, M.; Li, Y.; Kim, W.; Utz, P. J.; Dai, H., Noncovalent functionalization of carbon nanotubes for highly specific electronic biosensors. *Proceedings of the National Academy of Sciences* **2003,** 100, (9), 4984-4989.
228. Lee, S. Y.; Gao, X.; Matsui, H., Biomimetic and Aggregation-Driven Crystallization Route for Room-Temperature Material Synthesis: Growth of β-Ga2O3 Nanoparticles on Peptide Assemblies as Nanoreactors. *Journal of the American Chemical Society* **2007,** 129, (10), 2954-2958.
229. Banerjee, I. A.; Yu, L.; Matsui, H., Location-Specific Biological Functionalization on Nanotubes: Attachment of Proteins at the Ends of Nanotubes Using Au Nanocrystal Masks. *Nano Letters* **2003,** 3, (3), 283-287.
230. Piner, R. D.; Zhu, J.; Xu, F.; Hong, S.; Mirkin, C. A., "Dip-Pen" Nanolithography. *Science* **1999,** 283, (5402), 661-663.
231. Lee, K.-B.; Park, S.-J.; Mirkin, C. A.; Smith, J. C.; Mrksich, M., Protein Nanoarrays Generated By Dip-Pen Nanolithography. *Science* **2002,** 295, (5560), 1702-1705.
232. MacCuspie, R. I.; Nuraje, N.; Lee, S.-Y.; Runge, A.; Matsui, H., Comparison of Electrical Properties of Viruses Studied by AC Capacitance Scanning Probe Microscopy. *Journal of American chemical Society* **2008,** ASAP.

233. Giaever, I.; Keese, C. R., A morphological biosensor for mammalian cells. *Nature* **1993,** 366, (6455), 591-592.
234. Asami, K.; Gheorghiu, E.; Yonezawa, T., Real-Time Monitoring of Yeast Cell Division by Dielectric Spectroscopy. *Biophys. J.* **1999,** 76, (6), 3345-3348.
235. Horrocks, B. R.; Mirkin, M. V.; Pierce, D. T.; Bard, A. J.; Nagy, G.; Toth, K., Scanning electrochemical microscopy. 19. Ion-selective potentiometric microscopy. *Analytical Chemistry* **1993,** 65, (9), 1213-1224.
236. Xiao, C.; Lachance, B.; Sunahara, G.; Luong, J. H. T., An In-Depth Analysis of Electric Cell-Substrate Impedance Sensing To Study the Attachment and Spreading of Mammalian Cells. *Analytical Chemistry* **2002,** 74, (6), 1333-1339.
237. Tlili, C.; Reybier, K.; Geloen, A.; Ponsonnet, L.; Martelet, C.; Ouada, H. B.; Lagarde, M.; Jaffrezic-Renault, N., Fibroblast Cells: A Sensing Bioelement for Glucose Detection by Impedance Spectroscopy. *Analytical Chemistry* **2003,** 75, (14), 3340-3344.
238. Cherniavskaya, O.; Chen, L.; Weng, V.; Yuditsky, L.; Brus, L. E., Quantitative Noncontact Electrostatic Force Imaging of Nanocrystal Polarizability. *Journal of Physical Chemistry B* **2003,** 107, (7), 1525-1531.
239. Hilton, A. M.; Lynch, B. P.; Simpson, G. J., Reduction of Tip-Sample Contact Using Dielectrophoretic Force Scanning Probe Microscopy. *Analytical Chemistry* **2005,** 77, (24), 8008-8012.
240. Wilburn, J. P. W., D. W.; Cliffel, D. E., Imaging of voltage-gated alamethicin pores in a reconstituted bilayer lipid membrane via scanning electrochemical microscopy. *The Analyst* **2006,** 131, 311.
241. Sohn, L. L.; Saleh, O. A.; Facer, G. R.; Beavis, A. J.; Allan, R. S.; Notterman, D. A., Capacitance cytometry: Measuring biological cells one by one. *Proceedings of the National Academy of Sciences* **2000,** 97, (20), 10687-10690.
242. Beck, J. D.; Shang, L.; Marcus, M. S.; Hamers, R. J., Manipulation and Real-Time Electrical Detection of Individual Bacterial Cells at Electrode Junctions: A Model for Assembly of Nanoscale Biosystems. *Nano Letters* **2005,** 5, (4), 777-781.
243. Bhatt, K. H.; Grego, S.; Velev, O. D., An AC Electrokinetic Technique for Collection and Concentration of Particles and Cells on Patterned Electrodes. *Langmuir* **2005,** 21, (14), 6603-6612.
244. Layson, A.; Gadad, S.; Teeters, D., Resistance measurements at the nanoscale: scanning probe ac impedance spectroscopy. *Electrochimica Acta* **2003,** 48, (14-16), 2207-2213.
245. Shao, R.; Kalinin, S. V.; Bonnell, D. A., Local impedance imaging and spectroscopy of polycrystalline ZnO using contact atomic force microscopy. *Applied Physics Letters* **2003,** 82, (12), 1869-1871.
246. Pingree, L. S. C. M., E.F. Shull, K.R. Hersam, M.C., Nanoscale impedance microscopy-a characterization tool for nanoelectronic devices and circuits. *Nanotechnology, IEEE Transactions on* **2005,** 4, (2), 255.
247. Fasching, R. J.; Bai, S.-J.; Fabian, T.; Prinz, F. B., Nanoscale electrochemical probes for single cell analysis. *Microelectronic Engineering* **2006,** 83, (4-9), 1638.
248. Maliakal, A.; Katz, H.; Cotts, P. M.; Subramoney, S.; Mirau, P., Inorganic Oxide Core, Polymer Shell Nanocomposite as a High K Gate Dielectric for Flexible

Electronics Applications. *Journal of the American Chemical Society* **2005,** 127, (42), 14655-14662.
249. Polevaya, Y.; Ermolina, I.; Schlesinger, M.; Ginzburg, B.-Z.; Feldman, Y., Time domain dielectric spectroscopy study of human cells: II. Normal and malignant white blood cells. *Biochimica et Biophysica Acta (BBA) - Biomembranes* **1999,** 1419, (2), 257.
250. Cheung, K.; Gawad, S.; Renaud, P., Impedance spectroscopy flow cytometry: On-chip label-free cell differentiation. *Cytometry Part A* **2005,** 65A, (2), 124-132.
251. Jena, S. S.; Bloomfield, V. A., Probe Diffusion in Concentrated Polyelectrolyte Solutions: Effect of Background Interactions on Competition between Electrostatic and Viscous Forces. *Macromolecules* **2005,** 38, (25), 10551-10556.